11-20-2013

Assessing Functional Deficits at Optic Neuritis Onset in EAE Mice Using Manganese-Enhanced MRI (MEMRI) and Diffusion fMRI

Tsen-Hsuan Lin
Washington University in St. Louis

WASHINGTON UNIVERSITY IN ST. LOUIS

Department of Physics

Dissertation Examination Committee:
Mark S. Conradi, Chair
Sheng-Kwei Song, Co-Chair
James S. Schilling
William M. Spees
Ralf Wessel
Jason C. Woods

Assessing Functional Deficits at Optic Neuritis Onset in EAE Mice Using Manganese-Enhanced MRI (MEMRI) and Diffusion fMRI

by

Tsen-Hsuan Lin

A dissertation presented to the
Graduate School of Arts and Sciences
of Washington University in
partial fulfillment of the
requirements for the degree
of Doctor of Philosophy

December 2013
St. Louis, Missouri

Table of Contents

List of Figures

List of Tables

Acknowledgements

This dissertation is the summary of my graduate work, which was completed with the support of many people. First, I would like to offer my greatest appreciation to my research advisor, Dr. Sheng-Kwei (Victor) Song, for his guidance, encouragement, commitment, and support. He led me to enter the interesting MR-related research and provided guidance on many aspects of the work presented here, including imaging, biology, logic, presentation, and research attitude. I appreciate his trust when I spent longer time than others to master new techniques. He always offered his flexibility to allow me explore many possibilities in research and was happy to discuss any kind of question I had.

I also would like to express my great gratitude to my academic advisor, Dr. Mark Conradi, for his kind support and guidance during my early work on an automatic shimming project. I learned a lot of basic MR concepts, including MR signal processing and MR hadware in working with him. I appreciate his patience to answer basic questions and insight into how to think critically and solve the problems.

I am grateful for the help from Dr. William M. Spees. He was always willing to share his ideas and knowledge with me and mentor me in different aspects, including presentation, language, and a lot of interesting thoughts. Especially, I enjoyed working with him to learn and explore diffusion fMRI and appreciated his trust and flexibility to explore my own ideas.

In addition, I also express my appreciation for my collaborators. Dr. Anne H. Cross provided support, clinical insight, valuable comments, and suggestions. Mr. Bob Mikesell handled mouse EAE immunization and Dr. Kathryn Trinkaus provided valuable professional advice on statisticas.

I would like to thank Dr. Joong Hee Kim for his help and valuable discussions on basic aspects of MR and advanced applications. He is always happy to share his personal experience about animal studies and handling skills. I also would like to offer my deep appreciation to Dr. Chia-Wen Chiang for her encouragement, support, and sharing her knowledge with me. I also appreciate Dr. Tsang-Wei (William) Tu's help and support when I had just joined Song's group. I really enjoyed working with him and got a lot of valuable experience from our collaborations.

Special thanks to Dr. Carlos Perez-Torres. He shared a lot of his biological thoughts and knowledge with me and gave me his suggestions and comments on my writing. I also thank the members in Song's group: Drs. Peng Sun, Xiaojie Wang, and Yong Wang for their help.

I also would like to thank Dr. Jason C. Woods for serving on my thesis committee. I appreciate his suggestions and comments after every committee meeting. He always provided kind guidance and advised concerning how to think about problems. Special thanks to Drs. James S. Schilling and Ralf Wessel for serving on my defense committee.

I would like to offer my gratitude to several members of the BMRL: Dr. Joseph Ackerman, Dr. Joel Garbow, John Engelbach, Robert Massa, and Omar El-Ghazzawy for their help, discussion, and friendship.

In the end, and most importantly, I would like to offer my deepest appreciation and gratitude to my family in Taiwan. Without their patience, encouragement, and support, I could not have finished this degree. They always stand by me and let me pursue my goals. To them, I dedicate this thesis.

ABSTRACT OF THE DISSERTATION

Assessing Functional Deficits at Optic Neuritis Onset in EAE Mice Using Manganese-Enhanced MRI (MEMRI) and Diffusion fMRI

by

Tsen-Hsuan Lin

Doctor of Philosophy in Physics

Washington University in St. Louis, 2013

Professor Mark S. Conradi, Chair

Professor Shen-Kwei Song, Co-Chair

Optic neuritis (ON) is frequently a first sign of multiple sclerosis (MS), which is an inflammatory demyelinative disease of the central nerve system (CNS), including brain, optic nerve, and spinal cord. Investigating ON provides an approach to improve MS diagnosis and treatment monitoring. Experimental autoimmune encephalomyelitis (EAE) is a widely used animal model of MS and exhibits pathologies similar to the human disease. Magnetic resonance imaging (MRI) is a non-invasive tool to detect disease progress and as a standard diagnose procedure for MS in the clinic. In biological samples, the hydrogen nuclei are used to produce the MR signal due to its abundance in water and fat. As a result of tissue microstructural differences, ^{1}H nuclei exhibit tissue-specific and pathology-specific relaxation and diffusion properties, which are reflected in the resulting MR image contrast. Therefore, the pathologies of MS, such as inflammation, demyelination, and axonal injury can be detected using different MR-related tools, including T1- and T2-weighted imaging, diffusion-weighted imaging, and diffusion tensor imaging, and so on. Importantly, direct non-invasive assessment of functional deficits could be important for understanding pathology mechanisms or provide a useful bio-index to

validate treatment strategies. In this dissertation, manganese-enhanced MRI (MEMRI) and diffusion fMRI were introduced to explore the functional deficits, including axonal transport disruption and axon-activity dysfunction, at optic neuritis onset in EAE mice.

.

Chapter 1

Introduction

1.1 Multiple Sclerosis

Multiple sclerosis (MS) is an inflammatory demyelinating disease that mainly affects the central nervous system (CNS) such as brain, optic nerve and spinal cord (Fig. 1 – 1), usually diagnosed in young adults [1, 2]. Main symptoms include impaired vision, extreme fatigue, spasms, and paralysis of a variety of muscle systems [3]. Hallmarks of MS include focal inflammatory infiltration, demyelination, oligodendrocyte depletion, and axonal degeneration [4]. Around 85% of all MS cases initially develop relapsing-remitting MS (RR-MS, Fig. 1 – 2A), characterized by episodes of neurological disability and return to baseline. Approximately 50% of RR-MS patients, so-called secondary progressive MS (SP-MS, Fig. 1 – 2B), show relapses but clinical disability worsens over time. While people with SP-MS experience fewer relapses, the disability worsens and symptoms might become more severe. There is another 10% of all MS cases called primary progressive MS (PP-MS, Fig. 1 – 2C), chracterized by steadily worsening clinical disability. The final 5% of all MS cases, called progressive relapsing MS (PR-MS, Fig. 1 – 2D), is characterized by steady worsening of disability along with occasional relapses [5, 6].

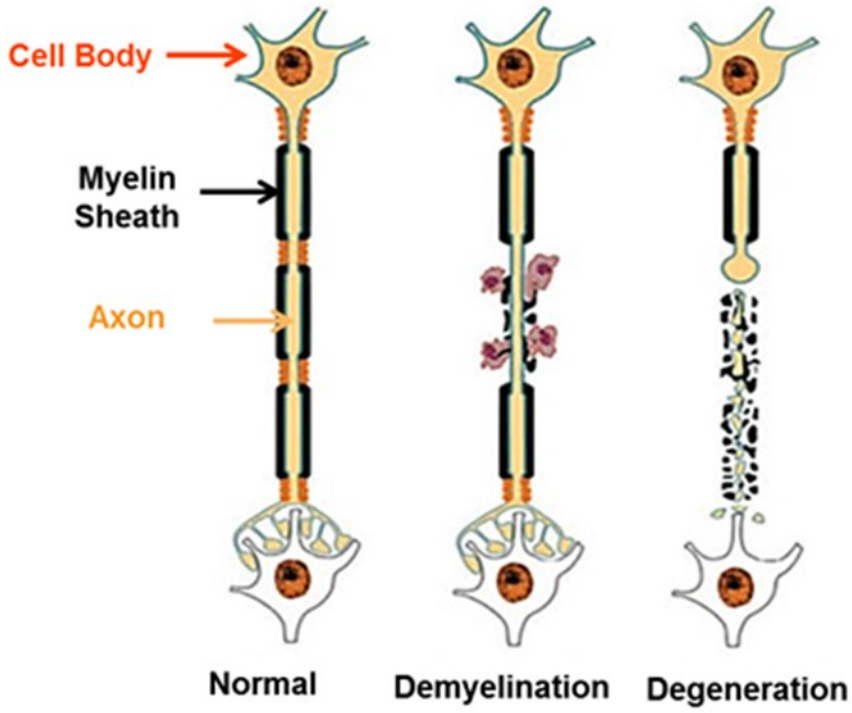

Figure 1 – 1 Disease process of MS is believed to start when lymphocytes cross the blood-brain barrier (BBB) and attack the myelin sheaths in CNS. Ultimately, it leads to axonal injury/degeneration.

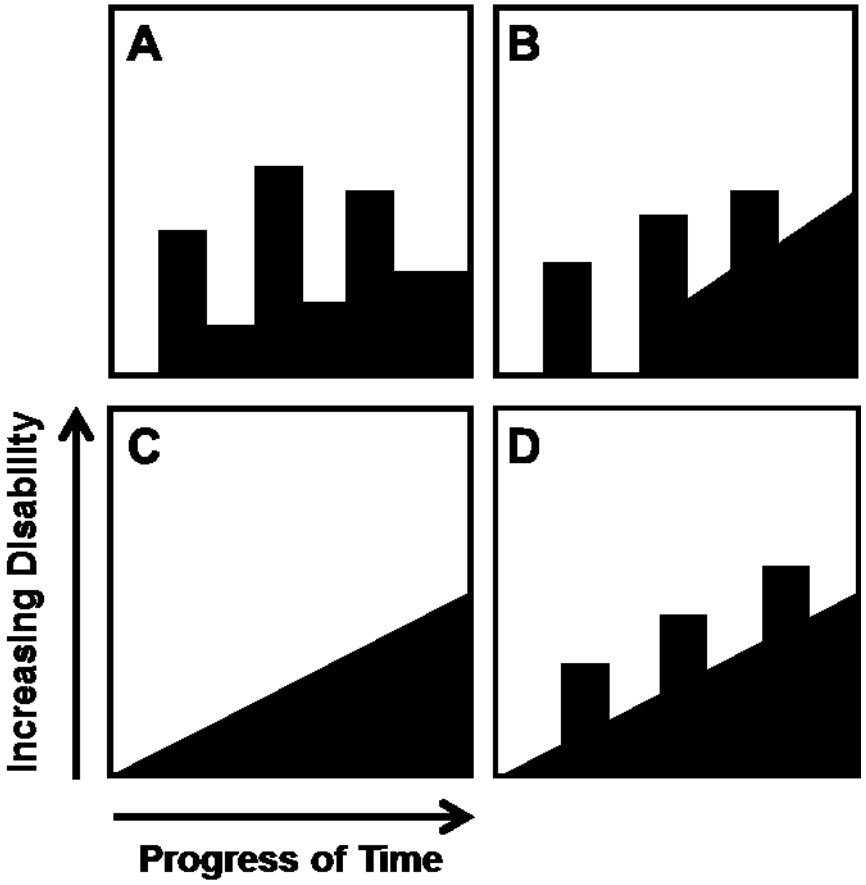

Figure 1 – 2 Types of MS (left to right; top to bottom): relapsing-remitting (A), secondary progressive (B), primary progressive and (C) progressive relapsing (D)

1.2 Disease Process of Multiple Sclerosis

It is believed that most MS starts with increased migration of lymphocytes across the blood-brain barrier (BBB) [4]. The lymphocyte-derived inflammation causes oligodendrocyte-associated demyelination which then blocks or slows propagation of electrical signals by white-matter axons (Fig. 1 – 3). In demyelinated axons, increased sodium channels redistribute homogeneously along axons to maintain conduction propagation, therefore, energy demand should be higher than usual to support extra regulation (Fig. 1 – 4). Importantly, mitochondria provide energy in form of ATP in CNS to maintain regular function, including conduction propagation and transport of proteins and organelles [7, 8]. However, due to acute inflammation, activated microglia and macrophages produce nitric oxide (NO), which can act to inhibit mitochondrial energy production, leading to diminished ATP. Therefore, this leads to dysfunction of energy-consuming Na^+/K^+ ATPase pump and Na^+/Ca^{2+} exchanger and eventually Ca^{2+} overload, which is directly associated with mitochondrial dysfunction. One consequence of this compromised cellular energetic status is a dysfunction of electrical signal propagation and axonal transport. Another serious consequence is a disruption of axonal protein and organelle transport along the length of the axons, required to maintain regular function, which further contributes to mitochondrial failure, leading to axonal injury and degeneration, [9, 10, 2, 11-15].

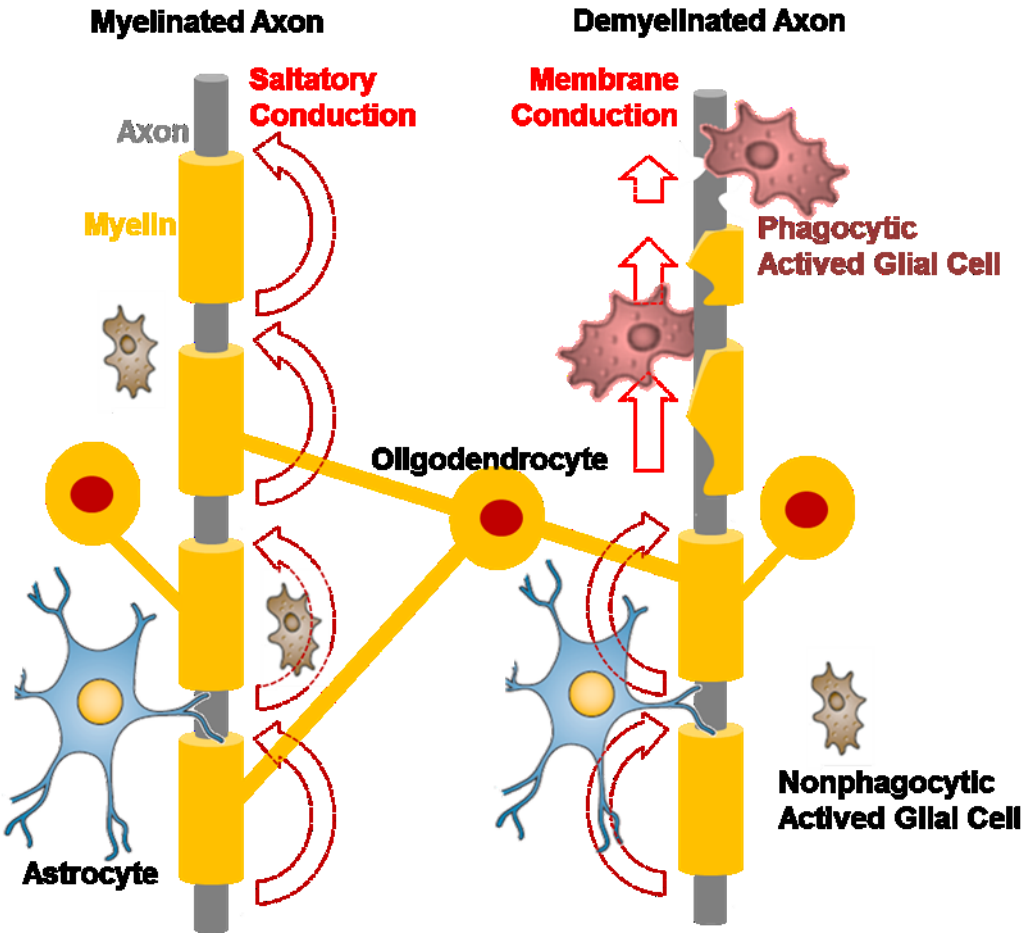

Figure 1 – 3 Electrical signal (action potential) propagation in myelinated and demyelinated axons. In MS, activated microglial cells attack myelin sheaths in CNS and lead to demyelination. The left-hand side of the figure shows fast signal propagation in myelinated axon. The membrane electrical disturbances jump between consecutive nodes of Ranvier. The right-hand side shows that electrical signal propagation in demyelinated axon is slowed due to non-saltatory membrane conduction (flat arrows).

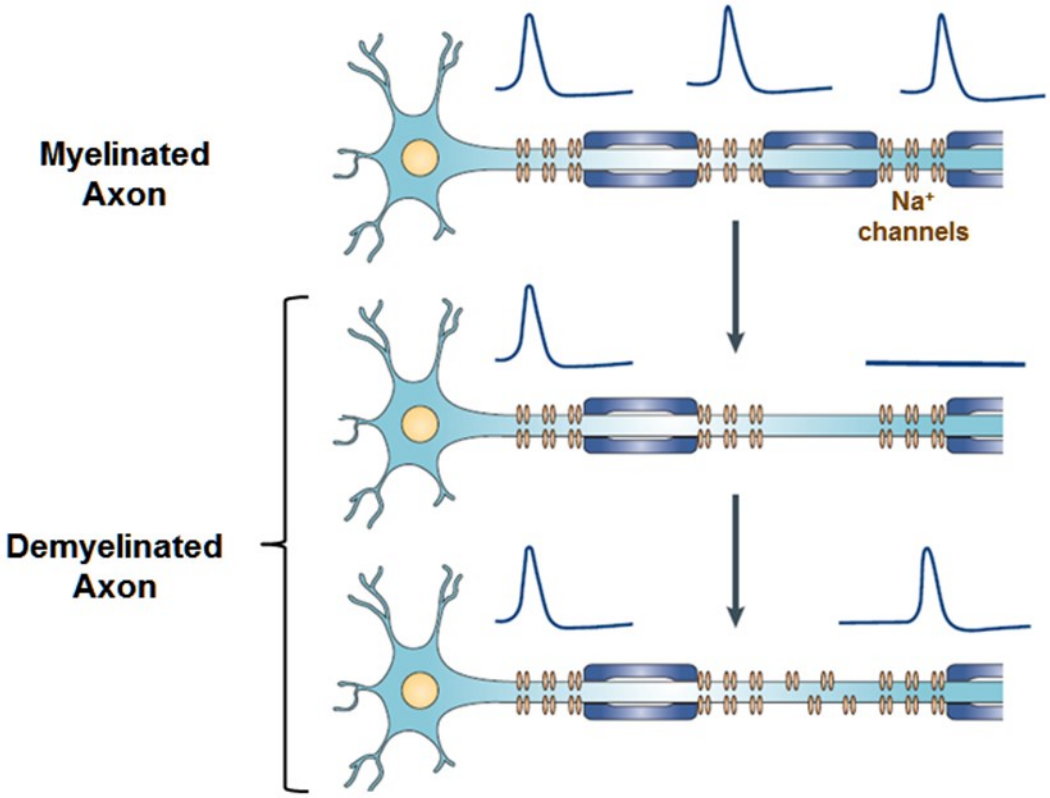

Figure 1 – 4 Sodium channels are increased and redistributed along demyelinated axons to main electrical signal (action potential) propagation.

1.3 Optic Neuritis of Multiple Sclerosis

Optic neuritis is an inflammatory disorder of the optic nerve and is the first sign of MS in 66% of cases (Fig. 1 – 5). Typically, MS patients with optic neuritis have sudden mono-ocular visual loss and/or pain [16, 17]. The ten- and fifteen-year risk of developing clinical MS following a single episode of optic neuritis is 38% and 50%, respectively [16, 18]. Hence, investigating the etiology and treatment of optic neuritis might be crucial to reduce later development of MS and long-term disability due to the significant relationship between MS and optic neuritis [19]. In general, patients are examined by vision tests (i.e. visual acuity, color vision, etc.) and diagnosis is confirmed with visual evoke potential (VEP), magnetic resonance imaging (MRI) and optical coherence tomography (OCT) [20]. VEP tests are recordings of the nervous system's electrical response to visual stimulation and might highlight demyelination which delays or blocks electrical potential propagation [21]. MRI could provide a non-invasive means to diagnose the lesion in CNS [18, 22]. OCT is a non-invasive measurement using infrared light to reflect retinal thickness, which is associated with axonal and neuronal degeneration [23, 24].

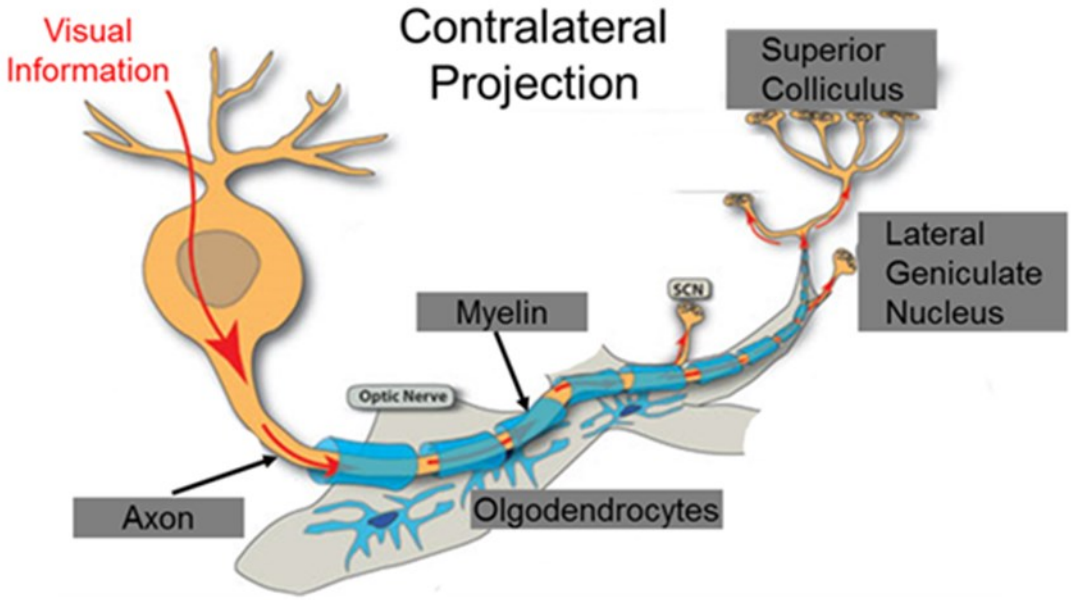

http://www.vanderbilthealth.com/eyeinstitute/23604

Figure 1 – 5 Visual signal is relayed from from retinal ganglion cell axons of the optic nerve via synaptic terminalsto the lateral geniculate nucleus (LGN) and superior colliculus (SC). Demyelination cancause signal propagation blockage and lead to axonal injury.

1.4 Animal Model of Multiple Sclerosis

Experimental autoimmune encephalomyelitis (EAE) is a widely used animal model of MS and can be induced in several species, including mice, rats, non-human primates, and so on. EAE is induced by immunization with myelin antigens (active induction) such as myelin oligodendrocyte glycoprotein (MOG), myelin basic protein (MBP), and myelin proteolipid protein (PLP) or via adoptive transfer of myelin-reactive T cells (passive induction) [5, 25, 26]. Many of the immune mediators responsible for EAE pathologies have been shown to play a role in MS, but there are differences between EAE and MS: the auto-antigen against which the immune response is directed is known in EAE, while the etiology of MS is unknown. However, EAE models have greatly advanced our understanding of T-cell mediated neuroinflammation. For example, heterogeneity of disease is an important feature of both EAE and MS [25]. MOG-specific EAE in rodents has been shown to include the development of optic neuritis during its course [27-29] and provides an appropriate model to investigate optic neuritis of MS.

1.5 Mouse Visual System and Visual Acuity

The mouse visual system has become one of the primary models for the study of the human visual system. The mouse eye is remarkably similar in structure to the human eye and shares similar cell types and structural features. Therefore, studies in the mouse models might lead to a better understanding of the mechanism of human disease [30]. Indeed, the mouse visual system has been reported to show functional response similar to the human visual system [31]. The visual pathway starts from retinal ganglion cells (inner layer of retina), and connects to the optic nerve. After the optic chiasm, 95% of optic nerve axons project to the contralateral optic tract, lateral geniculate nuclei (LGN), and superior colliculus (SC) [32] (Fig. 1 – 6).

To determine if EAE mouse developed optic neuritis, rapid and reproducible behavioral assessment of visual-tracking was introduced using Virtual Optometry System (Optomotry, Cerebral Mechanics, Inc., Canada) to reflect visual system integrity [33, 34] (Fig. 1 – 7). Briefly, virtual rotating columns were projected on the LCD monitors with different spatial frequencies in cycles/degree (c/d). The mouse head movement in response to the virtual column rotations was noted. The spatial frequency was incremented from 0.1 c/d with step size of 0.05 c/d until the mouse stopped responding. The VA was defined as the highest spatial frequency of virtual rotating columns to which the mouse was able to respond. We have previously reported that normal VA of C57BL/6 was 0.38 ± 0.03 c/d (mean ± S.D., n=30) and defined VA ≤ 0.25 c/d as the onset of acute ON for EAE mice [35]. In Chapter 3 and 4, after immunization, VA of each eye was evaluated daily. MRI was performed on mice with VA ≤ 0.25 c/d, the operational definition of ON.

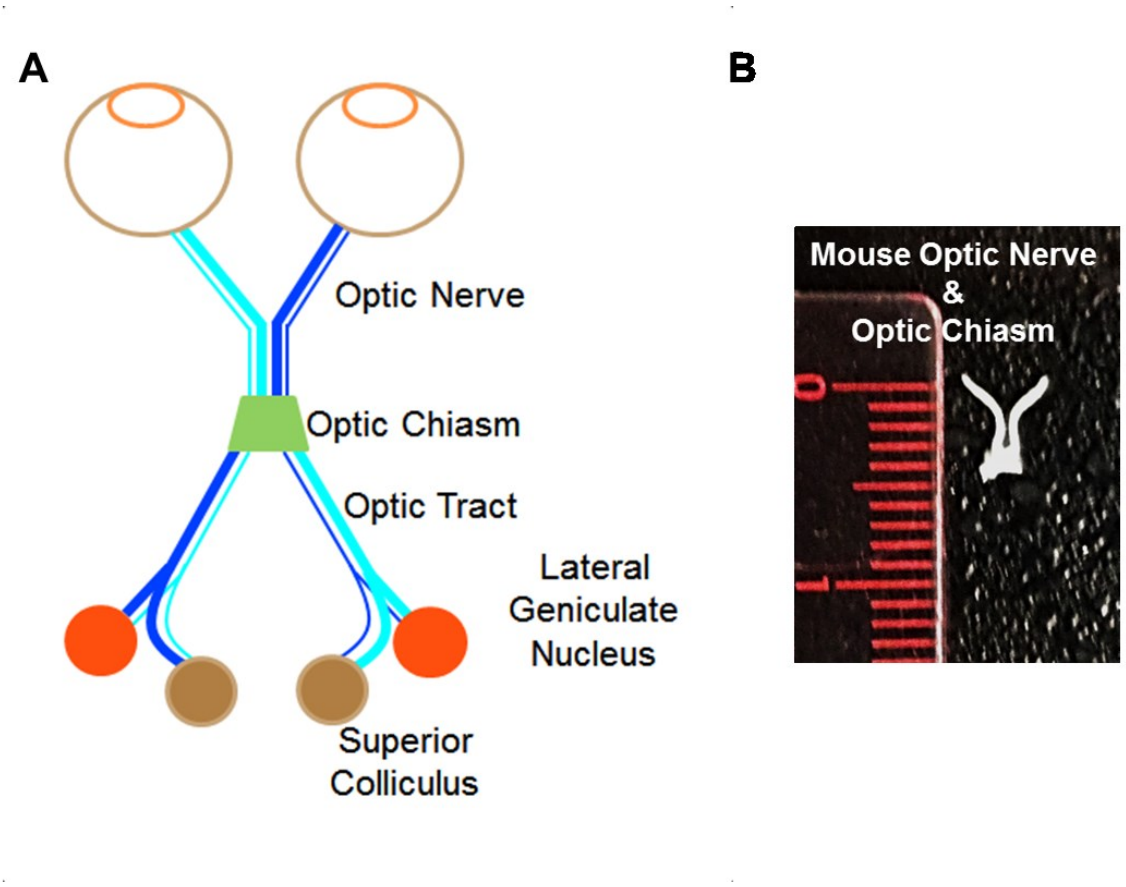

Figure 1 – 6 Visual system consists of retina, optic nerve, optic chiasm, optic tract, lateral geniculate nucleus (LGN), and superior colliculus (SC). Most (~95%) optic nerve after optic chiasm corresponds to contralateral LGN and SC (A). After intravitreal Mn^{2+} injection, it goes from ipsilateral retina and optic nerve to contralateral LGN and SC (seen details in Chapter 2 and 3). The real mouse optic nerve and optic chiasm are shown the same structure as A.

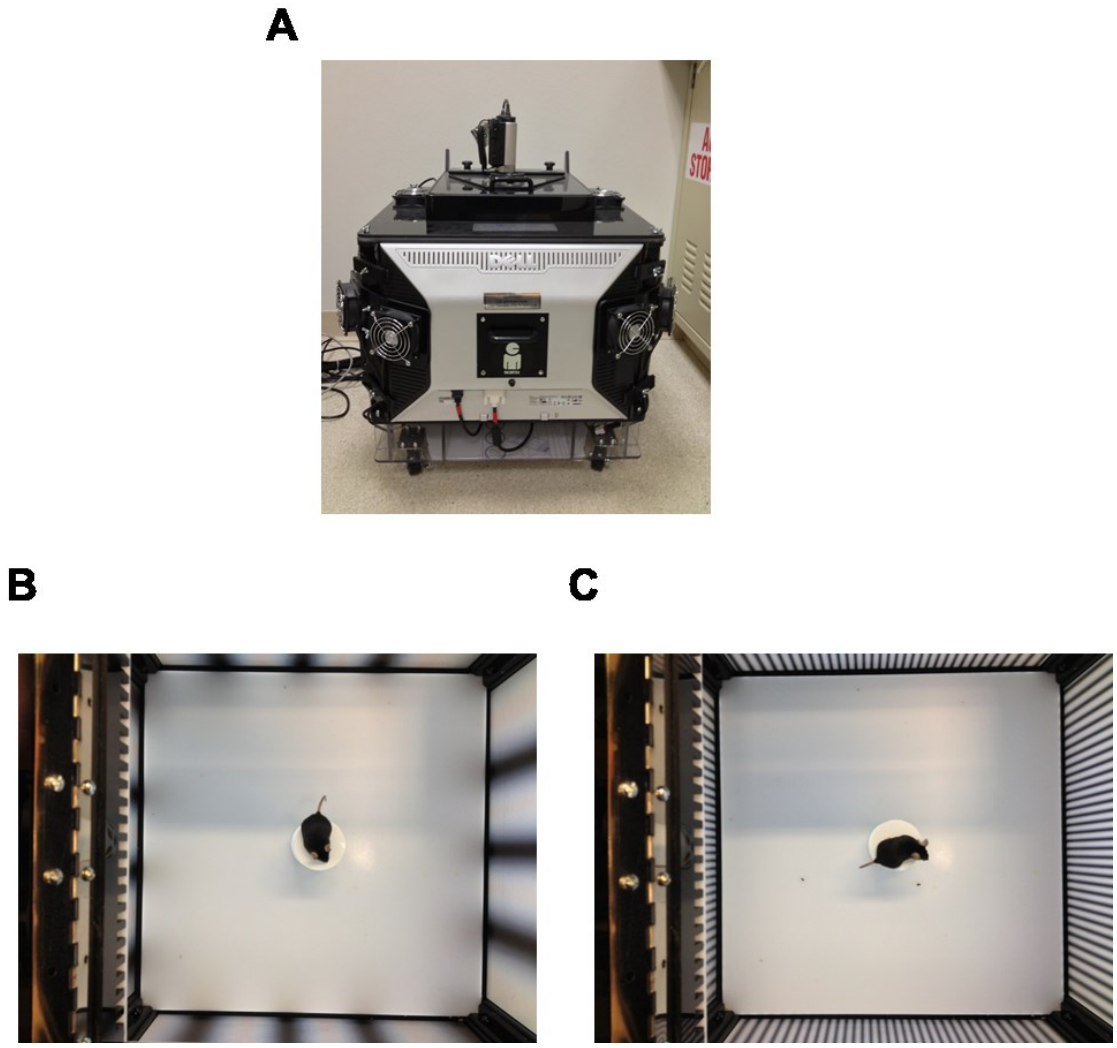

Figure 1 – 7 Optokinetic response (OKR) reflects mouse visual acuity. The testing apparatus was comprised by four LCD monitors (faced inward) with a camera at the top (A). Mouse was placed in the testing box surrounding with LCDs. Moving bar graphs were provided on the screens with different spatial frequencies (cycle/degree) (B and C); therefore, mouse can see thick (lower spatial frequency) or thin (higher spatial frequency) bar graphs. Direction of moving bar graphs can move either clockwise or counterclockwise to test specific left and right eye. Operator can track movement of mouse head to determine if mouse responded or not. (Seen Section 1.6 for details protocol of operation)

1.6 Magnetic Resonance Imaging as a Non-invasive Bio-marker

Magnetic resonance imaging (MRI) has been a non-invasive approach to the diagnosis of MS since the first MR images were acquired in MS patients in the early 1980s [36]. MRI now serves as one of the standard diagnostic approaches for MS. Therefore, it is a promising tool in assessment of optic neuritis in MS and EAE [1, 37-42]. The inflammation induced morphological changes in CNS, including BBB break-down, inflammation, demyelination, axonal injury or degeneration, are validated by gadolinium contrast enhancement image, manganese-enhanced MRI (MEMRI), T1- and T2-weighted image, diffusion-weighted imaging (DWI), and diffusion-tensor imaging (DTI). According to these approaches, morphological features of optic neuritis in MS and EAE are further understood. However, these metrics cannot directly assess the functional deficits in optic nerve/white matter in MS and EAE. Since functional deficits might precede morphological changes, investigating functional deficits should shed light on treatment strategies for optic neuritis that could further prevention of MS. MRI might provide an *in vivo* non-invasive means to 'monitor' real-time functional processes. We believe that regular axonal activity, including axonal transport (Fig. 1 – 8) and electrical signal propagation (Fig. 1 – 3), can be detected by MRI. The following sections will introduce some important principles of NMR/MRI and show how we take advantage of these properties to reflect biological function.

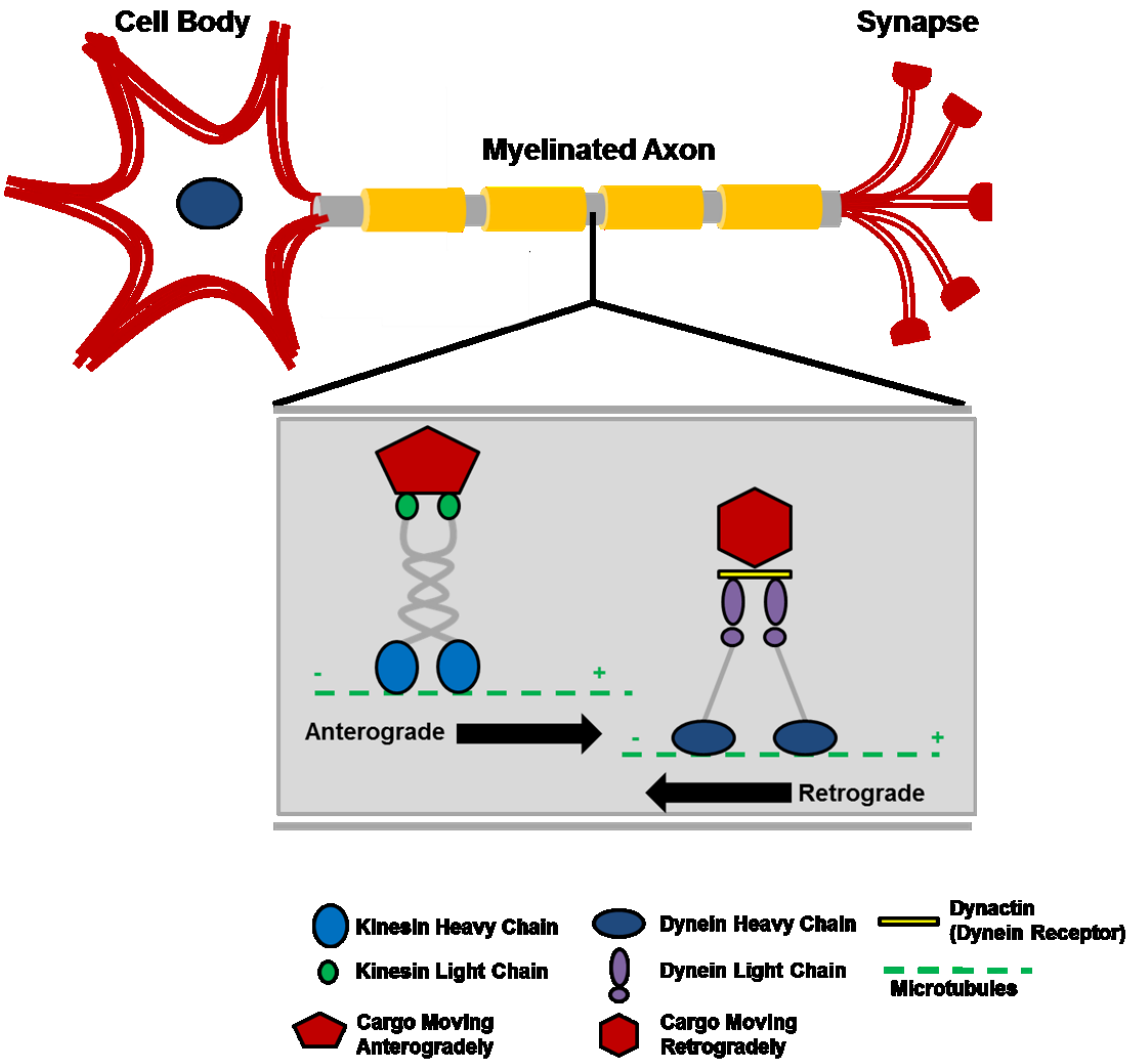

Figure 1 – 8 Axonal transport is crucial to maintain regular function. Motor proteins can move along microtubules, the cytoskeleton of axon, within axons to deliver proteins and organelles in either anterograde or retrograde direction.

1.7 Nuclear Magnetic Resonance and Magnetic Resonance Imaging

MRI is an advanced application of nuclear magnetic resonance (NMR). NMR began in 1946 with two independent but simultaneous groups led by Purcell [43] and Bloch [44], respectively. The key property of NMR-active nuclei is that they possess spin or intrinsic spin angular momentum. However, not all nuclei exhibit spin. Specific isotopes fall into one of three groups of spin values, zero, integral, and half-integral. Only integral spin value with an even atomic weight and an odd atomic number (e.g. ^{2}H) and half-integral spin value with an odd atomic weight (e.g. ^{1}H, ^{23}Na, and ^{31}P, etc.) can be detected in NMR. The ^{1}H nucleus is the most commonly-used nuclei for use in MRI signals. It has a spin of ½ and is the most abundant isotope of hydrogen.

Water molecules, which constitute two third of human/animal body weight, consist of two hydrogens and one oxygen atom. Thus water protons account for the bulk of the ^{1}H MRI signal in biological samples. In the absence of a magnetic field, protons with ½ spin equally distribute between two energy states and thus cancel their collective magnetic effect. In the magnet with constant magnetic field $B_0\,\hat{z}$, at equilibrium, the fraction of spins that are oriented parallel to the direction of B_0 is slightly greater than those that are anti-parallel to B_0. The equilibrium population of spin states is by Boltzmann statistics (Eq. 1.1).

$$\frac{N_{m=-1/2}}{N_{m=+1/2}} = e^{-\Delta E/kT} \tag{1.1}$$

where N_m is the fraction of particle population in each state, k is Boltzmann constant, 1.381×10^{-23} JK^{-1}, and T is the absolute temperature in Kelvin. This unequal population of spin-states produces a non-zero net magnetization (vector sum of spin-up and spin-down within the ensemble).

The corresponding Hamiltonian of the interaction between the spins and B_0 field is shown in Eq. (1.2)

$$\boldsymbol{H}\Psi_m = -\gamma B_0 \boldsymbol{I_z}\Psi_m = -m\hbar\gamma B_0 \Psi_m \tag{1.2}$$

where $\boldsymbol{H}$ is the Hamiltonian operator, Ψ_m is an eigenfunction, $\boldsymbol{I_z}$ is an angular momentum operator, γ is gyromagnetic ratio, m is its spin quantum number, B_0 is the main magnetic field strength, h is Planck's constant, 6.626×10^{-34} **J**·s (ħ is h divided by 2π), and $-m\hbar\gamma B_0$ is the corresponding eigenvalue. The energy gap between two states is shown in Eq. (1.3) (Fig. 1 – 9)

$$\Delta E = E_{+1/2} - E_{-1/2} = \pm\hbar\gamma B_0 = \hbar\omega_0 \tag{1.3}$$

$$\omega_0 = \gamma B_0 \tag{1.4}$$

A time-varying (varying with frequency $\nu_0 = \omega_0/2\pi$), applied perpendicular to B_0 magnetic field, and typically denoted as B_1 can induce transitions between the two spin states. The resonance is known as resonance frequency or absorption frequency, which is associated with γ and B_0.

For each proton (microscopic view), the angular momentum is quantized. However, for a bulk sample of magnetic dipoles (macroscopic view), the interaction of the net magnetization with applied magnetic fields (B_0 and/or B_1) is conveniently treated using classical mechanics [46] (Fig. 1 – 10). This macroscopic view ignores quantum effects due to the small order of ħ [45]. In this classical treatment, the net magnetization precesses in the B_0 field with a frequency that is the same as the absorption frequency, called the Larmor frequency.

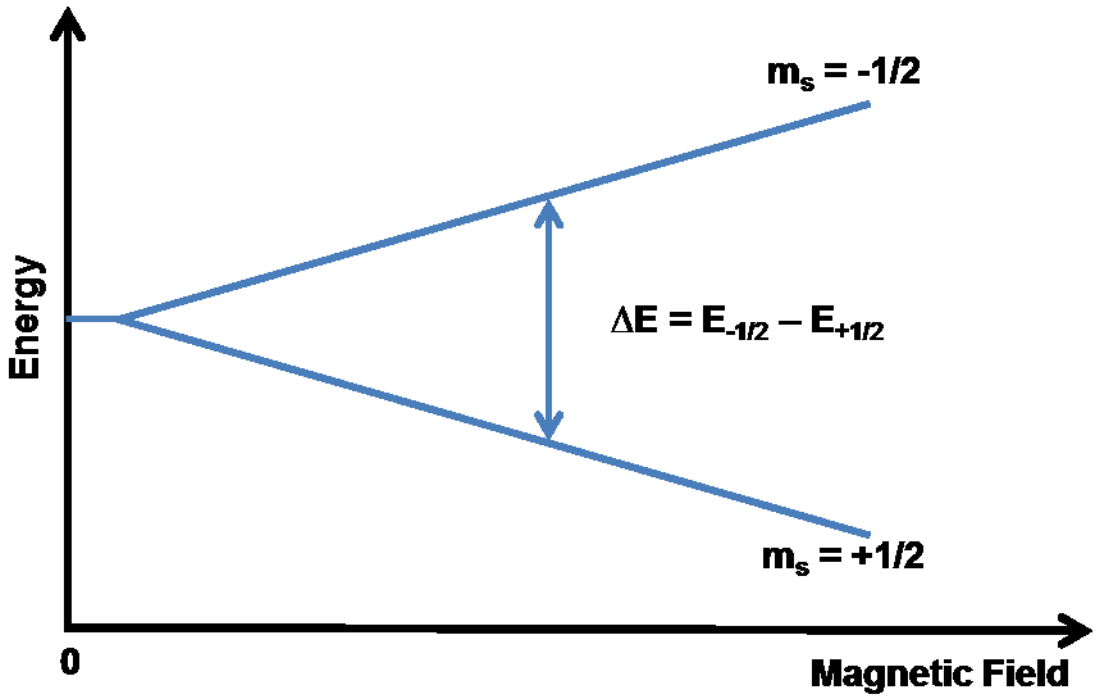

Figure 1 – 9 Nuclei that possess spin align themselves to the corresponding energy state in magnetic field, so-called Zeeman Effect. The spins are separated into two groups -1/2 (anti-parallel) and +1/2 (parallel) by magnetic field. Energy gap can correspond to specific resonance frequency, so-called Larmor frequency.

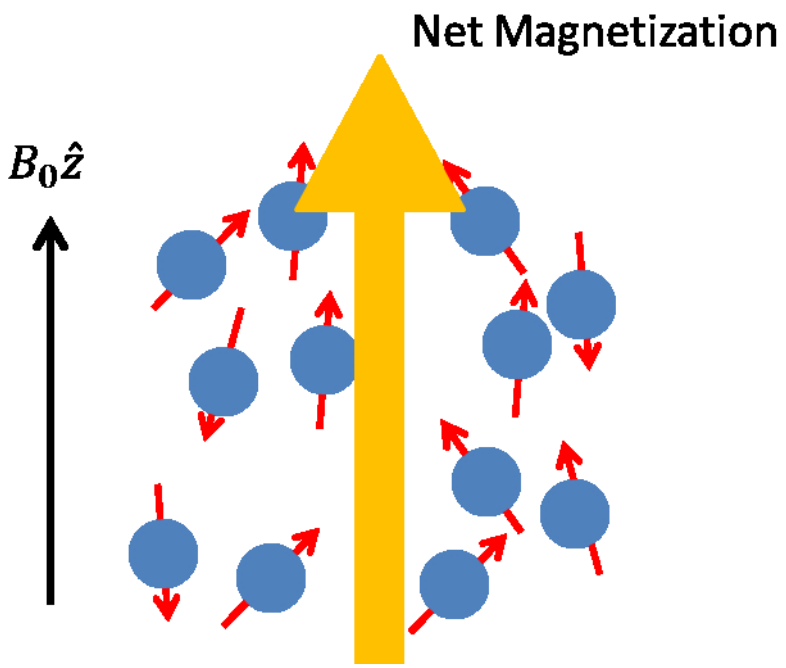

Figure 1 – 10 For macroscopic view, net magnetization is the vector to represent the combination effects of total spins

1.7.1 T1 and T2 Relaxation

Magnetization in magnetic field experiences a torque, which is the rate of change of angular momentum (analogous to Newton's first law that force is the rate of change of momentum). Their relationships could be presented as a motion equation like Eq. (1.5) and (1.6) (in rotating frame)

$$\mathbf{N} = \frac{d\boldsymbol{L}}{dt} = \boldsymbol{\mu} \times \boldsymbol{B} \tag{1.5}$$

$$\frac{d\boldsymbol{\mu}}{dt} = \gamma\,(\boldsymbol{\mu} \times \boldsymbol{B}) \tag{1.6}$$

where $\mathbf{L} = \mathbf{I}\omega_0$, $\boldsymbol{\mu} = \gamma\,\mathbf{L}$, **N** is a torque, **μ** is a dipole moment, **B** is a magnetic field, and γ is a gyromagnetic ratio.

In addition to precession in the magnetic field, magnetization also experiences relaxation. That is, once perturbed from equilibrium, the magnetization gradually tends to approach the most-probable (Boltzmann distribution) population of spin-states. Therefore, Bloch proposed a set of differential equations to represent precession and relaxation of magnetization in magnetic field [44]. If the magnetic field is constant (B_0) and in $\hat{z}$ direction the equations are as follow

$$\frac{dM_x}{dt} = \gamma B_0 M_y - \frac{M_x}{T_2} \tag{1.7}$$

$$\frac{dM_y}{dt} = -\gamma B_0 M_x - \frac{M_y}{T_2} \tag{1.8}$$

$$\frac{dM_z}{dt} = -\frac{M_z - M_0}{T_1} \tag{1.9}$$

where M_x and M_y are transverse component of magnetization, M_0 is net equilibrium

magnetization, M_z is the longitudinal component of net magnetization, M_0 is the equilibrium magnetization, T_1 is a longitudinal relaxation time constant, and T_2 is time constant for decay of transverse magnetization components. The solutions of Eq. (1.9) is shown in Eq. (1.10)

$$M_z(t) = M_0 + [M_z(0) - M_0]\, e^{-\frac{t}{T_1}} \tag{1.10}$$

and if we let $M_{xy} = M_x + i\, M_y$, Eq. (1.7) and (1.8) are rewritten as Eq. (1.11)

$$\frac{dM_{xy}}{dt} = \left(\frac{dM_x}{dt} + i\frac{dM_y}{dt}\right) = \left[\left(\gamma M_y B_0\right) - \frac{M_x}{T_2}\right] + i\left[\left(\gamma M_x B_0\right) - \frac{M_y}{T_2}\right] \tag{1.11}$$

the solution of transverse magnetization is shown in Eq. (1.12)

$$\mathrm{M}(t) = M_0\, e^{-iB_0\gamma t}\, e^{-\frac{t}{T_2}} = M_0\, e^{-i\omega_0 t}\, e^{-\frac{t}{T_2}} \tag{1.12}$$

where $\omega_0 = B_0\, \gamma$, Larmor frequency

After a 90º RF pulse, the magnetization is flipped to the transverse plane, and decay of the net magnetization, viewed in an on-resonance rotating frame (i.e., a reference frame rotating about B_0 with angular frequency ω_0) can represented as Eq. (1.13)

$$M_\perp(t) = M_0 e^{-\frac{t}{T_2}} \tag{1.13}$$

Different tissues have their own specific field-strength-dependent T1 and T2 relaxation time constants. MRI takes advantage of this property and utilizes different MR parameters to bias measurements based upon T1 or T2 characteristics, so called T1- or T2- weighted images. Fig. 1 – 11 demonstrates the different T1 and T2 relaxation times of brain tissue.

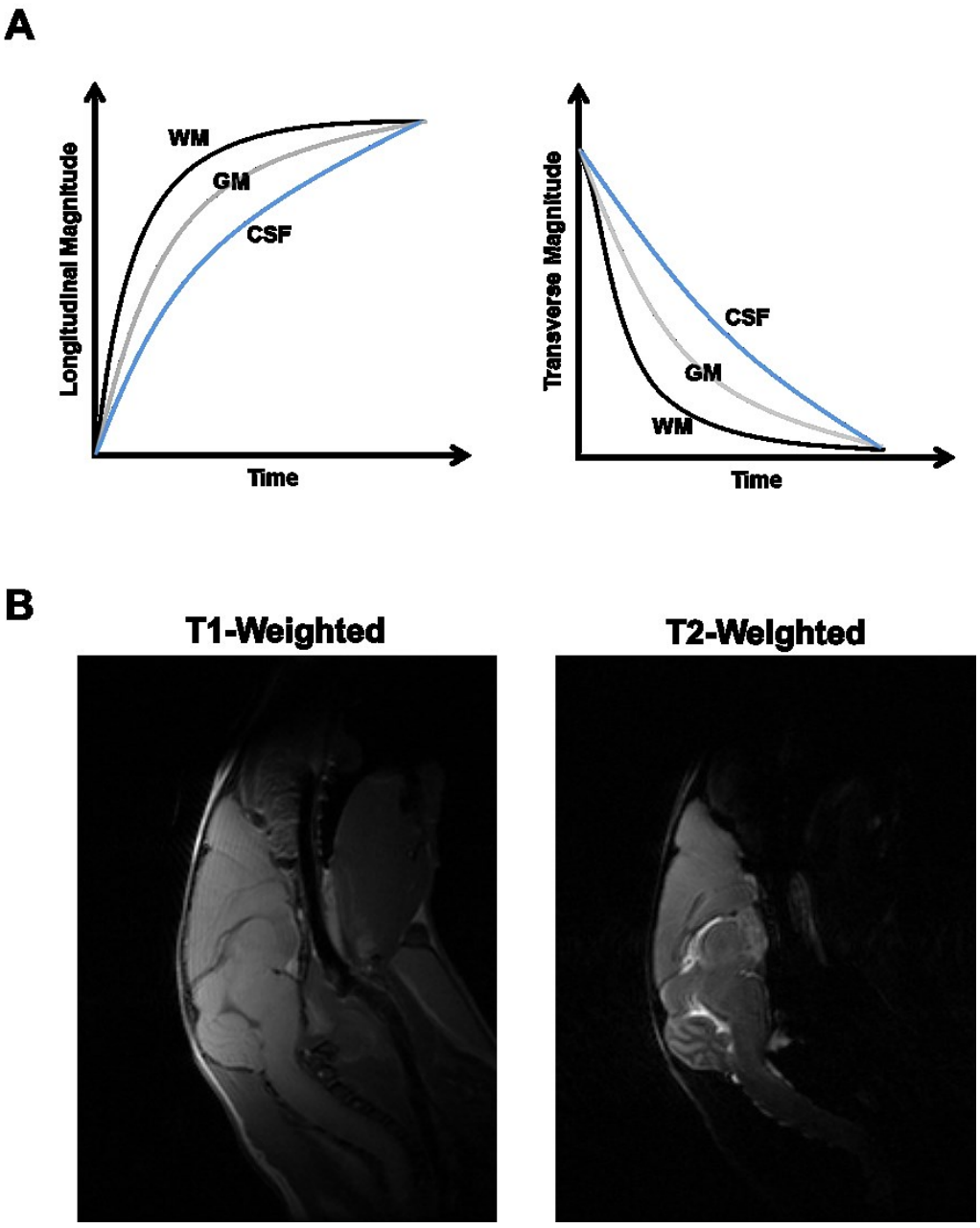

Figure 1 – 11 White matter (WM), gray matter (GM), and cerebrospinal fluid (CSF) have different T1 and T2 relaxation time. The specific MR parameters (i.e. TR or TE) can reveal tissue contrast (A). Representative T1- and T2-weighted middle sagittal images of mouse brain show different contrast. Image parameter: 30 mm × 30 mm × 1 mm; T1-weighted spin-echo sequence with TR = 600 ms, TE = 25 ms, Average = 8; T2-weighted spin-echo sequence with TR = 3,000 ms, TE = 100 ms, Average = 4.

1.7.2 Diffusion NMR and MRI

The relationship of Brownian motion (self diffusion) of molecules and diffusivity in microscopic view was described by Einstein in 1905 (Eq. (1.14)).

$$\langle (r_1 - r_0)^2 \rangle = 2 \cdot D \cdot t \tag{1.14}$$

where $\langle (x_1 - x_0)^2 \rangle$ is the mean square displacement, D is the diffusion coefficient, and t is the time interval. For the case of diffusion in 3-D, the mean square displacement is $6Dt$.

Regarding macroscopic view, Fick's 1st law describes that the movement of molecules are from region of high concentration to low concentration by random molecular motion (Eq. (1.15)).

$$\mathbf{J} = -\mathrm{D}\nabla\mathbf{C} \tag{1.15}$$

where $\mathbf{J}$ is diffusion flux, and $\mathbf{C}$ concentration gradient. Conservation of mass during the diffusion process implies $-\nabla\mathbf{J} = \frac{\partial \mathbf{C}}{\partial \mathbf{t}}$. It leads to Fick's 2nd law (Eq. (1.16))

$$\frac{d\boldsymbol{C}}{dt} = \boldsymbol{\nabla} \cdot \mathrm{D}\boldsymbol{\nabla}\, \mathrm{C} \tag{1.16}$$

Torrey proposed that this diffusional motion could be accounted for in the Bloch equations by adding an additional term [47]. Subsequently, the new simultaneous equations (Eq. (1.17) to Eq. (1.19)) become as below

$$\frac{dM_x}{dt} = \gamma B_0 M_y - \frac{M_x}{T_2} + \boldsymbol{\nabla} \cdot \mathrm{D}\boldsymbol{\nabla}\, M_{\boldsymbol{x}} \tag{1.17}$$

$$\frac{dM_y}{dt} = \gamma B_0 M_y - \frac{M_x}{T_2} + \boldsymbol{\nabla} \cdot \mathrm{D}\boldsymbol{\nabla}\, M_{\boldsymbol{y}} \tag{1.18}$$

$$\frac{dM_z}{dt} = -\frac{M_z - M_0}{T_1} + \nabla \cdot D\nabla (M_z - M_0) \quad (1.19)$$

where D is diffusion coefficient

If the diffusion is isotropic, then, the Bloch-Torrey equations can be re-written as Eq. (1.20), (1.21) and (1.22)

$$\frac{dM_x}{dt} = \gamma B_0 M_y - \frac{M_x}{T_2} + D\nabla^2 M_x \quad (1.20)$$

$$\frac{dM_y}{dt} = \gamma B_0 M_y - \frac{M_x}{T_2} + D\nabla^2 M_y \quad (1.21)$$

$$\frac{dM_z}{dt} = -\frac{M_z - M_0}{T_1} + D\nabla^2 (M_z - M_0) \quad (1.22)$$

A decade later (1965), Stejskal and Tanner modified Hahn's spin echo experiment and designed the pulse gradient spin echo (PGSE) experiment with two identical magnetic gradients before and after 180º RF pulse to encode the diffusing spin [48, 49] (Fig. 1 – 12). Let us again define the complex transverse magnetization as $M_{xy} = Mx + iMy$. After adding diffusion terms and considering gradients ($B_z = B_0 + G \cdot z$, $B_x = ½ (G \cdot x)$ and $= ½ (G \cdot y)$), Eq. (1.11) is rewritten as Eq. (1.23)

$$\frac{dM_{xy}}{dt} = -i\omega_0 M_{xy} - i\gamma G \cdot z\, M_{xy} - \frac{M}{T_2} + D\nabla^2 M_{xy} - \frac{1}{2} i\gamma G(x + iy) M_z \quad (1.23)$$

where $\omega_0 = B_0 \gamma$ and M_{xy}, the complex transverse magnetization, which precesses about the z axis with angular speed – ω_0. Then, Eq. (1.24) is putting in Eq. (1.23) and obtaining Eq. (1.25)

$$m = \varphi\, e^{-i\omega_0 t}\, e^{-\frac{t}{T_2}} \quad (1.24)$$

$$\frac{d\varphi}{dt} = -i\gamma G \cdot z\ \varphi + \mathrm{D}\nabla^2\ \mathrm{M} - \frac{1}{2} i\gamma G(x+iy) M_z\ e^{\,i\omega_0 t}\ e^{\frac{t}{T_2}} \tag{1.25}$$

the third term of Eq. (1.25) is the order of $M_0 G(x+iy)/B_0$, which is assumed to be negligible. Therefore, Eq. (1.25) is rewritten as Eq. (1.26)

$$\frac{d\varphi}{dt} = -i\gamma G \cdot z\ \varphi + \mathrm{D}\nabla^2\varphi \tag{1.26}$$

Now, if a constant magnetic field gradient **G** is applied and is collinear with B_0. The magnetization precesses in the resulting magnetic field

$$B_z = B_0 + \mathbf{G} \cdot \mathbf{r} \tag{1.27}$$

the gradient **G** is assumed uniform through whole sample and **r** is the position vector for a given nucleus. The Eq. (1.26) is rewritten as Eq. (1.28)

$$\frac{d\varphi}{dt} = -i\gamma \boldsymbol{G} \cdot \boldsymbol{r}\ \varphi + \mathrm{D}\nabla^2\varphi \tag{1.28}$$

In the absence of diffusion, φ in Eq. (1.28) can be written as Eq. (1.29), which represents the transverse magnetization at any time point. φ(0) = A represents the transverse magnetization immediately after the first 90º RF pulse

$$\varphi = Ae^{-i\gamma \boldsymbol{r} \cdot F(t)} \tag{1.29}$$

where

$$\mathbf{F}(\mathrm{t}) = \int_0^t G(t')dt'$$

After time τ, at which a 180° refocusing pulse is applied, Eq. (1.29) can be rewritten as Eq. (1.30)

$$\varphi = Ae^{-i\gamma \boldsymbol{r} \cdot [F(t) - 2\boldsymbol{f}]} \tag{1.30}$$

where $\mathbf{f} \equiv \mathbf{F}(\tau)$, and it corresponds to the phase angle that has accumulated between 90º and 180º

RF pulse, due to the time-varying applied diffusion gradients. If we want to correctly describe the magnetization before the 180º RF pulse, the new parameter, $\xi = 1$ for $t < \tau$ and $\xi = -1$ for $t > \tau$, is introduced. Then, the Eq. (1.30) is modified as Eq. (1.31)

$$\varphi = Ae^{-i\gamma \boldsymbol{r}\cdot[F(t)+(\xi-1)\boldsymbol{f}]} \tag{1.31}$$

therefore, after 180º RF pulse, the second exponent is -2**f**, while the first exponent continues to increase from **F** (τ) to **F** (2τ). A spin echo is formed when **F** (2τ) = 2**f**. Then, the second exponential term is equal to one. Stejskal-Tanner assumed that the solution of equation 1.28 with diffusion effects would take the same shape as in the non-diffusing case. They also let A be a function of time, A(t), in the presence of diffusion.

Now, the Eq. (1.28) without diffusion is rewritten as Eq. (1.32)

$$\frac{d\varphi}{dt} = \frac{dA(t)}{dt} e^{-i\gamma \boldsymbol{r}\cdot[F(t)+(\xi-1)\boldsymbol{f}]}$$

$$+A(t)(-i\gamma \boldsymbol{r})[\frac{d\boldsymbol{F}(t)}{dt} + (\xi - 1)\frac{d\boldsymbol{f}}{dt}]e^{-i\gamma \boldsymbol{r}\cdot[F(t)+(\xi-1)\boldsymbol{f}]} \tag{1.32}$$

where

$$\frac{d\boldsymbol{F}(t)}{dt} = \mathbf{G}(\mathrm{t}) \tag{1.33}$$

and

$$\frac{d\boldsymbol{f}}{dt} = 0 \tag{1.34}$$

The Laplacian term of Eq. (1.28) would be like Eq. (1.35)

$$\mathrm{D}\boldsymbol{\nabla^2}\varphi = \mathrm{D}\boldsymbol{\nabla^2} A(t)e^{-i\gamma \boldsymbol{r}\cdot[F(t)+(\xi-1)\boldsymbol{f}]}$$

$$= -DA(t)\gamma^2[F(t) + (\xi - 1)\boldsymbol{f}]^2 e^{-i\gamma \boldsymbol{r}\cdot[F(t)+(\xi-1)\boldsymbol{f}]} \tag{1.35}$$

Substituting Eq. (1.35) into the Laplacian term of Eq. (1.28) and equating Eq. (1.32) gives

$$\frac{dA(t)}{dt} = -\mathrm{A(t)D}\gamma^2[\mathbf{F(t)} + (\xi - 1)\mathbf{f}]^2 \tag{1.36}$$

Integrating Eq. (1.36) from t = 0 to t = 2τ gives Eq. (1.37)

$$ln\left[\frac{A(2\tau)}{A(0)}\right] = -D\gamma^2[\int_0^{2\tau} \boldsymbol{F}(t)^2 dt - 4\boldsymbol{f}\int_0^{2\tau} \boldsymbol{F}(t)dt + 4\boldsymbol{f}^2\tau] \tag{1.37}$$

where

$$\mathbf{G(t)} = \begin{cases} g_0, & 0 < t < t_1 \\ g_0 + g, & t_1 < t < t_1 + \delta < \tau \\ g_0, & t_1 + \delta < t < t_1 + \Delta \\ g_0 + g, & t_1 + \Delta < t < t_1 + \Delta + \delta < 2\tau \\ g_0, & t_1 + \Delta + \delta < t \end{cases}$$

The definition of **G** (t) in this discrete time interval shows the simplest pulse gradient spin-echo (PSGE) (Fig. 1 – 7). The final result of Eq. (1.37) is shown in Eq. (1.38)

$$\ln\left[\frac{dA(2\tau)}{A(0)}\right] = -D(\gamma G\delta)^2\left(\Delta - \frac{\delta}{3}\right) \tag{1.38}$$

where

$$\mathrm{b} = (\gamma G\delta)^2\left(\Delta - \frac{\delta}{3}\right) \tag{1.39}$$

Eq. (1.38) is the famous Stejskal-Tanner equation, and b value (Eq. (1.39)), the so-called gradient-sensitization parameter, reflects how diffusion is weighted by G (the gradient strength), δ (the duration of each gradient pulse), and Δ (the time between the two gradient pulses). D is a diffusion coefficient, γ is gyromagnetic ratio, and the effective diffusion time (T) is Δ – δ/3. Subsequently, according to Stejskal and Tanners' report, applied pulse gradient reduced signal

intensities (Fig. 1 – 13). According to Eq. (1.38), diffusion coefficient, D, is calculated from two different intensities, A (2τ) and A (0), and two different b values.

Tissues are highly heterogeneous media that consists of various compartments and barriers. Thus, water molecules are restricted by microstructures and interact with cell membranes, and intracellular organelles [50]. The diffusion coefficient of water molecules is not free. Therefore, Le Bihan introduced the apparent diffusion coefficient (ADC) [51] to replace physical diffusion coefficient D. Diffusion MRI provides an approach to observe the water displacement in tissues and reveals information about the presence of microscopic obstacles/structures and geometric organization of tissues by ADC (Fig. 1 – 14).

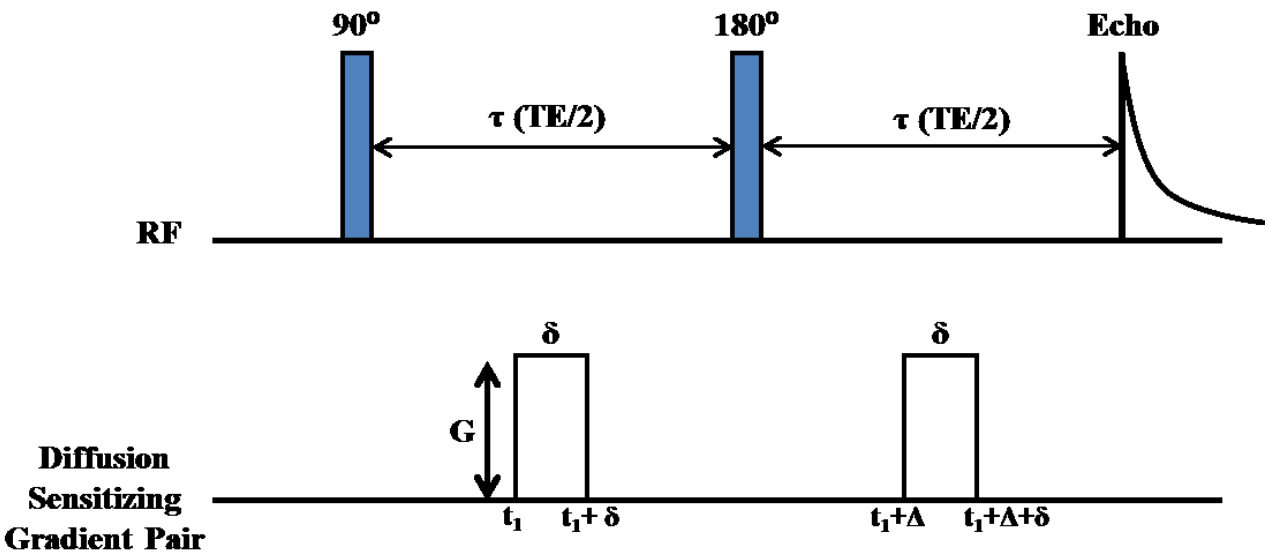

Figure 1 – 12 Stejskal-Tanner Pulse-Gradient Spin-Echo with square-wave diffusion sensitizing gradients. G is gradient strength, δ is duration of diffusion sensitizing gradient, Δ is time interval between diffusion-sensitizing gradient pair, and τ is the time interval between 90º and 180º RF pulses.

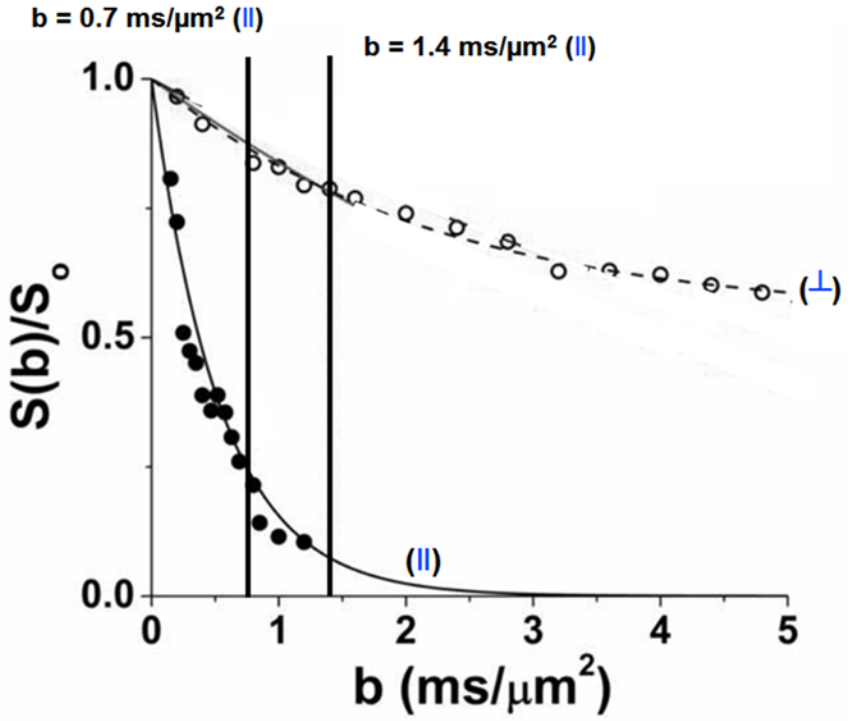

Figure 1 – 13 According to Stejskal-Tanner equation (Eq. (1.38)), applied pulse gradient reduced signal intensity (there was phase difference among spins, and net magnetization was decreased).Figure shows signal attenuation curves (mono-exponential decay) with different b values (only changing gradient strengths) either parallel or perpendicular to mouse optic nerve (highly coherent white-matter tract). The overall signal with gradient direction perpendicular to optic nerve was higher than the other direction since spins were 'trapped' within and by cylindrical axonal fibers, and thus could not easily move. When the diffusion gradient was applied along the optic nerve, spins were not restricted by optic nerve. Subsequently, they were affected by applied gradients easily and resulted in reduced signal due to obvious phase difference. Signal decay for b values less than 1.4 and 0.7 ms/μm^2 for perpendicular and parallel direction was close to mono-exponential decay; the exponential decay constant within those regions was the apparent diffusion coefficient (ADC).

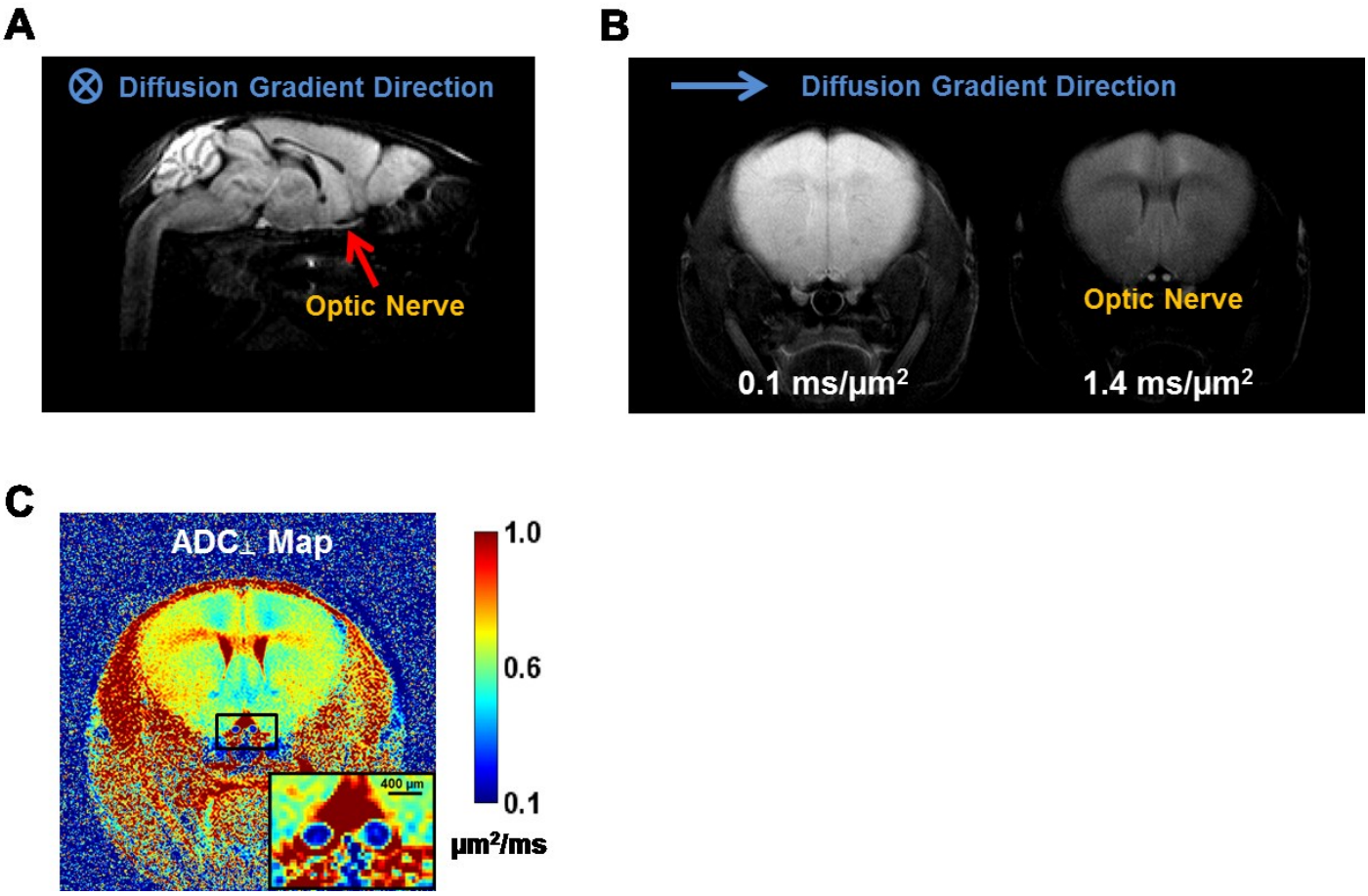

Figure 1 – 14 Diffusion-weighted image (DWI) of whole mouse brain (sagittal view) (A). Diffusion-sensitizing gradients were applied perpendicular to page, producing images which clearly reveal the optic nerve (A, red arrow). Based on the result in (A), we adjusted another image plan that was perpendicular to the optic nerves. Then, we could obtain another two DWIs with gradient direction from left to right with two b values (B). The DWIs in (A) and (B, which was applied with higher b value) show that the surrounding CSF was suppressed and reflected optic nerve structure clearly. According to Stejskal-Tanner equation (Eq. (1.38)), we calculated $ADC_{\perp}$ map (C) from two DWIs (B). The $ADC_{\perp}$ of optic nerves were lower than other moues brain tissues suggests that applied gradient was perpendicular to optic nerves, and spins in the optic nerves didn't have severe phase differences. Comparing to other mouse brain tissue, the signal intensity of optic nerves is considerably higher.

1.8 Magnetic Resonance Imaging (MRI) as a bio-marker to assess functional deficits

The discussion in the section 1.7.1 shows that MRI could reflect tissue contrast due to different T1 and T2 relaxation time. The first 2D MR image was introduced by Lauterbur [52]. In that paper, he used paramagnetic Mn^{2+} to show relaxation time could affect signal intensity. Therefore, Mn^{2+} was the first MRI contrast agent. Recently, manganese-enhanced MRI (MEMRI) has been widely used in animal studies, including mouse [53, 54, 11], rat [55-57], songbird [58], and monkey[59]. Manganese (Mn^{2+}), a calcium (Ca^{2+}) analog, enters cells through voltage-gated Ca^{2+} channels. After entry into the cell, Mn^{2+} is transported by fast axonal transport in vesicles and released into the synaptic cleft [54, 60]. Because Mn^{2+} is paramagnetic, it reduces T1 relaxation in tissue water and produces concentration-dependent hyper-intensities in T1-weighted (T1W) imaging [61] (Fig. 1 – 15). Therefore, Mn^{2+} can serve as both contrast agent and axonal transport tracer. Taking the visual system as an example, MEMRI provides a potential approach to track the pathway from retinal ganglion cell (inner layer of retina), optic nerve, to contralateral optic tract and superior colliculus. However, the cellular toxicity of Mn^{2+} has long been recognized [61, 62]. In Chapter 2, we compared functional effects of topical loading or intravitreal injection with working dosage. Briefly, topical loading with higher concentration of $MnCl_2$ damaged photoreceptor layers but not optic nerve. After optimizing working dosage, we applied MEMRI to EAE mice with optic neuritis to compare differences in axonal transport rates. We found that at the onset of optic neuritis in EAE mice, a significantly decreased axonal transport rate was observable (detailed in Chapter 3).

In section 1.7.2, we mentioned that ADC from diffusion MRI measurement can reflect the tissue structures or geometric orientation. We further proposed that ADC is a potential means to directly reveal axonal activity. Le Bihan et al. have reported that in human visual cortex,

signal intensity increased (ADC decreased) in diffusion-weighted image (DWI) during visual stimulation [63]. However, Miller et al. reported that such signal/ADC change in human visual cortex might result from a vascular contribution [64]. In white matter, blood oxygen level dependent (BOLD) fMRI is not easy to perform due to less blood flow and blood volume [65]. Therefore, in Chapter 4, we introduced our recent finding that during visual stimulation, decreased $ADC_{\perp}$ in mouse optic nerve (gradient direction was perpendicular to optic nerve) was observed and excluded vascular contribution as well. Such $ADC_{\perp}$ change might be related to extracellular space shrinkage due to stimulation-associated change in size or shape of glial cells or osmotic water shift across membrane. In Chapter 5, we further applied diffusion fMRI to EAE mice with optic neuritis. Then, we compared $ADC_{\perp}$ change of EAE and sham mice during visual stimulation. The results showed that activation-associated $ADC_{\perp}$ change of EAE mice was less than sham mice.

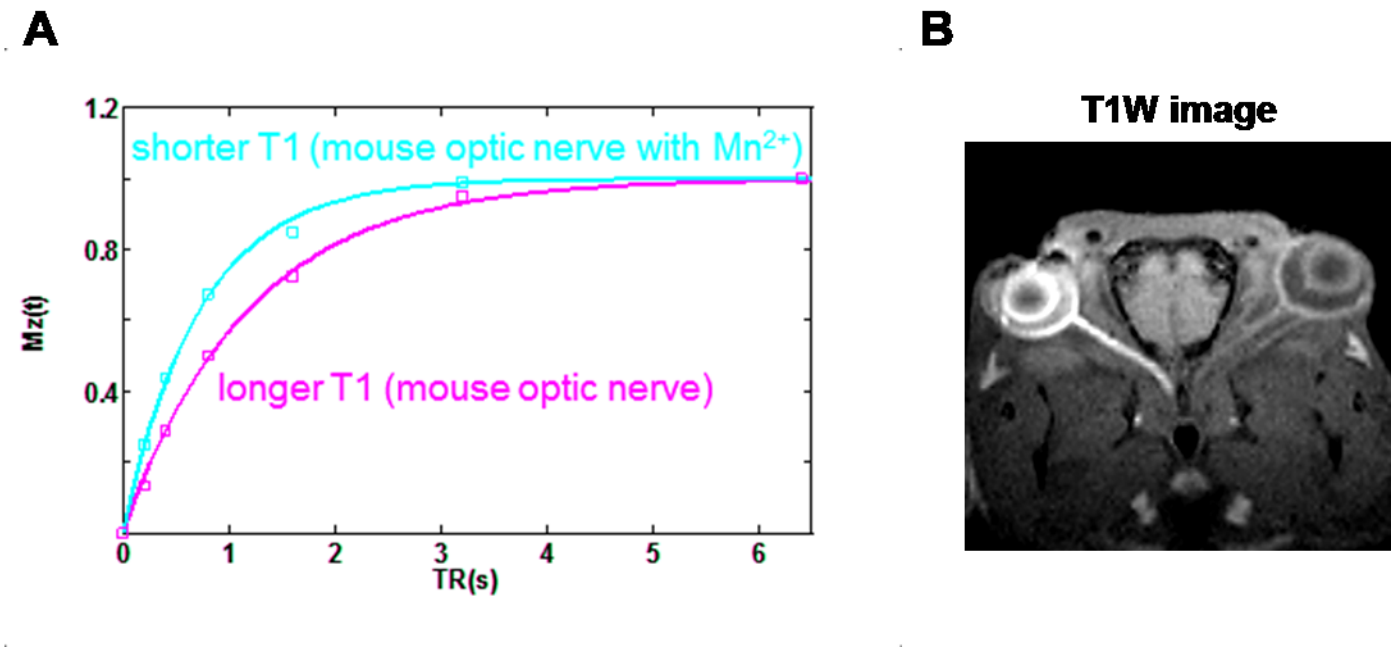

Figure 1 – 15 The T1 relaxation curves of mouse optic nerve with and without Mn^{2+} loading at a 4.7 T animal scanner with multiple TR (from 200 ms to 10 s, figure only showed TR from 0 to 6.5 s) and minimal TE using stand spin-echo sequence (A). The measurement was performed one day after intravitreal Mn^{2+} injection with 0.25μL of 0.2 M $MnCl_2$ (A). Open symbols are experimental data and solid lines are fitting curves, and T1 of Mn^{2+}-loading and normal mouse optic nerve is ~1.1 and 1.5 s, respectively. Since Mn^{2+} reduces T1 relaxation time in tissue water, Mn^{2+}-loading mouse optic nerve shows hyper-intensities in T1-weighted image (B, left optic nerve).

1.9 Reference

1. Filippi, M., et al., *Association between pathological and MRI findings in multiple sclerosis.* Lancet Neurol, 2012. **11**(4): p. 349-60.

2. Waxman, S.G., *Axonal conduction and injury in multiple sclerosis: the role of sodium channels.* Nat Rev Neurosci, 2006. **7**(12): p. 932-41.

3. Mao, P. and P.H. Reddy, *Is multiple sclerosis a mitochondrial disease?* Biochim Biophys Acta, 2010. **1802**(1): p. 66-79.

4. Compston, A. and A. Coles, *Multiple sclerosis.* Lancet, 2008. **372**(9648): p. 1502-17.

5. Simmons, S.B., et al., *Modeling the heterogeneity of multiple sclerosis in animals.* Trends Immunol, 2013.

6. Lublin, F.D. and S.C. Reingold, *Defining the clinical course of multiple sclerosis: results of an international survey. National Multiple Sclerosis Society (USA) Advisory Committee on Clinical Trials of New Agents in Multiple Sclerosis.* Neurology, 1996. **46**(4): p. 907-11.

7. Ohno, N., et al., *Myelination and axonal electrical activity modulate the distribution and motility of mitochondria at CNS nodes of Ranvier.* J Neurosci, 2011. **31**(20): p. 7249-58.

8. Kann, O. and R. Kovacs, *Mitochondria and neuronal activity.* Am J Physiol Cell Physiol, 2007. **292**(2): p. C641-57.

9. Stys, P.K., *General mechanisms of axonal damage and its prevention.* J Neurol Sci, 2005. **233**(1-2): p. 3-13.

10. Su, K.G., et al., *Axonal degeneration in multiple sclerosis: the mitochondrial hypothesis.* Curr Neurol Neurosci Rep, 2009. **9**(5): p. 411-7.

11. Sharma, R., et al., *Hyperglycemia induces oxidative stress and impairs axonal transport rates in mice.* PLoS One, 2010. **5**(10): p. e13463.

12. Smith, K.J. and H. Lassmann, *The role of nitric oxide in multiple sclerosis.* Lancet Neurol, 2002. **1**(4): p. 232-41.

13. Hooper, D.C., et al., *Prevention of experimental allergic encephalomyelitis by targeting nitric oxide and peroxynitrite: implications for the treatment of multiple sclerosis.* Proc Natl Acad Sci U S A, 1997. **94**(6): p. 2528-33.

14. Kornek, B., et al., *Distribution of a calcium channel subunit in dystrophic axons in multiple sclerosis and experimental autoimmune encephalomyelitis.* Brain, 2001. **124**(Pt 6): p. 1114-24.

15. Andrews, H.E., et al., *Mitochondrial dysfunction plays a key role in progressive axonal loss in Multiple Sclerosis.* Med Hypotheses, 2005. **64**(4): p. 669-77.

16. Beck, R.W., et al., *High- and low-risk profiles for the development of multiple sclerosis within 10 years after optic neuritis: experience of the optic neuritis treatment trial.* Arch Ophthalmol, 2003. **121**(7): p. 944-9.

17. Beck, R.W., et al., *The effect of corticosteroids for acute optic neuritis on the subsequent development of multiple sclerosis. The Optic Neuritis Study Group.* N Engl J Med, 1993. **329**(24): p. 1764-9.

18. *Multiple sclerosis risk after optic neuritis: final optic neuritis treatment trial follow-up.* Arch Neurol, 2008. **65**(6): p. 727-32.

19. Arnold, A.C., *Evolving management of optic neuritis and multiple sclerosis.* Am J Ophthalmol, 2005. **139**(6): p. 1101-8.

20. Polman, C.H., et al., *Diagnostic criteria for multiple sclerosis: 2010 revisions to the McDonald criteria.* Ann Neurol, 2011. **69**(2): p. 292-302.

21. Brusa, A., S.J. Jones, and G.T. Plant, *Long-term remyelination after optic neuritis: A 2-year visual evoked potential and psychophysical serial study.* Brain, 2001. **124**(Pt 3): p. 468-79.

22. Kupersmith, M.J., et al., *Contrast-enhanced MRI in acute optic neuritis: relationship to visual performance.* Brain, 2002. **125**(Pt 4): p. 812-22.

23. Naismith, R.T., et al., *Optical coherence tomography is less sensitive than visual evoked potentials in optic neuritis.* Neurology, 2009. **73**(1): p. 46-52.

24. Frohman, E.M., L.J. Balcer, and P.A. Calabresi, *Multiple sclerosis: can retinal imaging accurately detect optic neuritis?* Nat Rev Neurol, 2010. **6**(3): p. 125-6.

25. Berard, J.L., et al., *Characterization of relapsing-remitting and chronic forms of experimental autoimmune encephalomyelitis in C57BL/6 mice.* Glia, 2010. **58**(4): p. 434-45.

26. Gold, R., C. Linington, and H. Lassmann, *Understanding pathogenesis and therapy of multiple sclerosis via animal models: 70 years of merits and culprits in experimental autoimmune encephalomyelitis research.* Brain, 2006. **129**(Pt 8): p. 1953-71.

27. Matsunaga, Y., et al., *Visual functional and histopathological correlation in experimental autoimmune optic neuritis.* Invest Ophthalmol Vis Sci, 2012. **53**(11): p. 6964-71.

28. Meyer, R., et al., *Acute neuronal apoptosis in a rat model of multiple sclerosis.* J Neurosci, 2001. **21**(16): p. 6214-20.

29. Bettelli, E., et al., *Myelin oligodendrocyte glycoprotein-specific T cell receptor transgenic mice develop spontaneous autoimmune optic neuritis.* J Exp Med, 2003. **197**(9): p. 1073-81.

30. Ridder, W.H., 3rd and S. Nusinowitz, *The visual evoked potential in the mouse--origins and response characteristics.* Vision Res, 2006. **46**(6-7): p. 902-13.

31. Andermann, M.L., et al., *Functional specialization of mouse higher visual cortical areas.* Neuron, 2011. **72**(6): p. 1025-39.

32. Godement, P., J. Salaün, and C.A. Mason, *Retinal axon pathfinding in the optic chiasm: Divergence of crossed and uncrossed fibers.* Neuron, 1990. **5**(2): p. 173-186.

33. Douglas, R.M., et al., *Independent visual threshold measurements in the two eyes of freely moving rats and mice using a virtual-reality optokinetic system.* Vis Neurosci, 2005. **22**(5): p. 677-84.

34. Prusky, G.T., et al., *Rapid quantification of adult and developing mouse spatial vision using a virtual optomotor system.* Invest Ophthalmol Vis Sci, 2004. **45**(12): p. 4611-6.

35. Chiang, C.W., et al., *Acute visual function impairment in EAE is primarily caused by optic nerve inflammation as assessed by DBSI.* Proc. Intl. Soc. Mag. Reson. Med. 20, 3085, 2012.

36. Ge, Y., *Multiple sclerosis: the role of MR imaging.* AJNR Am J Neuroradiol, 2006. **27**(6): p. 1165-76.

37. Boretius, S., et al., *MRI of optic neuritis in a rat model.* Neuroimage, 2008. **41**(2): p. 323-34.

38. Diem, R., et al., *Autoimmune optic neuritis in the common marmoset monkey: comparison of visual evoked potentials with MRI and histopathology.* Invest Ophthalmol Vis Sci, 2008. **49**(8): p. 3707-14.

39. Gadjanski, I., et al., *Role of n-type voltage-dependent calcium channels in autoimmune optic neuritis.* Ann Neurol, 2009. **66**(1): p. 81-93.

40. Guy, J., *MRI in experimental inflammatory and mitochondrial optic neuropathies.* NMR Biomed, 2008. **21**(9): p. 968-77.

41. Hickman, S.J., *Optic nerve imaging in multiple sclerosis.* J Neuroimaging, 2007. **17 Suppl 1**: p. 42S-45S.

42. Sun, S.W., et al., *Selective vulnerability of cerebral white matter in a murine model of multiple sclerosis detected using diffusion tensor imaging.* Neurobiol Dis, 2007. **28**(1): p. 30-8.

43. Purcell, E.M., H.C. Torrey, and R.V. Pound, *Resonance Absorption by Nuclear Magnetic Moments in a Solid.* Physical Review, 1946. **69**(1-2): p. 37-38.

44. Bloch, F., *Nuclear Induction.* Physical Review, 1946. **70**(7-8): p. 460-474.

45. Buxton, R.B., *Introduction to functional magnetic resonance imaging : principles and techniques*. 2nd ed2009, Cambridge ; New York: Cambridge University Press. p. 425-439.

46. Plewes, D.B. and W. Kucharczyk, *Physics of MRI: A primer.* Journal of Magnetic Resonance Imaging, 2012. **35**(5): p. 1038-1054.

47. Torrey, H.C., *Bloch Equations with Diffusion Terms.* Physical Review, 1956. **104**(3): p. 563-565.

48. Stejskal, E.O. and J.E. Tanner, *Spin Diffusion Measurements: Spin Echoes in the Presence of a Time-Dependent Field Gradient.* The Journal of Chemical Physics, 1965. **42**(1): p. 288-292.

49. Kuchel, P.W., et al., *Stejskal-tanner equation derived in full.* Concepts in Magnetic Resonance Part A, 2012. **40A**(5): p. 205-214.

50. Hagmann, P., et al., *Understanding diffusion MR imaging techniques: from scalar diffusion-weighted imaging to diffusion tensor imaging and beyond.* Radiographics, 2006. **26 Suppl 1**: p. S205-23.

51. Le Bihan, D., et al., *MR imaging of intravoxel incoherent motions: application to diffusion and perfusion in neurologic disorders.* Radiology, 1986. **161**(2): p. 401-7.

52. Lauterbur, P.C., *Image Formation by Induced Local Interactions - Examples Employing Nuclear Magnetic-Resonance.* Nature, 1973. **242**(5394): p. 190-191.

53. Bearer, E.L., et al., *Role of neuronal activity and kinesin on tract tracing by manganese-enhanced MRI (MEMRI).* Neuroimage, 2007. **37 Suppl 1**: p. S37-46.

54. Smith, K.D., et al., *In vivo axonal transport rates decrease in a mouse model of Alzheimer's disease.* Neuroimage, 2007. **35**(4): p. 1401-8.

55. Chan, K.C., et al., *Evaluation of the retina and optic nerve in a rat model of chronic glaucoma using in vivo manganese-enhanced magnetic resonance imaging.* Neuroimage, 2008. **40**(3): p. 1166-74.

56. Olsen, O., et al., *Manganese transport in the rat optic nerve evaluated with spatial- and time-resolved magnetic resonance imaging.* J Magn Reson Imaging, 2010. **32**(3): p. 551-60.

57. Watanabe, T., J. Frahm, and T. Michaelis, *Functional mapping of neural pathways in rodent brain in vivo using manganese-enhanced three-dimensional magnetic resonance imaging.* NMR in Biomedicine, 2004. **17**(8): p. 554-568.

58. Van der Linden, A., et al., *In vivo manganese-enhanced magnetic resonance imaging reveals connections and functional properties of the songbird vocal control system.* Neuroscience, 2002. **112**(2): p. 467-474.

59. Saleem, K.S., et al., *Magnetic Resonance Imaging of Neuronal Connections in the Macaque Monkey.* Neuron, 2002. **34**(5): p. 685-700.

60. Millecamps, S. and J.P. Julien, *Axonal transport deficits and neurodegenerative diseases.* Nat Rev Neurosci, 2013. **14**(3): p. 161-76.

61. Silva, A.C., et al., *Manganese-enhanced magnetic resonance imaging (MEMRI): methodological and practical considerations.* NMR in Biomedicine, 2004. **17**(8): p. 532-543.

62. Koretsky, A.P. and A.C. Silva, *Manganese-enhanced magnetic resonance imaging (MEMRI).* NMR Biomed, 2004. **17**(8): p. 527-31.

63. Le Bihan, D., et al., *Direct and fast detection of neuronal activation in the human brain with diffusion MRI.* Proc Natl Acad Sci U S A, 2006. **103**(21): p. 8263-8.

64. Miller, K.L., et al., *Evidence for a vascular contribution to diffusion FMRI at high b value.* Proceedings of the National Academy of Sciences, 2007. **104**(52): p. 20967-20972.

65. Rostrup, E., et al., *Regional differences in the CBF and BOLD responses to hypercapnia: a combined PET and fMRI study.* Neuroimage, 2000. **11**(2): p. 87-97.

Chapter 2

Manganese-Enhanced MRI (MEMRI) via Topical Loading of Mn^{2+} Significantly Impairs Mouse Visual Acuity: A Comparison with Intravitreal Injection

This chapter represents the latest version of a manuscript that is targeted for submission to NMR in Biomedicine.

(Tsen-Hsuan Lin, Chia-Wen Chiang, Kathryn Trinkaus, William M. Spees, Peng Sun, and Sheng-Kwei Song)

Abstract

Purpose Manganese enhanced MRI (MEMRI) with topical loading of $MnCl_2$ provides comparable optic nerve enhancement as seen by intravitreal injection. However, the impact of this novel and noninvasive Mn^{2+} loading method on visual function remains undefined. The objective of this study is to determine the optimal topical Mn^{2+} loading dosage for MEMRI and to assess visual function after $MnCl_2$ loading. Intravitreal administration was performed to compare the two approaches of $MnCl_2$ loading.

Methods Twenty-four hours after topical loading of 0, 0.5, 0.75, and 1M $MnCl_2$, T1-weighted (T1W), T2-weighted (T2W), diffusion tensor image (DTI) and visual acuity were performed to determine the best topical loading dosage for MEMRI measurements and to assess the integrity

of retina and optic nerves. Mice were perfusion fixed immediately after *in vivo* experiments for H&E and immunohistochemistry staining.

Results Topical loading of 1 M $MnCl_2$ damaged the retinal photoreceptor layer with no detectable damage to optic nerves. For the topical loading, 0.75-M $MnCl_2$ was required to see sufficient enhancement of optic nerve. At this concentration the visual function was significantly affected followed by a slow recovery. Intravitreal injection (0.25 μL of 0.2 M $MnCl_2$) slightly affected visual acuity with full recovery a day later.

Conclusion Intravitreal Mn^{2+} injection provides more reproducible results with less adverse side effects than topical loading.

2.1 Introduction

Manganese (Mn^{2+}), as a calcium (Ca^{2+}) analog, enters cell bodies through voltage-gated Ca^{2+} channels. After entry into the cell, Mn^{2+} is transported by fast axonal transport in vesicles and released into the synaptic cleft [1]. Mn^{2+} produces a concentration-dependent shortening of tissue T1 due to its paramagnetic property. Therefore, Mn^{2+} can serve as both contrast agent and axonal transport tracer. T1-weighted (T1W) imaging is usually performed to monitor real-time Mn^{2+} transport reflected by the extent of enhancement in T1W MRI [2]. Therefore, MEMRI provides a potential approach to further explore the visual pathway from retinal ganglion cells, optic nerve, to contralateral optic tract and superior colliculus [3]. Indeed, manganese-enhanced MRI (MEMRI) has recently been used to investigate optic nerve axonal integrity [4-7], retinal projections to the superior colliculus through intravitreal injection of $MnCl_2$ [8], or layer-specific calcium-dependent retinal fMRI activation [9, 10].

The cellular toxicity of Mn^{2+} has long been recognized as overexposure causes Parkinsonism [11]. Therefore, it is important to determine optimal Mn^{2+} dosing, which is a tradeoff between maximizing MR detectability and minimizing toxicity [12]. The toxicity of $MnCl_2$ after intravitreal injection has been examined previously by histology and visual function measurements [13-15, 7, 16]. In an attempt to remedy the invasive intraocular injection of $MnCl_2$, Sun et al. proposed to deliver Mn^{2+} through topical loading [17]. Topical loading is a simple, noninvasive approach for Mn^{2+} delivery, achieved by dropping $MnCl_2$ solution directly onto the eye. The effect of repetitive topical $MnCl_2$ loading was recently examined reporting RGC loss after three bi-weekly applications of 1 M $MnCl_2$ while no RGC loss was observed after three monthly applications [18]. Corneal thickening was also observed after seven bi-weekly applications [18]. It appeared that increasing the time interval between repetitive topical

applications reduced adverse effects seen in RGC and cornea. In this study, the effect of topical and intravitreal loading of $MnCl_2$ was examined by assessing post-loading visual acuity and structural integrity of both retina (by high resolution in vivo T2-weighted MRI and histology) and optic nerves (by *in vivo* diffusion tensor imaging, i.e., DTI). Results suggest that intravitreal injection of $MnCl_2$ is safe with limited adverse effects when administered in small volume and low doses, sufficient to monitor axonal transport.

2.2 Materials and Methods

All experimental procedures were approved by Washington University's Animal Studies Committee and conformed to the NIH Policy on Responsibility for Care and Use of Animals and the ARVO Statement for the Use Animals in Ophthalmic and Vision Research.

2.2.1 Topical $MnCl_2$ Loading

Thirty-five female C57BL/6 mice obtained from Jackson Laboratory (Bar Harbor, ME) at 8 weeks of age underwent topical loading of 0 (n=5), 0.5 (n=5), 0.75 (n=15), or 1 M (n=10) of $MnCl_2$ in 0.9% saline. After anesthetized using 1.5-2% isoflurane/oxygen, a 30-µL drop of $MnCl_2$ was introduced covering the entire right eye. An additional 10µL of $MnCl_2$ was applied every 15 min to maintain the topical-fluid volume, different from the original procedure by Sun et al.[17], assuring a consistent loading among various lab personnel.

2.2.2 Intravitreal $MnCl_2$ Injection

An additional twenty 8-week old female C57BL/6 mice were employed to compare the "safe" injection volumes of 0.25 and 2 µL using saline (n=5 each group), and the "safe" dose

using 0.25 (n=5) and 0.125 (n=5) μL of 0.2-M $MnCl_2$ in saline. Mice, under 1.5-2% isoflurane/oxygen anesthesia, were placed on a custom-made head holder for intravitreal injection at 3-μL/min using a 34-gauge needle connected to a micro-injection pump (WPI Instrument, FL). After infusion, the needle was left in place for an extra 1 minute before withdrawal. A drop of topical antibiotic was applied after removing the injection needle [19].

2.2.3 Visual Acuity Assessment

Visual acuity (VA) was assessed using the OptoMotry Virtual Optometry System, (CerebralMechanics, Inc., Canada). Mice were placed on the platform inside the chamber with virtual rotating columns projected on four LCD monitors surrounding it. The spatial frequency in cycle/degree (c/d) starting from 0.1 c/d was incremented in steps of 0.05 c/d until the mouse stopped responding to the projected visual patterns, which was recorded as the VA [20, 21]. Thirty normal C57BL/6 mice were measured to establish the baseline VA for naïve animals. VA was measured before $MnCl_2$ loading and at days 1 through 7 after topical $MnCl_2$ loading, and at 4, 24, and 48 hours after intravitreal injection.

2.2.4 MRI: DTI and T1-weighted imaging of the visual pathway

Twenty-four hours after topical or intravitreal $MnCl_2$ loading, MRI measurements were performed on a 4.7T Agilent DiectDrive small-animal MRI system (Agilent Technologies, CA) equipped with a Magnex/Agilent HD gradient coil set (Magnex, Oxford, UK) with pulse gradient strength up to 58 G/cm and a gradient rise time ≤ 295 μs. Mice were anesthetized by isoflurane/oxygen (1.5%). Respiratory rate and body temperature were monitored during experiments using a MR compatible animal monitoring system (SA Instrument, Inc., NY). The body temperature was maintained at 37°C with a regulated circulating warm water pad placed

underneath mouse body along with regulated warm air blown into the magnet bore. An actively-decoupled 1.7-cm receive coil was placed on top of the mouse head. The animal holder assembly, including the receive coil was placed in an 8-cm active-decoupled volume transmit coil [22, 23].

2.2.4.1 T1-weighted Imaging

A 3D gradient echo sequence was employed to image mouse brain with the following parameters: TR= 15 ms, TE= 2.63 ms, flip angle 20°, number of averages 16, FOV 15×15×22 mm^3, data matrix size 128×128×64 (zero-filled to 256×256×128). Regions of interest (ROI) were manually outlined according to a previously published protocol[17] on the extracted 2D images containing retina, optic nerve, and superior colliculus using ImageJ software (NIH, http://bigwww.epfl.ch/sage/soft/watershed/, US). The ROI of the Mn^{2+}-loaded structures along the visual pathway was outlined and mean signal intensity was obtained using ImageJ. The signal intensity of the loaded ROI was normalized by the contralateral mean intensity to correct scan-to-scan sensitivity differences resulting from variable sample loading.

2.2.4.2 DTI of Optic Nerve

Optic nerve DTI was performed using a multi-echo spin-echo diffusion weighted imaging sequence (Tu et al., 2010) with the following parameters: TR=1.5 s, TE=34 ms (first echo time, including required time for diffusion-weighting gradients), inter-echo delay time 19 ms, FOV 22.5×22.5 mm^2, matrix size 192×192 (zero-filled to 384×384); in-plane resolution 117×117 mm^2 (prior to zero-filling), slice thickness 0.5 mm, two diffusion-sensitizing factors (b value) 0.0 and 1.0 ms/μm^2 (with δ = 5 ms and Δ = 18 ms). The standard six-direction diffusion encoding scheme was used, with $[G_x, G_y, G_z]$ = [1, 1, 0], [1, 0, 1], [0, 1, 1], [-1, 1, 0], [0, -1, 1], and [1, 0, -

1]. The image plane was adjusted to be as nearly perpendicular to optic nerve as possible to minimize partial volume effects. Fractional anisotropy (FA), axial ($\lambda_{\parallel}$) and radial ($\lambda_{\perp}$) diffusivity maps were generated from the image data by programs written in Matlab (MathWorks, Natick, MA).

2.2.5 T2-weighted Imaging of Retina

For retinal imaging, mice were anesthetized by intraperitoneal injection of ketamine (87 mg/kg) and xylazine (13 mg/kg) followed by constant subcutaneous infusion of ketamine (54 mg/kg/h)/xylazine (4 mg/kg/h). The infusion rate was adjusted to maintain the respiratory rate between 150 - 210 breaths/min during imaging. Retina imaging was performed on an Agilent 11.74 T DirectDrive small-animal MRI system using a spin-echo sequence with the following parameters: TR = 2 s, TE = 34 ms, FOV 12×12 mm^2, matrix size 256×256 (zero-filled to 512×512); in-plane resolution 47×47 μm^2 (prior to zero-filling), slice thickness 0.4 mm. All images were acquired on a nasal-temporal slice bisecting the eye through the retina and optic nerve head.

2.2.6 Histology

2.2.6.1 Optic nerve

Following MR experiments, mice were perfused with 4 % paraformaldehyde in phosphate-buffered saline (PBS). Brains were excised and post-fixed in fixative for 24 hours then transferred to 1% PBS for storage at 4°C until histological analysis. Mouse optic nerves were embedded in 2 % agar gel followed by paraffin embedding [24]. Five-μm thick transverse slices were sectioned for immunohistochemical staining. All sectioned tissues were deparaffinized, rehydrated, and blocked in solution mixed with 1% bovine serum albumin (BSA)

and 2% Triton-X100 for an hour at room temperature to prevent non-specific binding and to increase antibody permeability. Slides were incubated in monoclonal anti-phosphorylated neurofilament antibody (SMI-31; 1:2000, Covance) to stain non-injured axons, or in rabbit anti-myelin basic protein (MBP) antibody (1:1000 Sigma-Aldrich, MO) to stain myelin sheath at 4°C overnight. After rinsing, goat anti-mouse IgG or goat anti-rabbit IgG conjugated Alexa 488 (1:800, Invitrogen, CA) were applied to visualize immunoreactivity of phosphorylated neurofilaments and MBP. Finally, slides were covered using Vectashield Mounting Medium with 4′,6-diamidino-2-phenylindole (DAPI) (Vector Laboratory, Inc., Burlingame, CA). Histological slides were examined with Nikon Eclipse 80i fluorescence microscope. Images were captured with a black-and-white CCD camera using MetaMorph software (Universal Imaging Corporation, Sunnyvale, CA).

2.2.6.2 Retina

Mouse eyes were flash-frozen immediately after enucleation to avoid dehydration and fixation induced tissue distortion. Frozen-cut 8-µm-thick tissue sections were stained with hematoxylin and eosin (H&E) to assess the integrity of multiple retinal layers. Histological slices were scanned with Olympus NanoZoomer slide scanner (Hamamatsu Photonics, Hamamatsu, Japan). For quantitative analysis of H&E staining, scanned images were exported with NDP viewer software (Hamamatsu Photonics, Hamamatsu, Japan) with 20× objective. ROIs were selected to contain the retina segment with proximal and distal ends located at 250 and 800 µm away from the optic nerve head on both sides of the nerve head [25]. Within the ROIs, the retinal thickness was measured from nerve fiber layer to retina pigment epithelium every 55 µm (i.e., 10 measurements total). Ten measurements were averaged as the representative thickness for that side of retina.

2.2.6.3 Statistical analysis

Multiple comparisons for T1W enhancement in retina, optic nerve, and superior colliculus after Mn^{2+} loading were performed using a linear repeated measures model with adjustment for multiple testing using Tukey's HSD (honest significant difference). A linear repeated measures model was used to estimate the mean difference in VA between loaded and contralateral control eyes by dosages and day of experiment (from baseline to day 7). The effect of Mn^{2+} loading on the mean retinal thickness was assessed using a linear model on a log scale in each of the five study groups. Each Mn^{2+} treated group was compared with the saline control. P-values for the difference in mean retinal thickness were adjusted for multiple tests using Tukey's HSD.

2.3 Results

2.3.1 Topical $MnCl_2$ Loading

2.3.1.1 Manganese Enhanced T1W MRI

T1-weighted images of 1-M $MnCl_2$ loaded visual pathway including ipsilateral retina and optic nerve (ON), and contralateral lateral geniculate nucleus (LGN) and superior colliculus (SC) clearly demonstrated signal enhancement on these structures (Fig. 2 – 1A). The image of retina and optic nerve with 0.5, 0.75, and 1 M of $MnCl_2$ loading (Fig. 2 – 1B) suggested that both 1 and 0.75 M of $MnCl_2$ loading led to discernible signal enhancement in optic nerve while 0.5 M did not. Compared to the saline group, the group-averaged ROI analysis (Fig. 2 – 1C)

demonstrated that 0.75 and 1 M of $MnCl_2$ loading significantly enhanced all structures along the visual pathway.

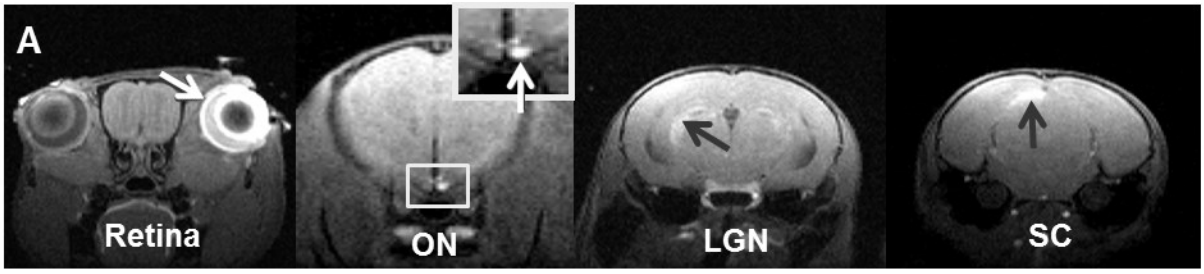
A
Retina
ON
LGN
SC

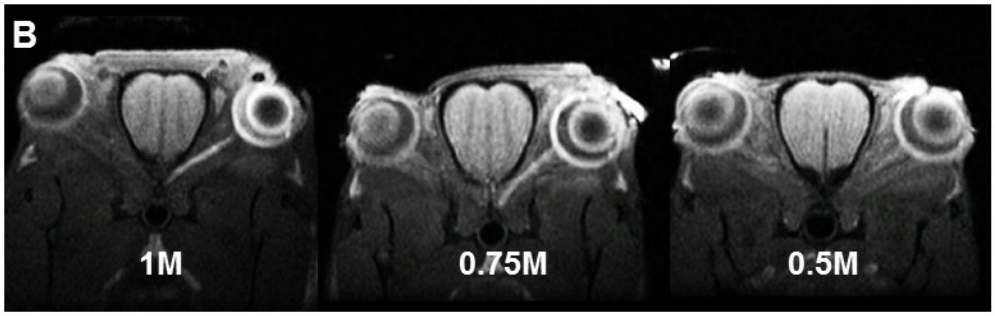
B
1M
0.75M
0.5M

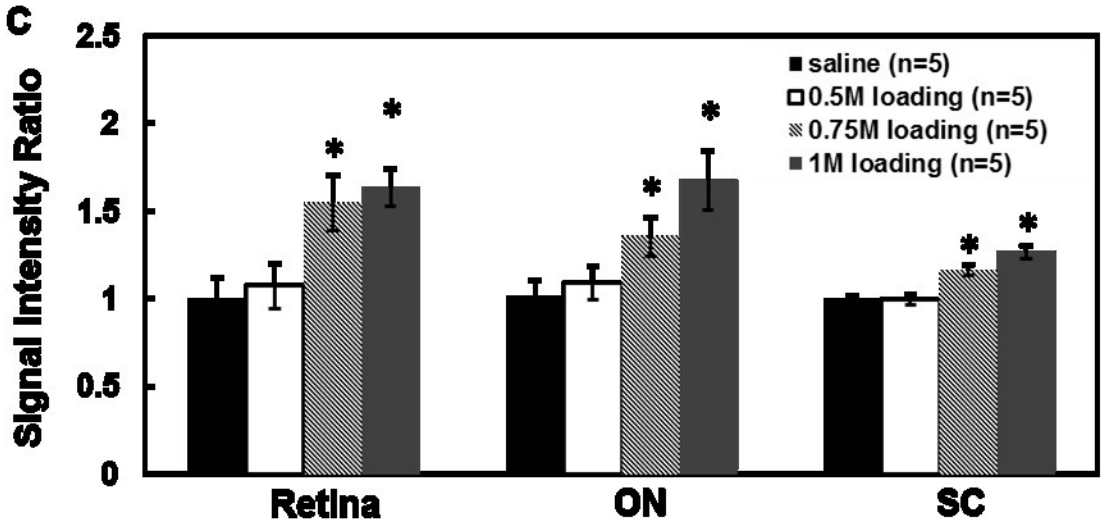
C
Signal Intensity Ratio
2.5
2
1.5
1
0.5
0
saline (n=5)
0.5M loading (n=5)
0.75M loading (n=5)
1M loading (n=5)
Retina
ON
SC

Figure 2 – 1 Representative T1W images acquired from a mouse brain at 24 hours after topical $MnCl_2$ loading (A), ipsilateral retina and optic nerve (ON), and contralateral lateral geniculate nucleus (LGN) and superior colliculus (SC) are enhanced with topical loading (arrows). The oblique images (B) bisecting retina and optic nerve after topical loading of 1, 0.75, and 0.5M $MnCl_2$ suggest that 0.75M $MnCl_2$ was sufficient to produce discernible enhancement of optic nerve. Bar graphs (C) demonstrate the signal intensity ratio between labeled and control retina, ON, and SC. With 1 and 0.75M $MnCl_2$ loading, a significant enhancement of the structures along the visual system (retina, ON, LGN, SC) was clearly seen. In contrast, only slight retinal enhancement was seen with 0.5M $MnCl_2$ loading. Therefore, 0.75M was the concentration selected for topical loading in this study.

* indicates that $P < 0.005$ compared to saline group via Tukey HSD test.

2.3.1.2 Visual Acuity

The VA of normal female C57BL/6 mice is 0.37 ± 0.03 c/d (mean ± SD; n=30). Topical loading of 1-M $MnCl_2$ caused total blindness (VA ~ 0 c/d) at one day after loading without recovery up to 7 days after loading (open squares; Fig. 2 – 2). A significant VA decrease in eyes following 0.75-M $MnCl_2$ loading was also observed (open circles; Fig. 2 – 2). However, the decreased VA gradually recovered to the normal range at day 5 (VA ≥ 0.3 c/d). Contralateral control eyes in animals treated without 1 and 0.75-M $MnCl_2$ loading were not affected throughout the time course (filled symbols, Fig. 2 – 2). Mice topically loaded with 0.5M $MnCl_2$ exhibited a slight VA decrease at one day after loading and recovered to normal at day 2; saline-loaded eyes exhibited normal VA throughout the time course (data not shown).

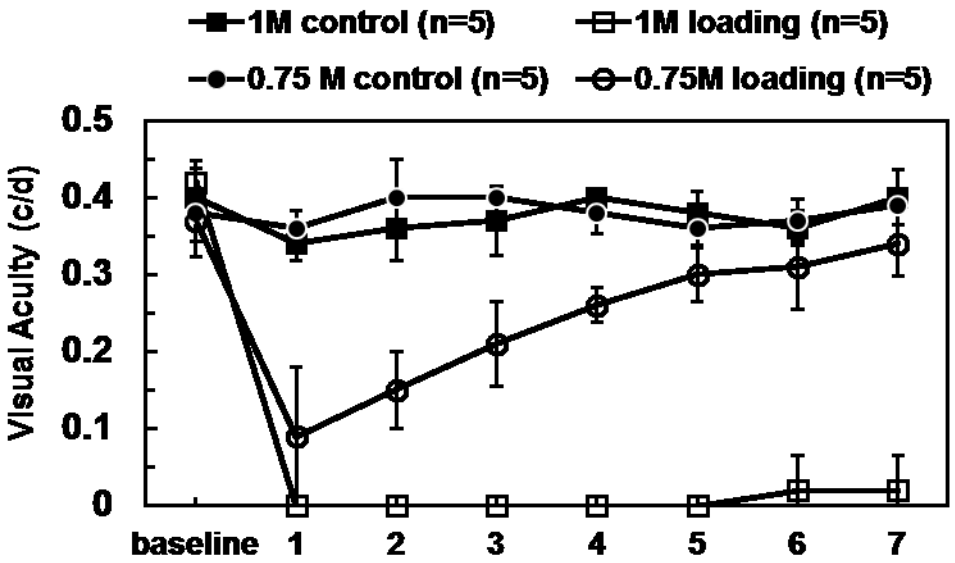

Figure 2 – 2 Visual acuity was measured daily in eyes after topical loading with 0.75 and 1M $MnCl_2$ (open symbols), and in contralateral, control eyes (filled symbols). Tests for difference between the dose groups indicate that there is no difference at baseline or on the first day of treatment. Between days 2 and 7, however, the difference between loaded and control eyes is not the same in the two different dosage groups (p-values < 0.0001 at days 2-7). At one day after 1M of $MnCl_2$ loading, the visual acuity decreased to zero (completely blind) and did not recover throughout the 7-day time course. In contrast, one day after 0.75M of $MnCl_2$ loading visual acuity decreased to 0.1c/d and recovered beginning on Day 2 ($p < 0.05$, compared to 1M loading eyes) until recovering back to the normal range by Day 6.

Note 1: mean VA of normal B6 mice (n=30) is 0.36 ± 0.03 (c/d; mean ± SD)

Note 2: c/d denotes units of cycles per degree

2.3.1.3 DTI and Immunohistochemistry of Optic Nerve

In vivo DTI of optic nerves was performed at days 1 and 7 after 1M $MnCl_2$ loading (VA = 0 c/d). Color-coded FA, maps derived from DTI analysis clearly delineated the optic nerves (Fig. 2 – 3A). There was no statistically-significant difference in group-averaged $\lambda_{\parallel}$ and $\lambda_{\perp}$ between the loaded and control optic nerves at days 1 and 7 after $MnCl_2$ loading (Fig. 2 – 3B). These DTI findings suggested that there was no detectable axon or myelin injury after topical $MnCl_2$ loading [26], supported by the immunohistochemical staining of phosphorylated neurofilaments (SMI-31; green dots in Fig. 2 – 3C) and myelin basic protein (MBP; red rings in Fig. 2 – 3C) from the same nerves after *in vivo* DTI.

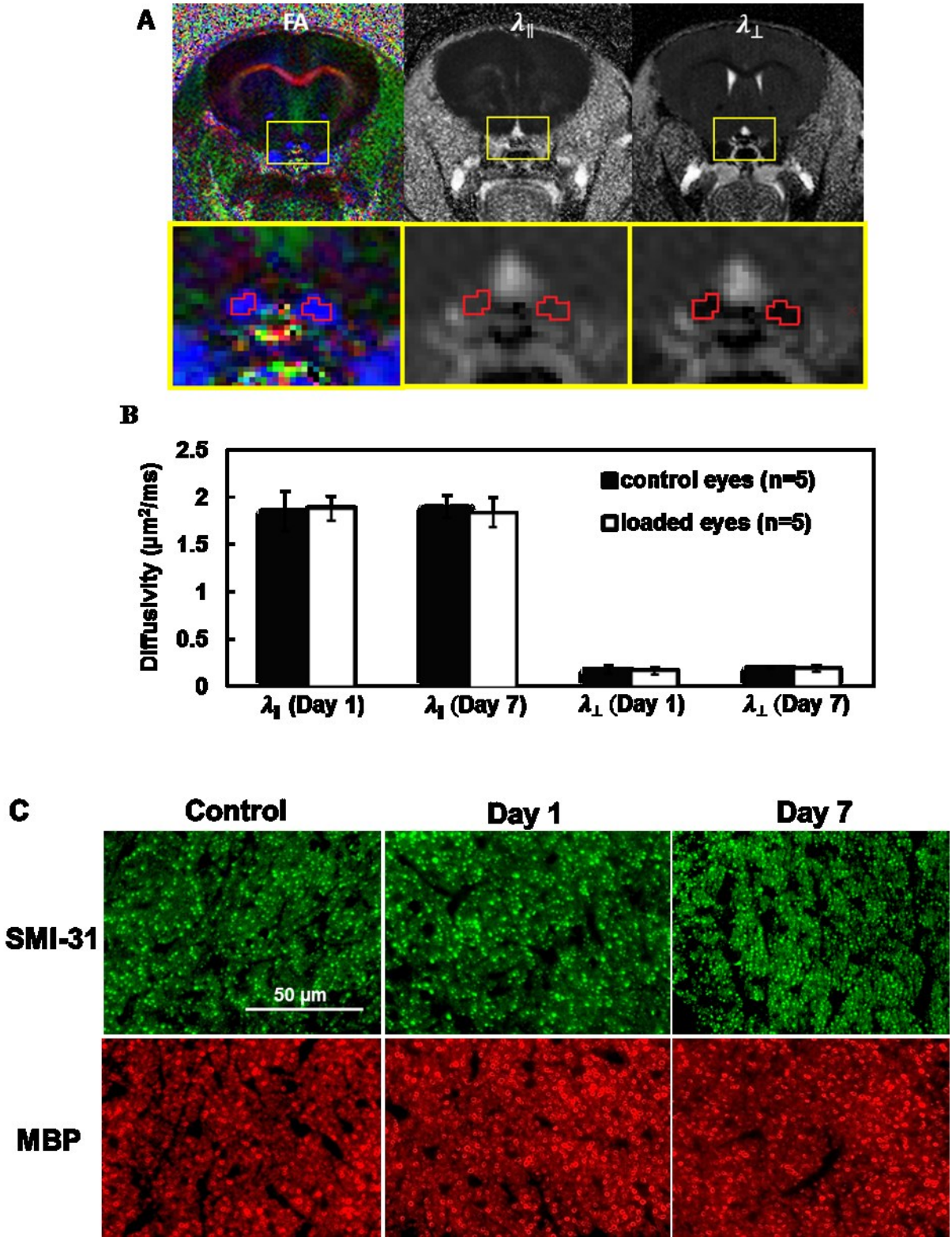
A
FA
$\lambda_{\parallel}$
$\lambda_{\perp}$
B
Diffusivity (μm²/ms)
2.5
2
1.5
1
0.5
0
control eyes (n=5)
loaded eyes (n=5)
$\lambda_{\parallel}$ (Day 1)
$\lambda_{\parallel}$ (Day 7)
$\lambda_{\perp}$ (Day 1)
$\lambda_{\perp}$ (Day 7)
C
Control
Day 1
Day 7
SMI-31
MBP
50 μm

Figure 2 – 3 Brain DTI maps, containing optic nerves, from mice at one and seven days after topical loading of 1M $MnCl_2$ were examined to assess the effect of Mn^{2+} on axonal integrity. The region-of-interest (ROI) based analysis was performed on diffusion metrics, including fractional anisotropy (FA), axial ($\lambda_{\parallel}$), and radial ($\lambda_{\perp}$) diffusivity, from each optic nerve (A, outline in red). At one and seven days after 1M of $MnCl_2$ loading, there was no difference in $\lambda_{\parallel}$ and $\lambda_{\perp}$ between the optic nerves from the control (B, black bars) and loaded (white bars) eyes suggesting no axon or myelin injury upon Mn^{2+} loading. The matched immunohistochemical staining of phosphorylated neurofilament (SMI-31) and myelin basic protein (MBP) strongly support the axonal and myelin sheath integrity seen by *in-vivo* DTI (C).

2.3.1.4 T2W Images and H&E Staining of Retina

T2W images acquired from retinas in control and topical-loading mice at day 7 after 1M $MnCl_2$ loading revealed the previously reported dark-bright-dark layer contrast of the control retinas [27, 28] (Fig. 2 – 4A and 2 – 4B). Significant thinning of the retina was seen in the 1M $MnCl_2$ loaded eyes (Fig. 2 – 4C and 2 – 4D). Retinal layers examined by H&E staining showed significant cell swelling (~26 % increased thickness) at day 1 (VA = 0 c/d; the time point of best T1W enhancement) and significant retinal thinning (~31 %) at day 7 (VA = 0 c/d) after 1M $MnCl_2$ loading (Fig. 2 – 4E and 2 – 4F). A slight swelling of the retina was seen at day 1 after 0.75M $MnCl_2$ loading with recovery to the normal thickness at day 5 (VA $\geq$ 0.3 c/d). Retina with saline loading exhibited the same thickness as that reported in the literature for normal mice (Fig. 2 – 4E and 2 – 4F) [25, 19].

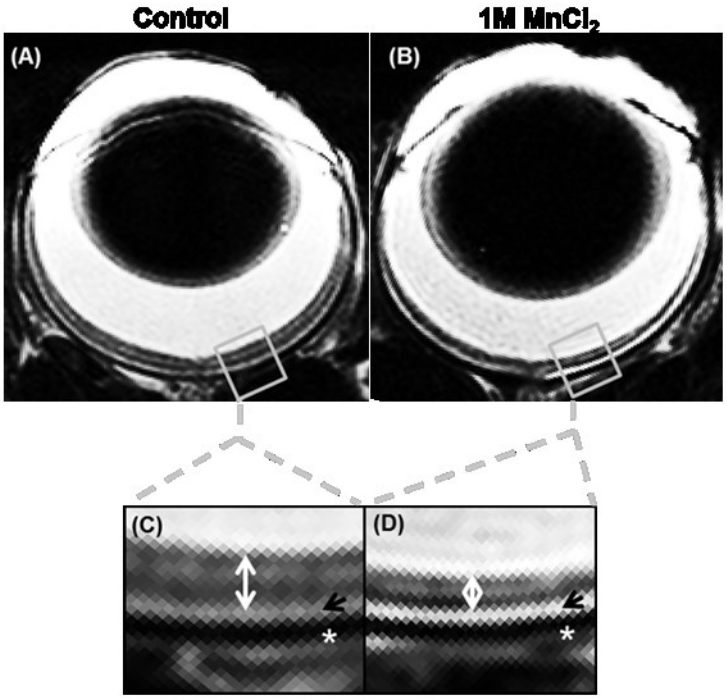
Control
1M MnCl2
(A)
(B)
(C)
(D)
*
*

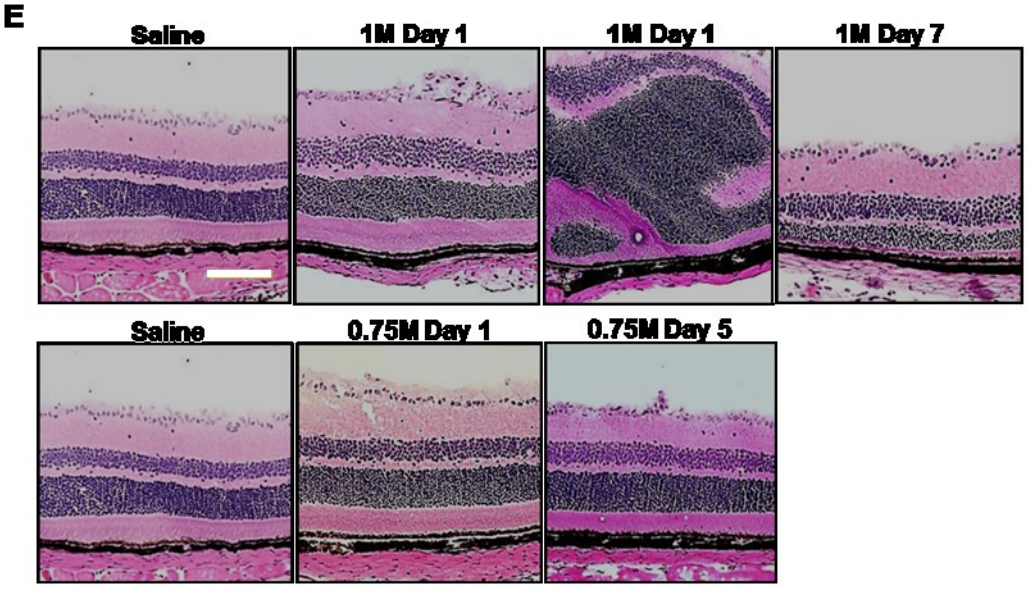
E
Saline
1M Day 1
1M Day 1
1M Day 7
Saline
0.75M Day 1
0.75M Day 5

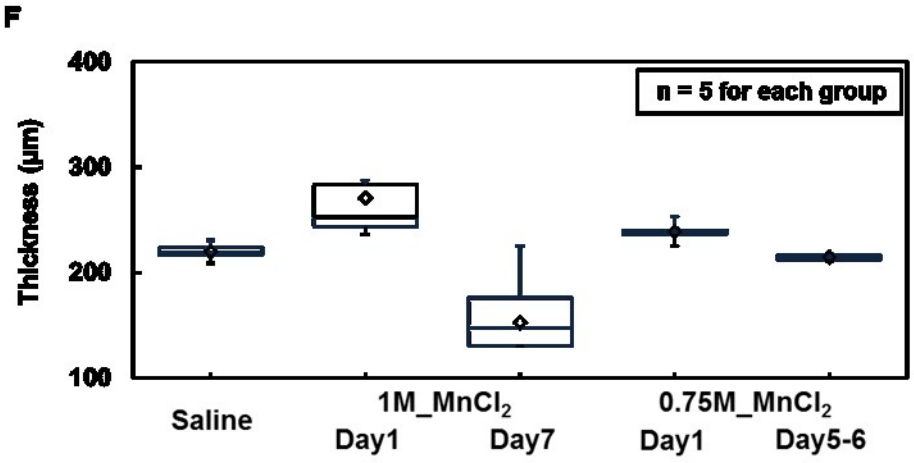
F
Thickness (μm)
400
300
200
100
n = 5 for each group
Saline
1M_MnCl2
Day1
Day7
0.75M_MnCl2
Day1
Day5-6

Figure 2 – 4 *In-vivo* T2-weighted (T2W) imaging was performed to compare the retinal thickness between the saline (sham) (A) and $MnCl_2$-loaded (B) eyes. Zoom-in images of mouse retina (C and D) seven days after topical loading of 1M of $MnCl_2$ exhibit typical T2W MRI features of a mouse retina wherein sclera appears dark (white stars), choroid is bright (black arrows), and retinal layers (white double-headed arrows) exhibit intensities between sclera and choroid. Clear thinning in Mn^{2+} loaded retina was seen 7 days after topical loading in T2W MRI. The hematoxylin and eosin (H&E) staining of the frozen-embedded retina confirmed the MRI detected retinal thinning (E). At 24 hours after 1 M $MnCl_2$ loading, heterogeneous retinal swelling was observed. On day 7 after 1M $MnCl_2$ loading, photoreceptor layers degeneration was visible. 0.75 M $MnCl_2$ loading caused retina slightly swelling at day 1 but recovery at day 5 (E). To quantify the extent of retinal thickness change, H&E images were analyzed (F). A linear model was used to estimate mean retinal thickness on a log scale in each of the 5 study groups. Each of the $MnCl_2$ treated groups was compared with the saline control. P-values for the difference in mean retinal thickness are adjusted for multiple testing using Tukey's HSD test. One day after 1M $MnCl_2$ loading, transient significant swelling of retina ($p < 0.005$, with blindness) was seen followed by significant retinal thinning at Day 7 ($p < 0.005$, with no recovery of visual function). At 0.75M of $MnCl_2$ loading, mild retinal swelling was seen at 1 day (significantly-decreased VA without blindness), which returned to normal thickness 7 days after loading (visual acuity returned to normal by 5-6 days post-loading).

Diamond symbols: mean value

Scale bar: 100 μm

2.3.2 Effect of Intravitreal Injection

2.3.2.1 Volume Effect

There was no change in VA of eyes receiving intravitreal 0.25-μL saline injection (Fig. 2 – 5A). In contrast, VA impairment was seen in eyes at 4 and 24 hours after intravitreal 2-μL saline injection, which recovered at 48 hours (Fig. 2 – 5A). Histological examinations revealed significant retinal swelling (~17% increase in thickness) at 24 hours after 2μL-saline injection while no detectable difference was seen in eyes with 0.25-μL saline injection or topical saline loading (Fig. 2 – 5C and 2 – 5D).

2.3.2.2 Dose Effect

Sufficient T1W enhancement in the visual pathway was seen 24 hours after intravitreal injection of 0.25-μL 0.2-M (50 nmol) $MnCl_2$ (Fig. 2 – 5B) as previously reported [13]. In contrast, we failed to see a detectable T1W enhancement in the visual pathway using the other reported dosage [13], 0.125-μL 0.2-M $MnCl_2$, (25 nmol; data not shown). In the 50 nmol dosage group, histological analysis of retina using H&E staining showed slight cell swelling at 4 hours, which recovered at 24 hours post-injection (Fig. 2 – 5C and 2 – 5D).

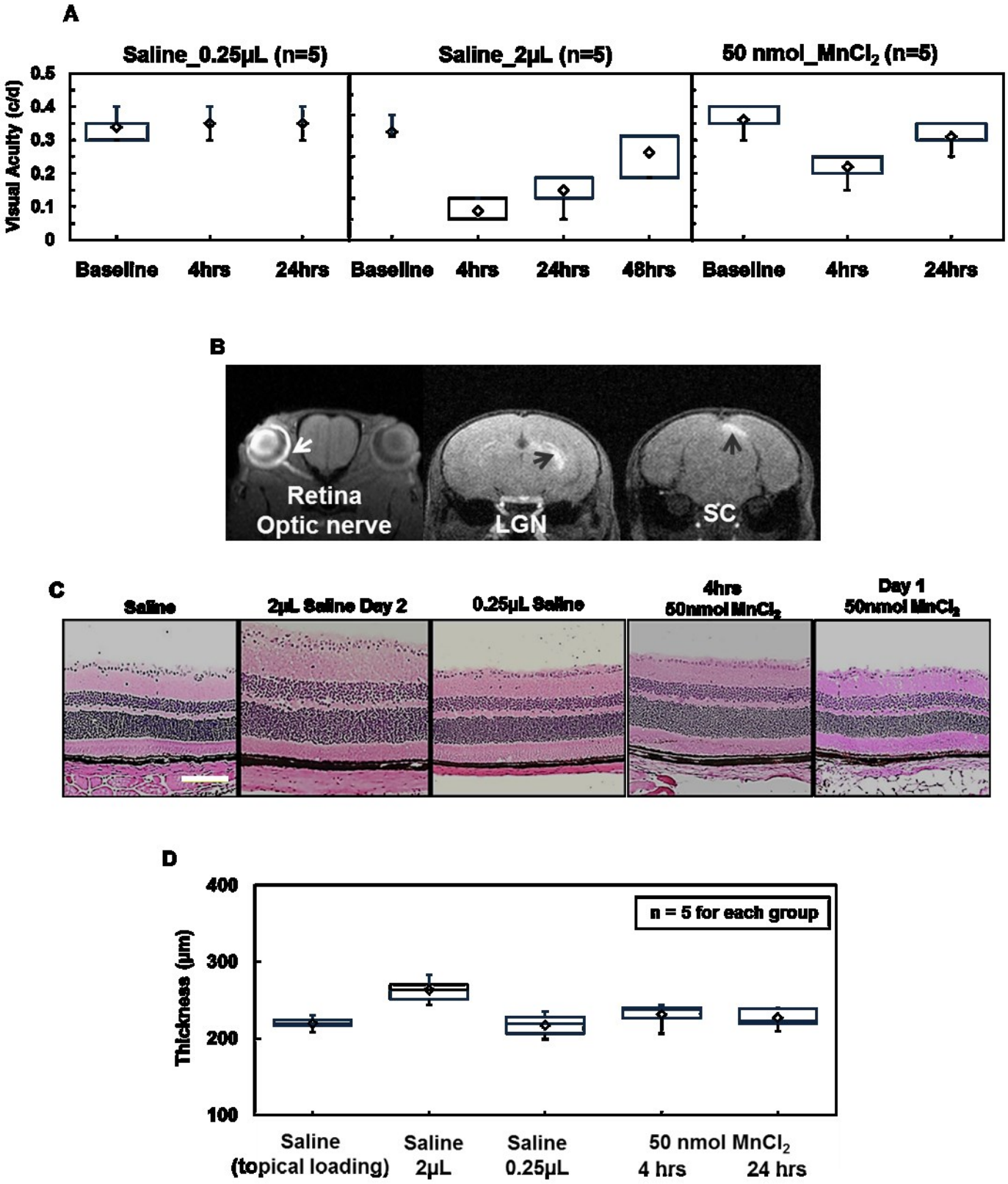
A
Saline_0.25µL (n=5)
Saline_2µL (n=5)
50 nmol_MnCl2 (n=5)
Visual Acuity (c/d)
0.5
0.4
0.3
0.2
0.1
0
Baseline
4hrs
24hrs
Baseline
4hrs
24hrs
48hrs
Baseline
4hrs
24hrs
B
Retina
Optic nerve
LGN
SC
C
Saline
2µL Saline Day 2
0.25µL Saline
4hrs
50nmol MnCl2
Day 1
50nmol MnCl2
D
Thickness (µm)
400
300
200
100
n = 5 for each group
Saline
(topical loading)
Saline
2µL
Saline
0.25µL
50 nmol MnCl2
4 hrs
24 hrs

Figure 2 – 5 The effect of intravitreal Mn^{2+} injection on retinal integrity and visual function was examined on mouse eyes receiving 0.25 and 2 μL saline injection. The effect of injecting 0.25 and 2 μL on the visual acuity (VA) was examined where 2μL saline injection transiently impaired visual function at 4 hours and Day1 after injection, subsequently recovered (VA ≥ 0.3) at Day 2 (A). The injection of 0.25μL of saline did not impact VA (A). Representative T1W images (B) obtained at 24 hours post-injection with the working dosage (0.25μL and 0.2M $MnCl_2$, 50 nmol) demonstrate the effect of Mn^{2+}- induced intensity enhancement in the loaded visual pathway (left retina, left optic nerve, right LGN, and right SC). The VA was affected by the working dosage at 4 hours post-injection with nearly full recovery by 24 hours post-injection (A). Retinal thickness was examined with H&E staining of frozen-embedded mouse eyes (C and D). The previously reported safe intravitreal 2 μL saline injection caused retinal swelling at Day 2. In contrast, the other reported safe intravitreal saline injection (0.25 μL) indeed did not cause any retinal swelling of the injected eyes (C and D). $MnCl_2$ injection caused slight retinal swelling at 4 hours that recovered at 24 hours post-injection. Histologically-revealed retinal thickening paralleled the decreased VA caused by injection volume and Mn^{2+} (A).

Diamond symbols: mean value

Scale bar: 100 μm

2.4 Discussion

This study investigated the toxicity of noninvasive topical Mn^{2+} loading using functional (VA) and structural (MR) measurements followed by histological validation. Our findings show that topical $MnCl_2$ loading caused photoreceptor layers degeneration without detectable damage to the optic nerve within the 7-day timecourse of this investigation. In addition, we also investigated the impact of literature-reported safe dose of intravitreal $MnCl_2$ injection concluding that intravitreal injection causes insignificant visual impairment and is probably safer for MEMRI studies than the newly proposed topical loading.

2.4.1 Topical loading

The route of Mn^{2+} entry is believed to start from the conjunctiva passing through the ciliary body [29, 30]. Afterwards, Mn^{2+} may diffuse into the choroid vasculature passing through the blood-retinal barrier [31] to enter the retinal layers. In addition, Mn^{2+} may also pass through blood-aqueous barrier diffusing into vitreous space reaching the retina ganglion cell layer [32, 29]. In our hands, topical loading only resulted in anterior chamber and retina enhancement while the vitreous space was not enhanced. This is consistent with findings by Sun et al. reporting no intravitreal enhancement [17]. Although a definitive conclusion may not be established from the current study, the observed lack of vitreous enhancement as well as the preferential photoreceptor layer injury after topical loading suggests that Mn^{2+} may enter the ocular space primarily through non-corneal permeation across the conjunctiva and sclera into the anterior uvea.

Visual acuity (VA) reflects the visual function and ocular integrity of retinal efferent pathways to subcortical visual structures [21]. In the present study, VA was employed to assess

the effect of Mn^{2+} loading since VA of normal mice has been measured consistently [20]. Our VA measurements from thirty female C57BL/6 mice were in agreement with Prusky's finding with less than 10% co-variance (0.37 ± 0.03 c/d; mean ± SD; n = 30). The acute 73% decrease in VA after 0.75 M $MnCl_2$ loading followed by a slow recovery and the total loss of vision after 1 M $MnCl_2$ loading without recovery (throughout the course of experiment) suggests that topical loading adversely affects visual function of the loaded eye as a result of Mn^{2+} toxicity since there was no VA change after topical saline loading.

With 1M $MnCl_2$ topical loading, the retina thickened at 1 day followed by significant thinning at 7 days after loading [(~31%, $p < 0.005$); Fig. 2 – 4E and 2 – 4F]. Retinal thickening at 24 hours after 1M $MnCl_2$ loading appears to result from cell swelling [33, 19], while subsequently decreased retinal thickness is likely the result of may be related to retinal degeneration and tissue loss. There was a negligible retinal thickness change by 0.75M topical loading (Fig. 2 – 4F). The increased image intensity of choroid (Fig. 2 – 4D) probably resulted from manganese accumulation in endothelial cells [34].

Photoreceptor layer degeneration was seen in H & E staining (Fig. 2 – 4E), suggesting that the entry of excess calcium analog, Mn^{2+}, could cause metabolic dysfunction and eventual photoreceptor cell loss [14]. At day 1 with 1-M $MnCl_2$ loading, retina thickened variably (Fig. 2 – 4E) due to differential uptake of topically loaded Mn^{2+} between mice. Our T2W images exhibited strong vitreous signal intensities (Fig. 2 – 3A ~ 2 – 3D), potentially confounding layer thickness estimation although retinal swelling and thinning was clearly visible in T2W images. A balanced steady state free precession (bSSFP) MR sequence has been demonstrated to be time-efficient to detect retinal layer and layer-specific responses to hypoxia in retinal and choroidal vasculature, which are separated by an avascular region [35]. This approach could be used to

overcome the shortcoming of T2W measurement employed herein to better assess retinal thickness. The optic nerve integrity was examined using in vivo DTI followed by immunohistochemistry (Fig. 2 – 3B and 2 – 3C). Normal axial ($\lambda_{\parallel}$) and radial ($\lambda_{\perp}$) diffusivities after $MnCl_2$ loading suggest axonal integrity of the loaded optic nerve [26]. Postmortem immunohistochemistry findings supported the conclusions drawn from in vivo DTI measurements. There was no detectable injury in either RGC layer (Fig. 2 – 4E) or optic nerve (Fig. 2 – 3B and 2 – 3C). The visual function impairment is more pronounced with increasing retinal morphological distortions—initially retinal swelling (Fig. 2 – 2, 2 – 4E and 2 – 4F) and subsequently photoreceptor loss and thinning of the retina. Topical saline loading did not cause retinal thickness change, or VA impairment. The results suggest that Mn^{2+} was the primary cause of the decreased VA and reduced retinal thickness.

2.4.2 Intravitreal injection

Intravitreal injection of $MnCl_2$ is a common practice for MEMRI studies. Published reports have examined toxicity of intravitreal injection of $MnCl_2$ in mice and rats [13-15, 36]. Bearer et al. used visual evoke potential (VEP) to assess visual function [13] reporting that 0.5μL of saline injection affected VEP response. They suggested a 0.25μL injection of 200mM $MnCl_2$ (equivalent of 50 nmol) to be the safe dose for MEMRI studies in C57BL/6 mice. Haenold et al. measured VA to determine visual function suggesting that 2μL of 0.0075M $MnCl_2$ (equal to 15 nmol) as the safe dose for the same mouse strain [14]. They found that 50 nmol caused photoreceptor degeneration with RGC injury observed at a dose over 50 nmol.

The volume of the vitreous space in C57BL/6 mice is approximately 5 μL. Chen et al. have previously reported that 0.5 μL of intravitreal saline injection was safe [19]. Haenold et al.

reported normal VA two days after 2 μL of saline injection [14]. The current finding saw transient impairment of VA with 2 μL of saline injection (Fig. 2 – 5A). The recovery of VA 2 days after injecting 2 μL of saline was in agreement with that seen by Haenold et al. A significant retinal swelling was observed with 2 μL saline injection in the present study (Fig. 2 – 5C and 2 – 5D) while 0.25μL saline injection did not impact VA (Fig. 2 – 5A) or retinal thickness (Fig. 2 – 5C and 2 – 5D) at any time point. Our findings support the conclusion of Bearer et al. suggesting the optimum dose for intravitreal injection is 0.25 μL of 200 mM $MnCl_2$. We failed to see enhancement using the dose proposed by Bearer et al., 0.125 μL of 200 mM $MnCl_2$ (data not shown).

In conclusion, we found that both topical loading and intravitreal injection of $MnCl_2$ provided similar T1W enhancement in the visual system for assessing anterograde axonal transport. Despite the non-invasive nature of $MnCl_2$ loading, topical loading significantly impaired VA. The photoreceptor layer was significantly injured with retinal ganglion cells largely unaffected thus no detectable injury in the optic nerve. The working concentration of 0.75 M $MnCl_2$ offers sufficient enhancement for assessing axonal transport. However, the visual function was still affected at this dose thus cautioning functional correlation studies using topical loading. In contrast, the previously reported safe dose for intravitreal injection proposed by Bearer et al. is ideal for axonal transport correlating with functional assessment in mouse visual system.

Acknowledgements

The authors would like to thank Dr. Junjie Chen for the invaluable discussions. This study was supported in part by the grants from National Institute of Health R01-NS047592 (S.-K.S.), and National Multiple Sclerosis Society (NMSS) RG 4549A4/1 (S.-K.S.).

2.5 References

1. Smith, K.D., et al., *In vivo axonal transport rates decrease in a mouse model of Alzheimer's disease.* Neuroimage, 2007. **35**(4): p. 1401-8.

2. Silva, A.C., et al., *Manganese-enhanced magnetic resonance imaging (MEMRI): methodological and practical considerations.* NMR in biomedicine, 2004. **17**(8): p. 532-43.

3. Thuen, M., et al., *Manganese-enhanced MRI of the optic visual pathway and optic nerve injury in adult rats.* J Magn Reson Imaging, 2005. **22**(4): p. 492-500.

4. Boretius, S., et al., *MRI of optic neuritis in a rat model.* Neuroimage, 2008. **41**(2): p. 323-34.

5. Gadjanski, I., et al., *Role of n-type voltage-dependent calcium channels in autoimmune optic neuritis.* Annals of neurology, 2009. **66**(1): p. 81-93.

6. Thuen, M., et al., *Combination of Mn(2+)-enhanced and diffusion tensor MR imaging gives complementary information about injury and regeneration in the adult rat optic nerve.* J Magn Reson Imaging, 2009. **29**(1): p. 39-51.

7. Thuen, M., et al., *Manganese-enhanced MRI of the optic visual pathway and optic nerve injury in adult rats.* Journal of magnetic resonance imaging : JMRI, 2005. **22**(4): p. 492-500.

8. Chan, K.C., et al., *In vivo retinotopic mapping of superior colliculus using manganese-enhanced magnetic resonance imaging.* Neuroimage, 2011. **54**(1): p. 389-95.

9. De La Garza, B.H., et al., *Layer-specific manganese-enhanced MRI of the retina in light and dark adaptation.* Invest Ophthalmol Vis Sci, 2012. **53**(8): p. 4352-8.

10. Berkowitz, B.A., et al., *Noninvasive and simultaneous imaging of layer-specific retinal functional adaptation by manganese-enhanced MRI.* Invest Ophthalmol Vis Sci, 2006. **47**(6): p. 2668-74.

11. Olanow, C.W., *Manganese-induced parkinsonism and Parkinson's disease.* Annals of the New York Academy of Sciences, 2004. **1012**: p. 209-23.

12. Silva, A.C. and N.A. Bock, *Manganese-enhanced MRI: an exceptional tool in translational neuroimaging.* Schizophrenia bulletin, 2008. **34**(4): p. 595-604.

13. Bearer, E.L., et al., *Role of neuronal activity and kinesin on tract tracing by manganese-enhanced MRI (MEMRI).* Neuroimage, 2007. **37 Suppl 1**: p. S37-46.

14. Haenold, R., et al., *Magnetic resonance imaging of the mouse visual pathway for in vivo studies of degeneration and regeneration in the CNS.* NeuroImage, 2012. **59**(1): p. 363-76.

15. Luo, L., et al., *Manganese-enhanced MRI optic nerve tracking: effect of intravitreal manganese dose on retinal toxicity.* NMR in biomedicine, 2012.

16. Lindsey, J.D., et al., *Ocular integrity following manganese labeling of the visual system for MRI.* Magn Reson Imaging, 2013.

17. Sun, S.W., et al., *Noninvasive topical loading for manganese-enhanced MRI of the mouse visual system.* Investigative ophthalmology & visual science, 2011. **52**(6): p. 3914-20.

18. Sun, S.W., T. Thiel, and H.F. Liang, *Impact of repeated topical-loaded manganese-enhanced MRI on the mouse visual system.* Investigative ophthalmology & visual science, 2012. **53**(8): p. 4699-709.

19. Chen, J., et al., *Cell swelling contributes to thickening of low-dose N-methyl-D-aspartate-induced retinal edema.* Invest Ophthalmol Vis Sci, 2012. **53**(6): p. 2777-85.

20. Prusky, G.T., et al., *Rapid quantification of adult and developing mouse spatial vision using a virtual optomotor system.* Invest Ophthalmol Vis Sci, 2004. **45**(12): p. 4611-6.

21. Douglas, R.M., et al., *Independent visual threshold measurements in the two eyes of freely moving rats and mice using a virtual-reality optokinetic system.* Visual neuroscience, 2005. **22**(5): p. 677-84.

22. Garbow, J.R., C. Mcintosh, and M.S. Conradi, *Actively decoupled transmit-receive coil-pair for mouse brain MRI.* Concepts in Magnetic Resonance Part B-Magnetic Resonance Engineering, 2008. **33B**(4): p. 252-259.

23. Spees, W.M., T.H. Lin, and S.K. Song, *White-matter diffusion fMRI of mouse optic nerve.* Neuroimage, 2013. **65**: p. 209-15.

24. Blewitt, E.S., T. Pogmore, and I.C. Talbot, *Double embedding in agar/paraffin wax as an aid to orientation of mucosal biopsies.* Journal of clinical pathology, 1982. **35**(3): p. 365.

25. Chen, J., et al., *In vivo quantification of T1, T2, and apparent diffusion coefficient in the mouse retina at 11.74T.* Magn Reson Med, 2008. **59**(4): p. 731-8.

26. Song, S.K., et al., *Diffusion tensor imaging detects and differentiates axon and myelin degeneration in mouse optic nerve after retinal ischemia.* Neuroimage, 2003. **20**(3): p. 1714-22.

27. Duong, T.Q., et al., *Layer-specific anatomical, physiological and functional MRI of the retina.* NMR in biomedicine, 2008. **21**(9): p. 978-96.

28. Wang, Q., et al., *Photoreceptor degeneration changes magnetic resonance imaging features in a mouse model of retinitis pigmentosa.* Magn Reson Med, 2011. **65**(6): p. 1793-8.

29. Diebold, Y. and M. Calonge, *Applications of nanoparticles in ophthalmology.* Progress in retinal and eye research, 2010. **29**(6): p. 596-609.

30. Molokhia, S.A., et al., *Examination of penetration routes and distribution of ionic permeants during and after transscleral iontophoresis with magnetic resonance imaging.* International journal of pharmaceutics, 2007. **335**(1-2): p. 46-53.

31. Morrison, J.C., et al., *Microvasculature of the rat optic nerve head.* Investigative ophthalmology & visual science, 1999. **40**(8): p. 1702-9.

32. Lindsey, J.D., et al., *Magnetic resonance imaging of the visual system in vivo: transsynaptic illumination of V1 and V2 visual cortex.* NeuroImage, 2007. **34**(4): p. 1619-26.

33. Berkowitz, B.A., et al., *Evidence for diffuse central retinal edema in vivo in diabetic male Sprague Dawley rats.* PloS one, 2012. **7**(1): p. e29619.

34. Nair, G., et al., *Manganese-enhanced MRI reveals multiple cellular and vascular layers in normal and degenerated retinas.* J Magn Reson Imaging, 2011. **34**(6): p. 1422-9.

35. Muir, E.R. and T.Q. Duong, *Layer-specific functional and anatomical MRI of the retina with passband balanced SSFP.* Magn Reson Med, 2011. **66**(5): p. 1416-21.

36. Thuen, M., et al., *Manganese-enhanced MRI of the rat visual pathway: acute neural toxicity, contrast enhancement, axon resolution, axonal transport, and clearance of Mn(2+).* J Magn Reson Imaging, 2008. **28**(4): p. 855-65.

Chapter 3

Axonal transport rate decreased at the onset of optic neuritis in EAE mice

This chapter represents a manuscript initially submitted on August 16th to The Journal of Neuroscience and currently under review.

(Tsen-Hsuan Lin, Joong Hee Kim, Carlos Perez-Torres, Chia-Wen Chiang, Kathryn Trinkaus, Anne H. Cross, and Sheng-Kwei Song)

Abstract

Optic neuritis is frequently the first symptom of multiple sclerosis (MS), an inflammatory demyelinating neurodegenerative disease. Impaired axonal transport has been considered as an early event of neurodegenerative diseases. However, few studies have assessed the integrity of axonal transport in MS or its animal models. In this study, we employed manganese-enhanced MRI (MEMRI) to assess axonal transport in optic nerves in experimental autoimmune encephalomyelitis (EAE) mice, at the onset of optic neuritis. Axonal transport was assessed as (a) optic nerve Mn^{2+} accumulation rate (in % signal change/hour) by measuring the rate of increased total optic nerve signal enhancement, and (b) Mn^{2+} transport rate (in mm/hour) by measuring the rate of change in optic nerve length enhanced by Mn^{2+}. Compared to sham-treated healthy mice, Mn^{2+} accumulation rate was significantly decreased by 19% and 38% for EAE mice with moderate and severe optic neuritis, respectively. The axonal transport rate of Mn^{2+} was significantly decreased by 43% and 65% for EAE mice with moderate and severe optic neuritis, respectively. The degree of axonal transport deficit correlated with the extent of impaired visual

function, as well as the severity of inflammation, demyelination, and axonal injury at the onset of optic neuritis.

3.1 Introduction

Multiple sclerosis (MS) is an inflammatory demyelinating disorder of the central nervous system (CNS) causing significant neurological dysfunction that accumulates over a lifetime[1]. Experimental autoimmune encephalomyelitis (EAE) is a widely used animal model of MS exhibiting many MS-like neurological dysfunctions including optic neuritis (ON) [2, 3], which is often an early symptom of MS [4-7]. Inflammatory demyelination and axonal injury in the optic nerve that are commonly seen in MS patients are also frequently present in EAE-affected mice (EAE mice) [8-10]. Accumulation of amyloid precursor protein (APP) is regarded as an early marker of axonal injury in MS patients and EAE mice [11-16]. Interruption of axonal transport in injured axons results in the accumulation of APP, which can be detected by immunohistochemistry (IHC) [11, 17]. Hence, axonal transport disruption is believed to be an early event in EAE and in some patients with MS.

Magnetic resonance imaging (MRI) has played crucial roles in examining pathologies of the optic nerve in rodent EAE [18-21]. Diffusion tensor imaging (DTI) can specifically reflect pathologies of axon injury and demyelination in optic nerve [8, 22, 23]. Visual function tests to assess optic nerve integrity are readily available in both human and animal models [23-25]. Thus, the optic nerve provides an ideal system to investigate the interrelationship between white-matter pathologies and functional outcomes. Manganese-enhanced MRI (MEMRI) has been applied in the rodent CNS [26-30] to investigate ion homeostasis and axonal transport. Manganese ion (Mn^{2+}), as a calcium analogue, is taken up by neurons through voltage-gated Ca^{2+} channels. In the mouse visual system, Mn^{2+} is taken up by retinal ganglion cells, packaged in vesicles, and transported along microtubules down the axonal tract [31]. Mn^{2+}, a paramagnetic ion, reduces tissue water T1 relaxation time and its presence in tissues can be identified as hyper-intensities in

the T1W image [32]. Therefore, Mn^{2+} can serve as both a contrast agent and an axonal transport tracer.

In this study, $MnCl_2$ was injected in the vitreous of sham and EAE mouse eyes immediately followed by serial 3D-T1W images for 5.5 hours to quantify the axonal transport rate. Our results suggest that axonal transport impairment is present at the onset of optic neuritis in EAE mice, and correlates with impaired visual function and the underlying pathologies.

3.2 Materials and Methods

All experimental procedures involving animals were approved by Washington University's Animal Studies Committee and conformed to the Public Health Service Policy on Humane Care and Use of Laboratory Animals (http://grants.nih.gov/grants/olaw/olaw.htm).

3.2.1 Experimental autoimmune encephalomyelitis (EAE)

Sixteen 7-week old C57BL/6 mice were obtained from Jackson Laboratory (Bar Harbor, ME). Before immunization, mice were housed with 12-hour dark/light cycle for a week. Ten mice were randomly selected to be immunized with 50 µg MOG_{35-55} peptide emulsified (1:1) in incomplete Freund's adjuvant (IFA) and Mycobacterium tuberculosis. Pertussis toxin (300 ng; PTX, List Laboratories, Campbell, CA) was injected intravenously on the day of MOG_{35-55} immunization and two days later. The remaining six sham mice underwent the same immunization procedure with only IFA without MOG_{35-55}. Mice were assessed daily for neurological disabilities using a standard clinical score [33] system: 1 = limp tail; 2 = hind limb

weakness sufficient to impair righting; 3 = one limb paralyzed; 4 = two limbs paralyzed; 5 = 3 or more limbs paralyzed or the animal is moribund (mice were euthanized if they reach grade 5).

3.2.2 Visual acuity (VA)

The VA of mice was measured daily starting before immunization using the Virtual Optometry System (Optomotry, Cerebral Mechanics, Inc., Canada). Briefly, the virtual rotating columns were projected on the LCD monitors with different spatial frequencies in cycles/degree (c/d). The mouse head movement in response to the virtual column rotations was noted. The spatial frequency was increased starting from 0.1 c/d with step size of 0.05 c/d until the mouse stopped responding. The VA was defined as the highest spatial frequency of the virtual rotating columns to which the mouse was able to respond. We have previously reported that VA of normal C57BL/6 mice to be 0.38 ± 0.03 c/d (mean ± S.D., n=30) and defined VA ≤ 0.25 c/d as the onset of acute ON for EAE mice [34]. MEMRI was performed on the day when mice exhibited VA ≤ 0.25 c/d. The mice in sham group did not develop impaired visual function and underwent the same MEMRI procedure at the same time period as EAE group.

3.2.3 Intravitreal $MnCl_2$ injection

$MnCl_2$ was injected in the eye that had a measured VA ≤ 0.25 c/d. Mice were anesthetized using 1.5-2% isoflurane/oxygen. After the appropriate level of anesthesia was achieved, assessed by the lack of response to toe pinch, mice were placed on a custom-made head holder. A 34-gauge needle, connected to a micro-injection pump (WPI Instrument, FL, US), was inserted into the posterior vitreous at 1-1.3 mm posterior to limbus. A dose of 50 nmol $MnCl_2$, given as 0.25 µL of 0.2 M solution [27], was delivered at a rate of 3 µL/min. At the

conclusion of injection, the needle was left in the place for an extra 1 minute before withdrawal and then a drop of antibiotic gel was applied to both injected and un-injected eyes[35].

3.2.4 Manganese-enhanced MRI (MEMRI)

MEMRI was performed immediately after $MnCl_2$ administration on a 4.7 T Agilent DirectDrive small-animal MRI system (Agilent Technologies, Santa Clara, CA) equipped with Magnex/Agilent HD image gradient coil (Magnex, Oxford, UK) with pulse gradient strength up to 58 G/cm and a gradient rise time ≤ 295 μs. Mice were anesthetized by 1.5% isoflurane/oxygen. During experiments, respiratory rate and body temperature were monitored using a MR compatible animal monitoring system (SA Instrument, Inc., Stony Brook, NY, US) and maintained at 130 – 150 breaths/min and 37˚C with a regulated circulating warm water pad underneath mouse body along with regulated warm air blown into the magnet bore, respectively. A pair of 8-cm diameter volume (transmit) and 1.7-cm diameter surface (receive) active-decoupled coils were used.

A standard 3D gradient echo sequence was employed for T1-weighted (T1W) image of the whole mouse brain with the following parameters: repetition time (TR) = 15 ms, echo time (TE) = 2.63 ms, flip angle = 20˚, number of averages = 16, field-of-view (FOV) = 15 × 15 × 22 mm^3, matrix size = 128 × 128 × 64 (zero-filled to 256 × 256 × 128), acquisition time = 32.8 minutes. Ten successive sets of 3D-T1W image were captured approximately from 0.55 – 5.5 hours post-injection.

3.2.5 B1-inhomogeneity correction

A 3D-T1W image of a phantom (uniform 13 × 9 × 25 mm^3 of 2% agar gel placed underneath the active-decoupled surface coil with the distance between gel and coil similar to the

in vivo study) was acquired using the same MEMRI parameters with 64 averages to obtain the profile of surface coil sensitivity (acquisition time was 131.2 minutes). To correct B1 inhomogeneity, the raw 3D-T1W image of the mouse brain was divided by the 3D-T1W image of 2% agar phantom voxel by voxel directly using image calculator in ImageJ [36] and the corrected 3D-T1W image data set was generated for analyzing MEMRI data.

3.2.6 MEMRI data analysis

Surface-coil sensitivity profile corrected T1W image data set of the final time point was displayed using volume viewer plugin version 1.31 in ImageJ (http://rsbweb.nih.gov/ij/plugins/volume-viewer.html, NIH, US) with z-aspect factor of 2 resulting in isotropic 256 × 256 × 256 data matrix. The 3D data matrix was adjusted by rotating about x- and z-axis and distance slider to make oblique image plan bisecting both optic nerves. The oblique image containing both nerves was saved and converted to 8-bit gray scale. The corrected 3D-T1W image data sets of other previous time points were rotated using the same rotation parameters. The final result was a stack of oblique corrected T1W images (ten images) from each mouse (from 0.55 – 5.5 hours post-injection) for accumulation and transport rate calculation.

To derive the rate of total Mn^{2+} accumulation, ROI of optic nerves were drawn on the oblique corrected T1W image at the final time point for each mouse. The average size of the optic nerve ROI was 188 ± 27 voxels (n=160, mean ± S.D.). A 20 × 20-voxel reference area ROI was drawn 30 voxels away from optic nerve head. This reference area ROI was pure muscle, not affected by Mn^{2+}. The ROI information of optic nerves and reference area was saved and then applied to oblique corrected T1W images of other previous time points. Finally, the

normalization was performed by taking the ratio of signal intensity of optic nerve ROIs and their respective reference ROI.

To calculate Mn^{2+} transport rate, a line ROI was drawn along the signal-enhanced and the contralateral optic nerves at the final time point, taking advantage of the increased contrast for the ROI definition. The same line ROIs were applied to the corrected T1W images at all time points. The average size of Mn^{2+}-loaded and reference line ROI was 54 ± 3.3 and 53 ± 3.2 voxels (n = 160, mean ± S.D.) respectively. The arrival of Mn^{2+} at the loaded nerve was defined by counting voxels with the signal intensity ≥ mean + 2 S.D. of the signal intensity of all voxels in the contralateral optic nerve. After determining the number of voxels in the length of Mn^{2+}-enhanced optic nerves was converted to millimeter by combining the known in-plane image resolution, the geometric transformation associated with the oblique slice plane and the Pythagorean equation [37]. Transport rate was defined as the slope of Mn^{2+}-enhanced length over time by linear fitting.

3.2.7 Immunohistochemistry (IHC) of optic nerves

Following MEMRI experiments, mice underwent intra-cardiac perfusion with 1% phosphate buffered saline (PBS) followed by 4% paraformaldehyde in 0.01 M PBS. Brains were excised and post-fixed in the same fixative for 24 hours then transferred to 0.01 M PBS for storage at 4 ˚C until histological analysis was performed. Mouse optic nerves were dissected from each brain and embedded in 2% agar blocks [38]. Then, the agar blocks were embedded in paraffin wax and 5-μm thick transverse slices were sectioned for IHC staining. Sectioned slices were deparaffinized, and rehydrated to facilitate binding of antibodies and then blocked using solution mixed with 1% bovine serum albumin (BSA, Sigma-Aldrich, MO, USA) and 5%

normal goat-serum solution (Invitrogen, CA, USA) for 20 minutes at room temperature to prevent non-specific binding and to increased antibody permeability. Slides were incubated with monoclonal anti-phosphorylated neurofilament antibody (SMI-31; 1:1000, Covance, NJ, USA) to stain non-injured axons, or with rabbit anti-myelin basic protein antibody (MBP, 1:1000, Sigma-Aldrich, MO, USA) to stain myelin sheath [8, 39, 40] at 4˚C overnight. After rinsing, goat anti-mouse IgG or goat anti-rabbit IgG conjugated Alexa 488 (1:800, Invitrogen, CA, USA) were applied to visualize immunoreactivity of phosphorylated neurofilaments and MBP. Finally, slides were covered using Vectashield Mounting Medium with 4',6-diamidino-2-phenylindole (DAPI) (Vector Laboratory, CA, USA) to stain nuclei [40, 41]. Histological slides were examined with Nikon Eclipse 80i fluorescence microscope equipped with a 60× water objective, and images were captured with a black-and-white CCD camera using MetaMorph software (Universal Imaging Corporation, Sunnyvale, CA, USA) at the center of optic nerve.

3.2.8 Histological data analysis

The whole field of SMI-31, MBP, and DAPI staining images at 60× magnification were captured with the same fluorescence light intensity and exposure time. All captured images were converted to 8- bit gray scale and analyzed using threshold, analyze particles and gray level watershed segmentation functions in ImageJ (http://bigwww.epfl.ch/sage/soft/watershed/).

3.2.9 Statistical analysis

Linear repeated measures models were used to test normalized Mn^{2+}-enhancement signal intensities at each time point (from 0.55 – 5.5 hours post-injection with 0.55-hour step size) for pairwise comparison among shame and EAE mice with moderate and severe ON: sham vs. moderate, sham vs. severe, and moderate vs. severe groups.

Multiple comparisons for accumulation rate, transport rate, SMI-31, MBP, and DAPI by each study group (sham/moderate/severe) were performed using a linear regression model of each outcome. P-values for the three pairwise tests (sham vs. moderate, sham vs. severe, and moderate vs. severe) were adjusted using Tukey's HSD (honest significant difference). VA, SMI-31, MBP and DAPI were measured once per mouse and their association with the rate of change in accumulation or transport was analyzed using Spearman rank correlation coefficients.

3.3 Results

3.3.1 Visual acuity

After immunization, daily visual acuity (VA) of sham and EAE mice was measured. When mice exhibited VA ≤ 0.25 c/d [34], MEMRI was performed (12 ± 2.1 days post-immunization, mean ± S.D., n=10). In this study, CS appeared at the same day as the first sign of impaired VA. VA at ON onset was different among mice examined and was used to separate mice into three groups: sham (VA = 0.35 or 0.4 c/d; CS = 0), moderate ON (VA = 0.2, CS = 1 for one mouse; VA = 0.25 c/d, CS = 0 for the other four mice), and severe ON (VA = 0 c/d, CS =0 for two mice and CS = 2.5 for the other three mice in this group; Fig. 1 A).

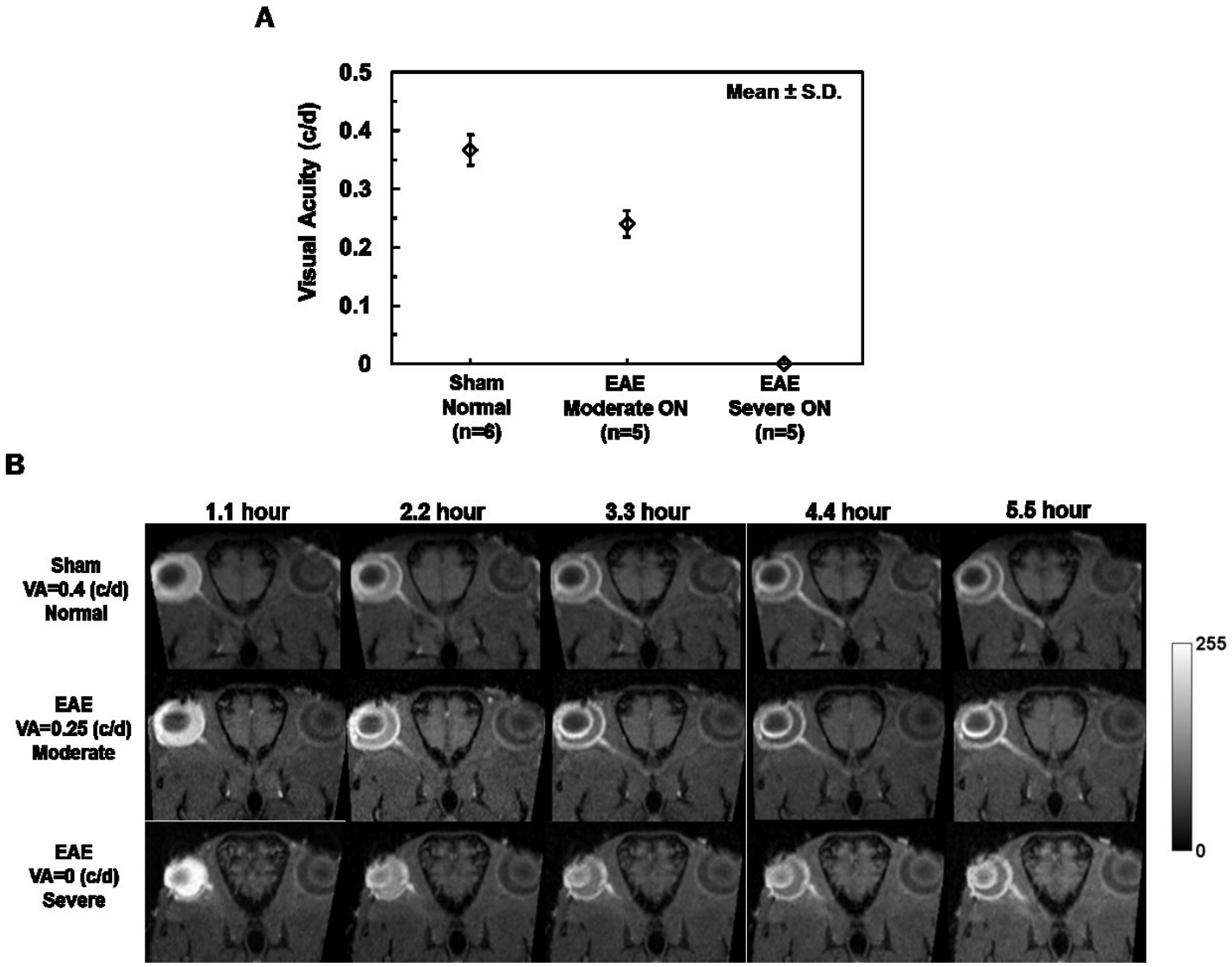

Figure 3 – 1 Group averaged visual acuity (VA) of sham (n=6) and EAE (n=10) eyes before MEMRI experiments. EAE mice were separated based on VA to moderate (VA = 0.25/0.20 c/d) and severe (VA = 0 c/d) ON groups (A). A serial time-lapse oblique corrected T1W images from representative mice are presented to demonstrate the different degree of Mn^{2+}-enhancement of optic nerves from sham and EAE mice from 1.1 – 5.5 hours post-injection (B). Mn^{2+}-enhancement of optic nerves clearly increases with time. At the end time point, mice with the lower VA exhibited less Mn^{2+}-enhancement reflecting slower axonal transport.

3.3.2 The optic nerve Mn^{2+} accumulation rate

Since the image intensity was used to detect Mn^{2+} arrival, the B1-inhomogeneity correction of the surface coil was performed (Lin et al., 2003, Hou, 2006) using the 3D T1W image of 2% agar gel. After correction, the averaged intensity of randomly selected line profiles on the corrected T1W images was comparable in both vertical and horizontal directions suggesting a reasonable B1-field inhomogeneity correction (data not shown).

A series of time-lapse representative B1-profile corrected oblique T1W images of sham, moderate and severe ON mice exhibited different degrees of Mn^{2+}-enhancement suggesting different axonal transport rates in optic nerves. The hyper-intensity of optic nerve resulting from axonal transport of Mn^{2+} was readily visible (Fig. 1 B). The optic-nerve and reference ROI were defined (Fig. 2 A). The time course of group averaged signal intensity ratios of optic-nerve to reference ROI exhibited different rate of signal enhancement among the sham and EAE mice with moderate and severe ON (Fig. 2 B). The accumulation rate of Mn^{2+} in the optic nerve was defined as the slope of the linear fit of the data over time. The group averaged optic nerve Mn^{2+} accumulation rate (the slopes) of sham, moderate ON, and severe ON mice was 0.16, 0.13, and 0.10 a.u./hour, respectively (Table 1; Fig. 2C). The accumulation rate in EAE mice was significantly slower than that of the sham by 19% (moderate ON, $p < 0.005$), and 38% (severe ON, $p < 0.005$). The accumulation rate was 23% ($p < 0.05$) slower in the EAE mice with severe ON than that with the moderate ON. The accumulation rate correlated with VA ($r = 0.87$, $p < 0.0001$).

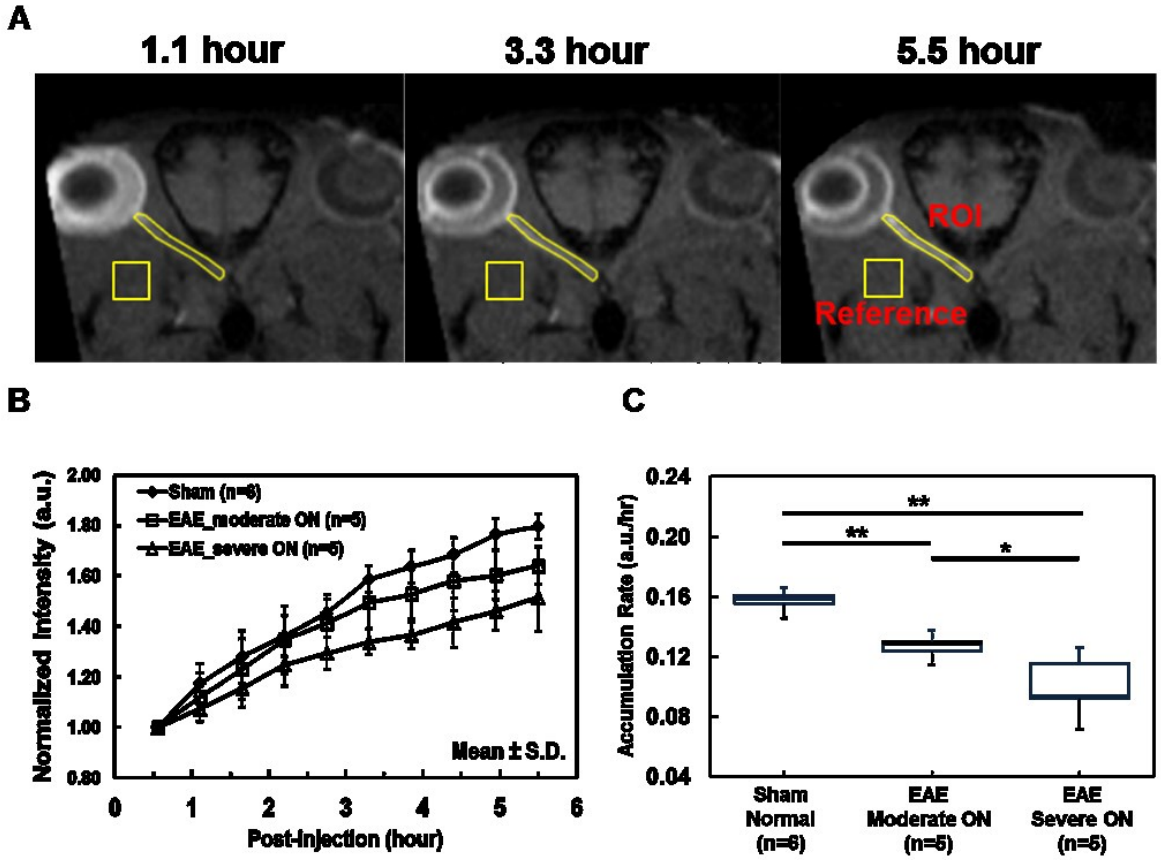

Figure 3 – 2 The ROI of optic nerve and reference area of muscle, where Mn^{2+} does not reach, were defined on the corrected T1W oblique image at each time point (A). The group average of the normalized optic nerve signal intensity from sham, moderate ON and severe ON mice was obtained for each time point from 0.55 – 5.5 hours after injection at a 0.55 hours resolution. The higher rate of Mn^{2+} accumulation over time was associated with the better VA (B). The group averaged slope of the normalized signal intensity over time was defined as the optic nerve accumulation rate of total Mn^{2+}. The box plots reveal that Mn^{2+}accumulation rate of severe ON optic nerves was slower than that of the moderate ON nerves, which was slower than that of the same nerves (B and C).

* indicates $p < 0.05$

** indicates $p < 0.005$

3.3.3 Transport rate of Mn^{2+}

The Mn^{2+}-loaded and contralateral optic nerve reference line ROIs were defined (Fig. 3 A). The enhanced T1W intensity of the optic nerve after Mn^{2+} loading was readily discernible after the subtraction of mean line ROI intensity of the reference optic nerve (Fig. 3 B – D). Representative difference images of sham and EAE mice with moderate ON exhibited different length of the Mn^{2+}-enhanced optic nerve. The entire optic nerve was enhanced at 3.3 and 5.5 hours post-injection for sham (Fig. 3 B) and EAE mice with moderate ON (Fig. 3 C), respectively. In EAE mice with severe ON, only partially enhanced optic nerve was seen (Fig. 3 D). The time course suggested that the group-averaged time to enhance the entire optic nerve took 3.3 and 4.95 hours for sham and EAE mice with moderate ON, respectively (Fig. 3 E). The slope of each group represents the transport rate (% of optic nerve/hour). The group averaged Mn^{2+} transport rate of sham, moderate ON, and severe ON mice was 26, 14, and 8 % of optic nerve/hour (Fig. 3 E). The Mn^{2+} transport rate converted to mm/hour was: 0.92, 0.52, and 0.32 mm/hour for the sham, moderate ON, and severe ON mice, respectively (Table 1). The transport rate of EAE mice was decreased compared with sham mice by 43% ($p < 0.05$) and 65% ($p < 0.005$) respectively for moderate and severe ON groups. EAE mice with moderate ON exhibited a non-significant trend of faster transport rate than severe ON mice ($p = 0.15$). The transport rate correlated well with the VA ($r = 0.85$, $p < 0.0001$).

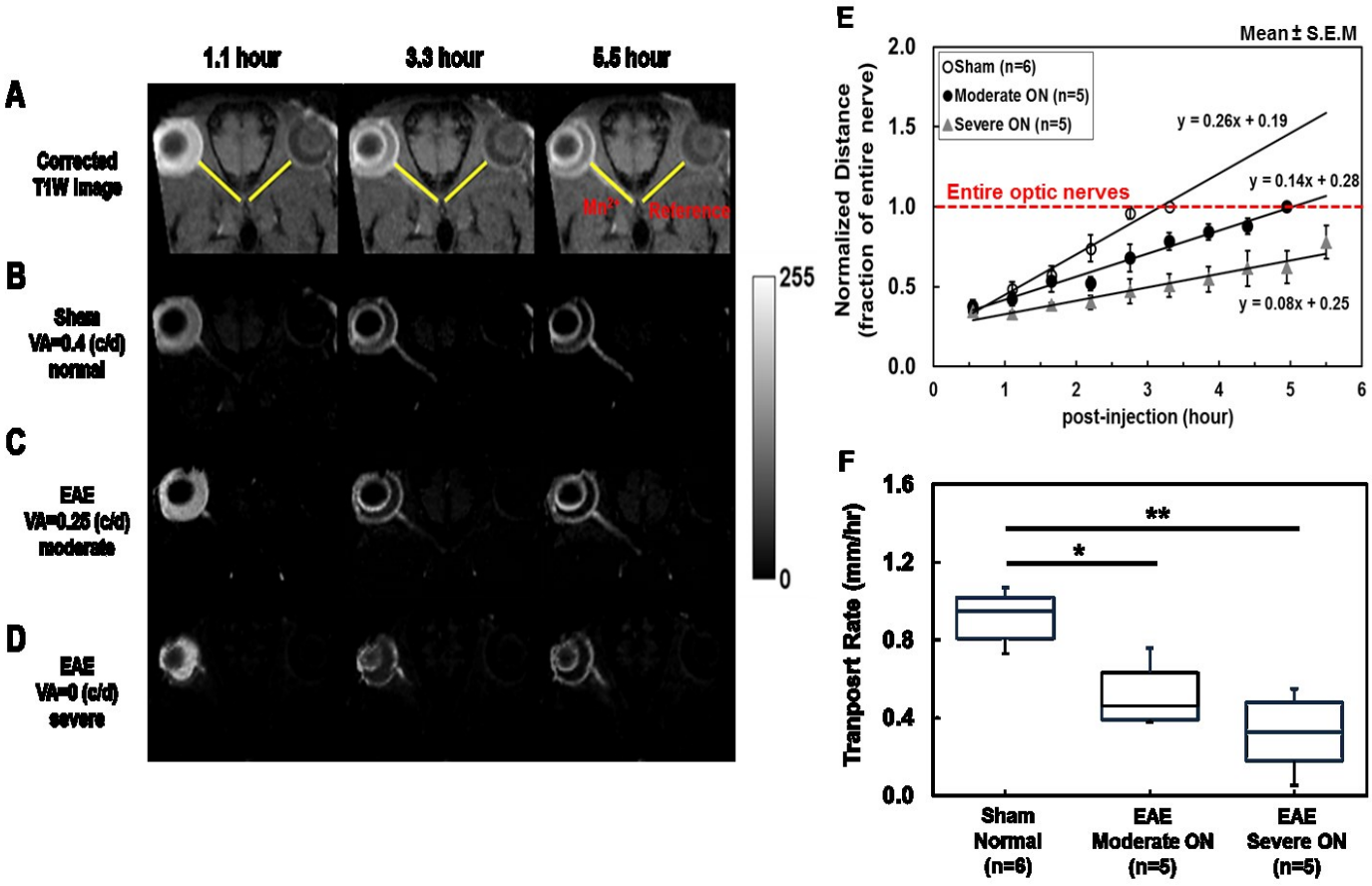

Figure 3 – 3 To estimate Mn^{2+} transport rate in mm/hour, line-ROIs were defined to match the optic nerve length (A). The arrival of Mn^{2+} in optic nerves was defined by the T1W enhancement of the optic nerves referencing to the line-ROI of the non-loaded eye. To visualize the extent of Mn^{2+}-enhancement, representative oblique-corrected T1W images from each group were displayed after subtracting the mean intensity of the reference line-ROI (B, C, and D). Three representative subtracted images of sham, moderate ON and severe ON mice (VA = 0.4, 0.25, and 0, respectively) show different degree of Mn^{2+} transport at 1.1, 3.3, and 5.5 hours post-injection (B, C, and D). For quantification of the transport rate, the arrival of Mn^{2+} was determined using non-subtracted images at each time point by identifying line-ROI voxels of the loaded eye with intensity higher than two standard deviation of the mean from the reference line-ROI of the non-loaded eye. The group averaged displacements, normalized to the total number of voxels of each nerve (red line, panel E), of Mn^{2+} over time revealed different rate of Mn^{2+} transport among the three groups of mice examined (E). Box plot shows transport rate distribution of each group in mm/hour by converting normalized voxel displacement to mm (F). The results demonstrated that Mn^{2+} transport rate of sham optic nerves were significantly faster than moderated ON ($p < 0.005$) and severe ON ($p < 0.005$) suggesting the presence of axonal transport impairment at the onset of ON in EAE mice.

* indicates $p < 0.05$

** indicates $p < 0.005$

Table 3 – 1
Group averaged accumulation and transport rates of sham (n=6), moderate ON (n=5) and severe ON (n=5)

	Sham (n=6)	**Moderate ON (n=5)**	**Moderate ON (n=5)**
Accumulation Rate	0.16 ± 0.01	0.13 ± 0.01	0.10 ± 0.02
Transport Rate	0.92 ± 0.14	0.52 ± 0.17	0.32 ± 0.21

Accumulation Rate (a.u./hour): mean ± S.D.
Transport Rate (mm/hour): mean ± S.D.

3.3.4 Immunohistochemistry (IHC) of optic nerve

Post-image SMI-31, MBP, and DAPI staining of optic nerves from sham and EAE mice with moderate and severe ON was used to assess the integrity of axons and myelin sheaths, and the extent of cellularity (Fig. 4A). Diminished SMI-31 positive axon density suggested axonal injury in EAE mice with moderate and severe ON. Myelin damage of EAE optic nerves was also evident by the decreased density of MBP positive axons. Increased number of DAPI positive nuclei in EAE optic nerves was observed, consistent with cellular inflammation (Fig. 4 A). The SMI-31 positive axon counting showed a significantly diminished intact axon density in optic nerves from EAE mice with moderate ($5.6 \pm 0.5 \times 10^5$, $p < 0.005$, Fig. 4 B) and severe ($4.5 \pm 0.9 \times 10^5$, $p < 0.005$, Fig. 4 B) ON. The significant loss of MBP positive axons expressed as area fraction in optic nerves with moderate (41.6 ± 2.0 %, $p < 0.05$, Fig. 4 B) and severe (34.0 ± 3.4 %, $p < 0.005$, Fig. 4 B) ON was also observed compared with the sham group (48.3 ± 3.9 %). DAPI positive cell nuclear staining was significantly increased in optic nerves from mice with severe ON ($9.1 \pm 3.3 \times 10^3$) when compared with the sham ($3.9 \pm 0.6 \times 10^3$, $p < 0.005$, Fig. 4B) and moderate ON ($5.4 \pm 1.0 \times 10^3$, $p < 0.05$, Fig. 4B) mice. However, the difference between sham ($3.9 \pm 0.6 \times 10^3$) and mice with moderate ON ($5.4 \pm 1.0 \times 10^3$, $p = 0.1$, B) was not significant. Visual function (measured by VA) highly correlated with SMI-31 ($r = 0.84$, $p < 0.0001$), MBP ($r = 0.88$, $p < 0.0001$), and DAPI ($r = -0.81$, $p = 0.0002$). The Mn^{2+} accumulation and transport rate correlated well with the extent of axonal injury ($r = 0.85$ and $r = 0.86$, respectively, $p < 0.0001$) assessed by the density of SMI-31 positive axons, myelin injury ($r = 0.91$ and $r = 0.82$, respectively, $p < 0.0001$) assessed by the MBP positive axons, and inflammation ($r = -0.83$ and $r = -0.84$, respectively) assessed by the density of DAPI-positive

nuclear staining (Fig. 5A – F). Moreover, total amount of Mn^{2+} accumulation rate correlated well with Mn^{2+} transport rate ($r = 0.78$, $p = 0.0003$, Fig. 5G).

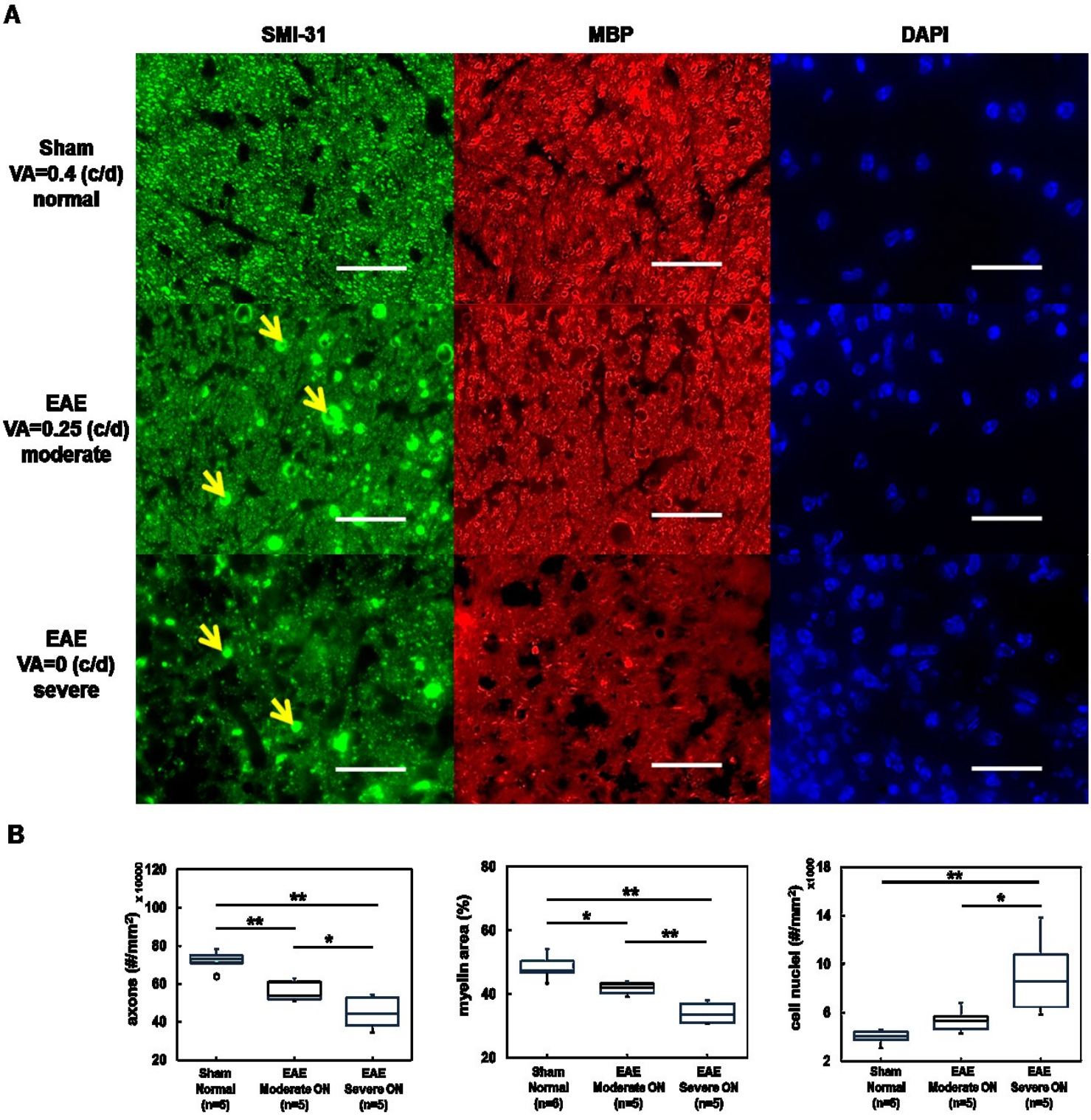
A
SMI-31
MBP
DAPI
Sham
VA=0.4 (c/d)
normal
EAE
VA=0.25 (c/d)
moderate
EAE
VA=0 (c/d)
severe
B
axons (#/mm²) x10000
120
100
80
60
40
20
**
**
*
Sham Normal (n=6)
EAE Moderate ON (n=5)
EAE Severe ON (n=5)
myelin area (%)
80
60
40
20
**
*
**
Sham Normal (n=6)
EAE Moderate ON (n=5)
EAE Severe ON (n=5)
cell nuclei (#/mm²) x1000
18
14
10
6
2
**
*
Sham Normal (n=6)
EAE Moderate ON (n=5)
EAE Severe ON (n=5)

Figure 3 – 4 Representative immunohistochemical staining of optic nerves from sham, moderate ON and severe ON mice (A). Images displayed are 56% field-of-view from the 60× magnification of phosphorylated neurofilament (SMI-31, green), myelin basic protein (MBP, red), and 4', 6-dianidino-2-phenylindole (DAPI, blue). Reduced density of SMI-31 positive axons was seen in optic nerve from moderate and severe ON mice. Increased number of SMI-31 positive areas, may reflect axonal beading or debris (A, yellow arrows), were observed with increased severity of VA. Decreased density of MBP positive axons was also seen with increased VA impairment. The increased DAPI positive nuclear staining was seen with increased VA impairment. Box plots demonstrate the difference in axonal pathologies among the three groups examined (B).

Scale Bar: 25 μm

*$p < 0.05$

**$p < 0.005$

Table 3 – 2
Quantitative immunohistochemistry results of sham (n=6), moderate ON (n=5) and severe ON (n=5)

	SMI-31 (#/mm^2)	**MBP (Area %)**	**DAPI (#/mm^2)**
Sham (n=6)	7.2 (± 0.5) × 10^5	48.3 ± 3.7	3.9 (± 0.6) × 10^3
Moderate ON (n=5)	5.6 (± 0.5) × 10^5	41.7 ± 2.0	5.4 (± 1.0) × 10^3
Severe ON (n=5)	4.5 (± 0.9) × 10^5	34.0 ± 3.4	9.1 (± 0.3) × 10^3

Area % of MBP: comparing to entire 60× image (0.017 mm^2)
Counts: mean ± S.D.

t

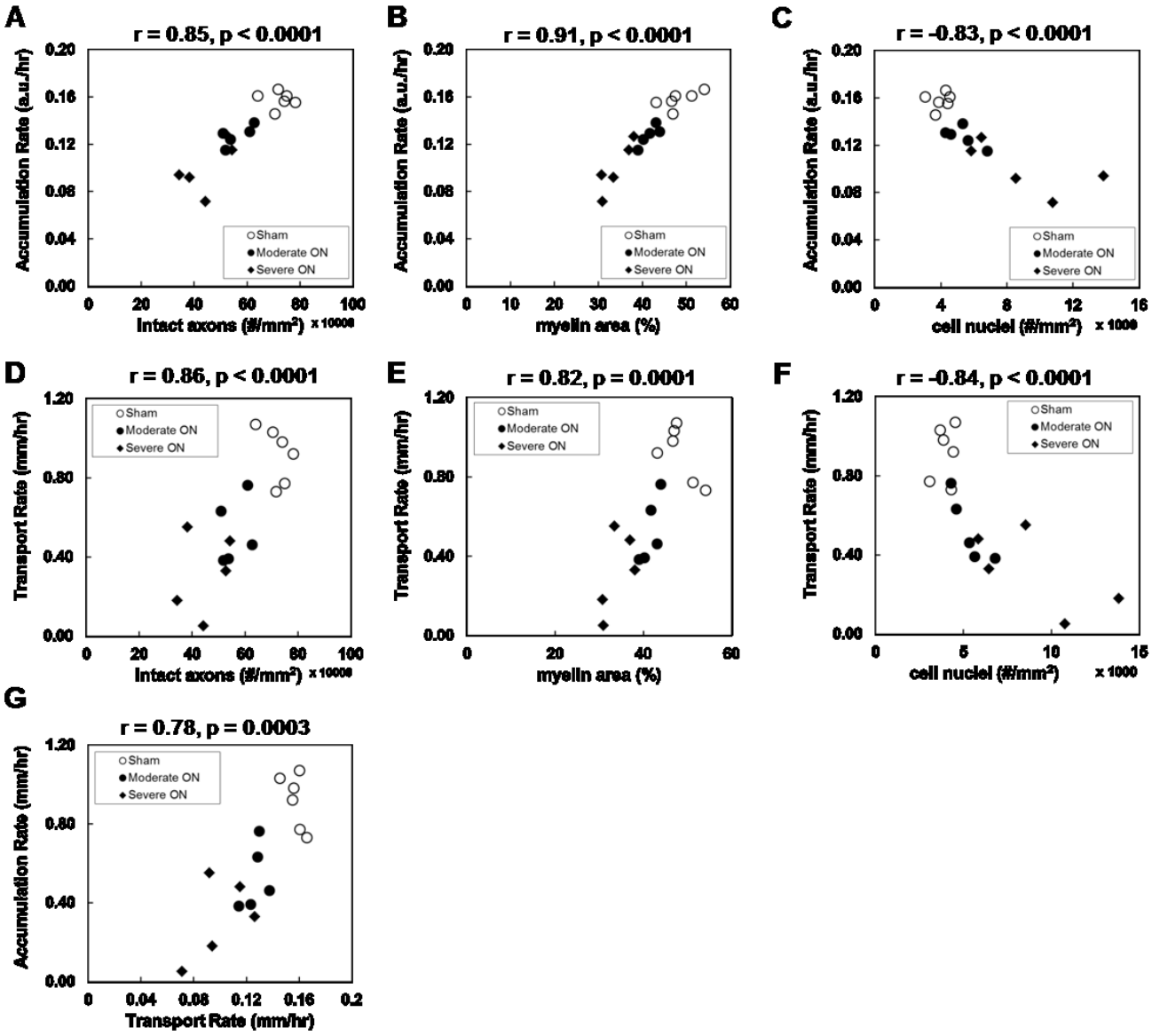

Figure 3 – 5 The scatter plots of axonal transport, assessed in accumulation rate (A – C) or transport rate (D – F). Results suggested that impaired axonal transport correlated with the severity of axonal injury, demyelination, and inflammation respectively. Accumulation rate correlated with transport rate suggesting both reflecting axonal transport in optic nerve of EAE (G).

3.4 Discussion

In this study, we measured the visual function by optokinetic response (to reflect VA; Fig. 1A) and correlated it with axonal transport of optic nerves quantitated using MEMRI at optic neuritis onset during mouse EAE (Fig. 1B). The rate of Mn^{2+} transport in EAE-affected optic nerves was significantly impaired (Fig. 1 – 3) indicating defective fast axonal transport at the onset of ON [42]. Immunohistochemistry of these tissues also indicated the presence of demyelination, inflammation, and axonal injury in optic nerves with ON (Fig. 4B). Each of these axonal pathologies correlated well with decreased axonal transport rate.

The rate of axonal Mn^{2+} accumulation has been reported to reflect axonal transport in mice [43-46]. In the literature, a linear fit of the MEMRI data over a short time course (< 1 hour) was commonly employed. In this study, a 5.5-hour time course was pursued. A linear repeated measures model accounting for the correlation between observations over time applied to the serial 10 measurements suggested that a linear fit was reasonable (data not shown). Thus, a more complex modeling [26, 47] was not pursued in this study to analyze the MEMRI time course data. In addition to this widely employed Mn^{2+} accumulation rate, the current study also assessed axonal transport rate in optic nerves at the onset of ON caused by EAE. The reported fast axonal transport rate ranges between 3 – 16 mm/hour [42, 48]. The Mn^{2+} transport rate by MEMRI has been reported ranging between 0.64 – 5 mm/hour, estimated by a two-point time-lapse measurement [27, 28, 49-53]. In the present study, the Mn^{2+} transport rate in sham optic nerves was 0.92 ± 0.14 mm/hour, at the lower end of published values. Animals in the current study were under isoflurane anesthesia throughout the course of the measurements. The lower axonal transport rate estimated herein may result from the long period of anesthesia [54, 55]. The transport rate estimated using data from the initial 0.55 hours was 1.33, 1.49, and 1.31 mm/hour

in sham, moderate and severe ON groups, respectively. The higher initial rate supported the possible effect of prolonged anesthesia on the measured transport rate. The varied rate of transport using the initial time-lapse data immediately after injection may reflect the variable severity of ON among mice, or the variable response of individual mice to the induction of anesthesia, masking the transport rate difference among groups. The linear increase over time of MEMRI length of the optic nerve between 0.55 – 5.5 hours from all groups suggested that a steady-state of anesthesia was reached 0.55 hours after the injection of Mn^{2+}.

The axonal Mn^{2+} transport rate between moderate and severe ON groups was not statistically different (Fig. 3F). This may be due to the variation in axonal pathologies of the severe ON group, leading to a high standard deviation in that group. It may also be due to imprecision of the method of VA measurement [56]. Optic nerves from three EAE mice with severe ON were not fully enhanced at the end of 5.5 hours post-injection (Fig. 3 E) while the remaining two exhibited whole optic nerve enhancement at 4.4 and 4.95 hours. These two mice also exhibited axonal injury (25% decrease in SMI-31 staining compared with the control) comparable to that in the moderate ON mice (22 ± 7%). IHC results indicated that the mice with higher transport rates suffered less axon and myelin damage than those with slower transport rates. It is possible that acute vasogenic edema at the ON onset impeded action potential propagation and thus reduced VA without significant axonal pathologies [18, 57].

Why might axonal transport be affected in early inflammatory demyelination? Axonal transport depends on energy supplied by mitochondria [58]. In MS and its animal model EAE, several pathologies conspire to reduce energy supply. Nitric oxide and the free radical/reactive oxygen species are increased, including within axons, and inhibit mitochondrial function [59] reducing energy production. Sodium channel redistribution in demyelinated axons reduces

internode length, thereby increasing the energy consumption needed for signal propagation [33, 60, 61]. The potential energy deficit would eventually lead to failure of the Na^+/K^+-ATPase pump (which requires energy for maintenance) and increased intracellular Na^+, thus triggering the reversal of Na^+/Ca^{2+} exchanger. The resultant influx and accumulation of intracellular Ca^{2+} may then lead to further mitochondrial dysfunction and axonal damage [62-66]. Excessive glutamate production by inflammatory cells, coupled with reduced buffering capacity of glial cells leads to glutamate-induced excitotoxicity of axons (which express glutamate receptors) in EAE [63, 66-69], and results in inhibition of mitochondrial mobility and function [70, 71]. Therefore, a vicious cycle of disruption of ion homeostasis, energy deficits, and axonal transport deficits could play a crucial role in axonal degeneration [42, 48, 64, 72].

Since APP is a post-mortem biomarker as early axonal transport disruption and indicates axonal injury, we speculate axonal transport disruption is an early event of axonal pathologies. Although the current data are not sufficient to determine whether the impaired axonal transport is the result or the cause of axonal injury at the onset of ON, its association with various axonal pathologies has been reported. Excess nitric oxide and reactive oxygen species are produced during neuroinflammation. These species have been shown to decrease axonal transport *in vitro* [73, 74]. In other studies, excessive nitric oxide was shown to reversibly block impulse conduction in demyelinated CNS axons of rodents [75] while reduction in nitric oxide at the inflammation site prevented further axonal degeneration [76]. Demyelination was also reported to result in axonal transport disruption in EAE mice [77, 78]. Phosphorylated neurofilaments play a role in regulating axonal transport [79, 80]. Our current findings that decreased axonal transport correlated with reduced SMI-31 (marker of phosphorylated neurofilaments) and MBP

(marker of myelination), and increased DAPI staining (marker of cell nuclei that is increased during inflammation) are consistent with these literature reports.

In summary, this study revealed the presence of impaired optic nerve *in vivo* axonal transport in the early stages of ON in EAE mice. The degree of decrease of the axonal transport rate correlated with severity of impaired visual function, and axonal pathologies including axonal injury, demyelination, and inflammation. Preventing and improving the early axonal transport deficit may be a potential treatment target to halt the degeneration of axons in MS. We have demonstrated the feasibility of quantitatively assessing axonal transport in EAE mice, suitable for a future pre-clinical drug development targeting axonal transport. Measuring axonal transport using MEMRI would not be a viable option in humans due to the potential toxicity of Mn^{2+}. However, preventing axonal degeneration by targeting axonal transport may be assessed by using axonal integrity as the outcome measure monitored using techniques such as diffusion MRI.

3.5 Reference

1. Compston, A. and A. Coles, *Multiple sclerosis.* Lancet, 2008. **372**(9648): p. 1502-17.

2. Bettelli, E., et al., *Myelin oligodendrocyte glycoprotein-specific T cell receptor transgenic mice develop spontaneous autoimmune optic neuritis.* J Exp Med, 2003. **197**(9): p. 1073-81.

3. Shao, H., et al., *Myelin/oligodendrocyte glycoprotein-specific T-cells induce severe optic neuritis in the C57BL/6 mouse.* Invest Ophthalmol Vis Sci, 2004. **45**(11): p. 4060-5.

4. Beck, R.W., et al., *The effect of corticosteroids for acute optic neuritis on the subsequent development of multiple sclerosis. The Optic Neuritis Study Group.* N Engl J Med, 1993. **329**(24): p. 1764-9.

5. Beck, R.W., et al., *High- and low-risk profiles for the development of multiple sclerosis within 10 years after optic neuritis: experience of the optic neuritis treatment trial.* Arch Ophthalmol, 2003. **121**(7): p. 944-9.

6. Pascual, A.M., et al., *Revision of the risk of secondary leukaemia after mitoxantrone in multiple sclerosis populations is required.* Mult Scler, 2009. **15**(11): p. 1303-10.

7. Shams, P.N. and G.T. Plant, *Optic neuritis: a review.* Int MS J, 2009. **16**(3): p. 82-9.

8. Sun, S.W., et al., *Selective vulnerability of cerebral white matter in a murine model of multiple sclerosis detected using diffusion tensor imaging.* Neurobiol Dis, 2007. **28**(1): p. 30-8.

9. Diem, R., et al., *Autoimmune optic neuritis in the common marmoset monkey: comparison of visual evoked potentials with MRI and histopathology.* Invest Ophthalmol Vis Sci, 2008. **49**(8): p. 3707-14.

10. Gold, R., C. Linington, and H. Lassmann, *Understanding pathogenesis and therapy of multiple sclerosis via animal models: 70 years of merits and culprits in experimental autoimmune encephalomyelitis research.* Brain, 2006. **129**(Pt 8): p. 1953-71.

11. Ferguson, B., et al., *Axonal damage in acute multiple sclerosis lesions.* Brain, 1997. **120 (Pt 3)**: p. 393-9.

12. Bitsch, A., et al., *Acute axonal injury in multiple sclerosis. Correlation with demyelination and inflammation.* Brain, 2000. **123 (Pt 6)**: p. 1174-83.

13. Linker, R.A., et al., *Functional role of brain-derived neurotrophic factor in neuroprotective autoimmunity: therapeutic implications in a model of multiple sclerosis.* Brain, 2010. **133**(Pt 8): p. 2248-63.

14. Fairless, R., et al., *Preclinical retinal neurodegeneration in a model of multiple sclerosis.* J Neurosci, 2012. **32**(16): p. 5585-97.

15. Petratos, S., et al., *Limiting multiple sclerosis related axonopathy by blocking Nogo receptor and CRMP-2 phosphorylation.* Brain, 2012. **135**(Pt 6): p. 1794-818.

16. MacKenzie-Graham, A.J., et al., *Estrogen treatment prevents gray matter atrophy in experimental autoimmune encephalomyelitis.* J Neurosci Res, 2012. **90**(7): p. 1310-23.

17. Smith, D.H., et al., *Amyloid beta accumulation in axons after traumatic brain injury in humans.* J Neurosurg, 2003. **98**(5): p. 1072-7.

18. Guy, J., *MRI in experimental inflammatory and mitochondrial optic neuropathies.* NMR Biomed, 2008. **21**(9): p. 968-77.

19. Boretius, S., et al., *MRI of optic neuritis in a rat model.* NeuroImage, 2008. **41**(2): p. 323-34.

20. Xu, J., et al., *Assessing optic nerve pathology with diffusion MRI: from mouse to human.* NMR Biomed, 2008. **21**(9): p. 928-40.

21. Gadjanski, I., et al., *Role of n-type voltage-dependent calcium channels in autoimmune optic neuritis.* Ann Neurol, 2009. **66**(1): p. 81-93.

22. Smith, S.A., et al., *Diffusion tensor imaging of the optic nerve in multiple sclerosis: association with retinal damage and visual disability.* AJNR Am J Neuroradiol, 2011. **32**(9): p. 1662-8.

23. Naismith, R.T., et al., *Diffusion tensor imaging in acute optic neuropathies: predictor of clinical outcomes.* Arch Neurol, 2012. **69**(1): p. 65-71.

24. Diem, R., et al., *Combined therapy with methylprednisolone and erythropoietin in a model of multiple sclerosis.* Brain, 2005. **128**(Pt 2): p. 375-85.

25. Matsunaga, Y., et al., *Visual functional and histopathological correlation in experimental autoimmune optic neuritis.* Invest Ophthalmol Vis Sci, 2012. **53**(11): p. 6964-71.

26. Olsen, O., et al., *Manganese transport in the rat optic nerve evaluated with spatial- and time-resolved magnetic resonance imaging.* J Magn Reson Imaging, 2010. **32**(3): p. 551-60.

27. Bearer, E.L., et al., *Role of neuronal activity and kinesin on tract tracing by manganese-enhanced MRI (MEMRI).* Neuroimage, 2007. **37 Suppl 1**: p. S37-46.

28. Pautler, R.G., A.C. Silva, and A.P. Koretsky, *In vivo neuronal tract tracing using manganese-enhanced magnetic resonance imaging.* Magn Reson Med, 1998. **40**(5): p. 740-8.

29. Thuen, M., et al., *Manganese-enhanced MRI of the rat visual pathway: acute neural toxicity, contrast enhancement, axon resolution, axonal transport, and clearance of Mn(2+).* J Magn Reson Imaging, 2008. **28**(4): p. 855-65.

30. Chan, K.C., et al., *In vivo retinotopic mapping of superior colliculus using manganese-enhanced magnetic resonance imaging.* NeuroImage, 2011. **54**(1): p. 389-95.

31. Pautler, R.G. and A.P. Koretsky, *Tracing odor-induced activation in the olfactory bulbs of mice using manganese-enhanced magnetic resonance imaging.* Neuroimage, 2002. **16**(2): p. 441-8.

32. Silva, A.C., et al., *Manganese-enhanced magnetic resonance imaging (MEMRI): methodological and practical considerations.* NMR Biomed, 2004. **17**(8): p. 532-43.

33. Dutta, R., et al., *Mitochondrial dysfunction as a cause of axonal degeneration in multiple sclerosis patients.* Ann Neurol, 2006. **59**(3): p. 478-89.

34. Chiang, C.W., et al., *Acute visual function impairment in EAE is primarily caused by optic nerve inflammation as assessed by DBSI.* Proc. Intl. Soc. Mag. Reson. Med. 20, 3085, 2012.

35. Chen, J., et al., *Cell Swelling Contributes to Thickening of Low-Dose N-methyl-D-Aspartate-Induced Retinal Edema.* Invest Ophthalmol Vis Sci, 2012. **53**(6): p. 2777-85.

36. Schneider, C.A., W.S. Rasband, and K.W. Eliceiri, *NIH Image to ImageJ: 25 years of image analysis.* Nat Methods, 2012. **9**(7): p. 671-5.

37. Sally, J.D. and P.J. Sally, *Roots to research : a vertical development of mathematical problems*2007, Providence, R.I.: American Mathematical Society. xiii, p. 63.

38. Blewitt, E.S., T. Pogmore, and I.C. Talbot, *Double embedding in agar/paraffin wax as an aid to orientation of mucosal biopsies.* J Clin Pathol, 1982. **35**(3): p. 365.

39. Song, S.K., et al., *Diffusion tensor imaging detects and differentiates axon and myelin degeneration in mouse optic nerve after retinal ischemia.* NeuroImage, 2003. **20**(3): p. 1714-22.

40. Budde, M.D., et al., *Axial diffusivity is the primary correlate of axonal injury in the experimental autoimmune encephalomyelitis spinal cord: a quantitative pixelwise analysis.* J Neurosci, 2009. **29**(9): p. 2805-13.

41. Wang, Y., et al., *Quantification of increased cellularity during inflammatory demyelination.* Brain, 2011. **134**(Pt 12): p. 3590-601.

42. Millecamps, S. and J.P. Julien, *Axonal transport deficits and neurodegenerative diseases.* Nat Rev Neurosci, 2013. **14**(3): p. 161-76.

43. Wang, F.H., et al., *Decreased axonal transport rates in the Tg2576 APP transgenic mouse: improvement with the gamma-secretase inhibitor MRK-560 as detected by manganese-enhanced MRI.* Eur J Neurosci, 2012. **36**(9): p. 3165-72.

44. Smith, K.D., et al., *In vivo axonal transport rates decrease in a mouse model of Alzheimer's disease.* Neuroimage, 2007. **35**(4): p. 1401-8.

45. Massaad, C.A., et al., *Mitochondrial superoxide contributes to blood flow and axonal transport deficits in the Tg2576 mouse model of Alzheimer's disease.* PLoS One, 2010. **5**(5): p. e10561.

46. Sharma, R., et al., *Hyperglycemia induces oxidative stress and impairs axonal transport rates in mice.* PLoS One, 2010. **5**(10): p. e13463.

47. Cross, D.J., et al., *Age-related decrease in axonal transport measured by MR imaging in vivo.* Neuroimage, 2008. **39**(3): p. 915-26.

48. De Vos, K.J., et al., *Role of axonal transport in neurodegenerative diseases.* Annu Rev Neurosci, 2008. **31**: p. 151-73.

49. Chan, K.C., et al., *Evaluation of the retina and optic nerve in a rat model of chronic glaucoma using in vivo manganese-enhanced magnetic resonance imaging.* Neuroimage, 2008. **40**(3): p. 1166-74.

50. Van der Linden, A., et al., *In vivo manganese-enhanced magnetic resonance imaging reveals connections and functional properties of the songbird vocal control system.* Neuroscience, 2002. **112**(2): p. 467-74.

51. Watanabe, T., J. Frahm, and T. Michaelis, *Functional mapping of neural pathways in rodent brain in vivo using manganese-enhanced three-dimensional magnetic resonance imaging.* NMR Biomed, 2004. **17**(8): p. 554-68.

52. Saleem, K.S., et al., *Magnetic resonance imaging of neuronal connections in the macaque monkey.* Neuron, 2002. **34**(5): p. 685-700.

53. Leergaard, T.B., et al., *In vivo tracing of major rat brain pathways using manganese-enhanced magnetic resonance imaging and three-dimensional digital atlasing.* Neuroimage, 2003. **20**(3): p. 1591-600.

54. Kameyama, K., K. Aono, and K. Kitamura, *Isoflurane inhibits neuronal Ca2+ channels through enhancement of current inactivation.* Br J Anaesth, 1999. **82**(3): p. 402-411.

55. Jevtovic-Todorovic, V., et al., *Anaesthetic neurotoxicity and neuroplasticity: an expert group report and statement based on the BJA Salzburg Seminar.* Br J Anaesth, 2013.

56. Ridder, W.H., 3rd and S. Nusinowitz, *The visual evoked potential in the mouse--origins and response characteristics.* Vision Res, 2006. **46**(6-7): p. 902-13.

57. Hickman, S.J., et al., *A serial MRI study following optic nerve mean area in acute optic neuritis.* Brain, 2004. **127**(Pt 11): p. 2498-505.

58. Ohno, N., et al., *Myelination and axonal electrical activity modulate the distribution and motility of mitochondria at CNS nodes of Ranvier.* J Neurosci, 2011. **31**(20): p. 7249-58.

59. Smith, K.J. and H. Lassmann, *The role of nitric oxide in multiple sclerosis.* Lancet Neurol, 2002. **1**(4): p. 232-41.

60. Waxman, S.G., *Axonal conduction and injury in multiple sclerosis: the role of sodium channels.* Nat Rev Neurosci, 2006. **7**(12): p. 932-41.

61. Kornek, B., et al., *Distribution of a calcium channel subunit in dystrophic axons in multiple sclerosis and experimental autoimmune encephalomyelitis.* Brain, 2001. **124**(Pt 6): p. 1114-24.

62. Craner, M.J., et al., *Sodium channels contribute to microglia/macrophage activation and function in EAE and MS.* Glia, 2005. **49**(2): p. 220-9.

63. Su, K.G., et al., *Axonal degeneration in multiple sclerosis: the mitochondrial hypothesis.* Curr Neurol Neurosci Rep, 2009. **9**(5): p. 411-7.

64. Mao, P.Z. and P.H. Reddy, *Is multiple sclerosis a mitochondrial disease?* Biochimica Et Biophysica Acta-Molecular Basis of Disease, 2010. **1802**(1): p. 66-79.

65. Andrews, H.E., et al., *Mitochondrial dysfunction plays a key role in progressive axonal loss in Multiple Sclerosis.* Med Hypotheses, 2005. **64**(4): p. 669-77.

66. Stys, P.K., *General mechanisms of axonal damage and its prevention.* J Neurol Sci, 2005. **233**(1-2): p. 3-13.

67. Mark, L.P., et al., *Pictorial review of glutamate excitotoxicity: fundamental concepts for neuroimaging.* AJNR Am J Neuroradiol, 2001. **22**(10): p. 1813-24.

68. Pitt, D., P. Werner, and C.S. Raine, *Glutamate excitotoxicity in a model of multiple sclerosis.* Nat Med, 2000. **6**(1): p. 67-70.

69. Trapp, B.D. and K.A. Nave, *Multiple sclerosis: an immune or neurodegenerative disorder?* Annu Rev Neurosci, 2008. **31**: p. 247-69.

70. Macaskill, A.F., et al., *Miro1 is a calcium sensor for glutamate receptor-dependent localization of mitochondria at synapses.* Neuron, 2009. **61**(4): p. 541-55.

71. Rintoul, G.L., et al., *Glutamate decreases mitochondrial size and movement in primary forebrain neurons.* The Journal of neuroscience : the official journal of the Society for Neuroscience, 2003. **23**(21): p. 7881-8.

72. Hollenbeck, P.J. and W.M. Saxton, *The axonal transport of mitochondria.* J Cell Sci, 2005. **118**(Pt 23): p. 5411-9.

73. Fang, C., D. Bourdette, and G. Banker, *Oxidative stress inhibits axonal transport: implications for neurodegenerative diseases.* Mol Neurodegener, 2012. **7**: p. 29.

74. Stagi, M., et al., *Breakdown of axonal synaptic vesicle precursor transport by microglial nitric oxide.* J Neurosci, 2005. **25**(2): p. 352-62.

75. Redford, E.J., R. Kapoor, and K.J. Smith, *Nitric oxide donors reversibly block axonal conduction: demyelinated axons are especially susceptible.* Brain, 1997. **120 (Pt 12)**: p. 2149-57.

76. Smith, K.J., et al., *Electrically active axons degenerate when exposed to nitric oxide.* Ann Neurol, 2001. **49**(4): p. 470-6.

77. Rodriguez, M., *A function of myelin is to protect axons from subsequent injury: implications for deficits in multiple sclerosis.* Brain, 2003. **126**: p. 751-752.

78. O'Neill, J.K., et al., *Optic neuritis in chronic relapsing experimental allergic encephalomyelitis in Biozzi ABH mice: demyelination and fast axonal transport changes in disease.* J Neuroimmunol, 1998. **82**(2): p. 210-8.

79. Shea, T.B., C. Jung, and H.C. Pant, *Does neurofilament phosphorylation regulate axonal transport?* Trends Neurosci, 2003. **26**(8): p. 397-400.

80. Roy, S., et al., *Neurofilaments are transported rapidly but intermittently in axons: implications for slow axonal transport.* J Neurosci, 2000. **20**(18): p. 6849-61.

Chapter 4

White-Matter Diffusion fMRI of Mouse Optic Nerve

This chapter represents a modified version of a manuscript initially published in NeuroImage. (William M. Spees, Tsen-Hsuan Lin, Sheng-Kwei Song White-Matter Diffusion fMRI of Mouse Optic Nerve. NeuroImage, 2013, 65: 209-215)

Author Contributions

S.-K.S. and W.M.S. designed the experiments. W.M.S. assembled the apparatus for in-magnet visual stimulation. T.-H.L. acquired experimental data with input from S.-K.S. and W.M.S. T.-H.L. and W.M.S. performed data analyses. W.M.S. wrote the manuscript with input from S.-K.S. and T.-H.L.

Abstract

Non-invasive assessment of white-matter functionality in the nervous system would be a valuable basic neuroscience and clinical diagnostic tool. Using standard MRI techniques, a visual-stimulus-induced 22% decrease in the apparent diffusion coefficient of water perpendicular to the axonal fibers ($ADC_{\perp}$) is demonstrated for C57BL/6 mouse optic nerve *in vivo*. A slight increase in $ADC_{\parallel}$ (diffusion parallel to the optic nerve fibers) was observed during visual stimulation. The stimulus-induced changes are completely reversible. A possible vascular

contribution was sought by carrying out the $ADC_{\perp}$ measurements in hypercapnic mice with and without visual stimulus. No differences were seen between room-air-breathing and hypercapnic animals. The *in vivo* stimulus-induced $ADC_{\perp}$ decreases are roughly similar to literature reports for *ex vivo* rat optic nerve preparations under conditions of osmotic swelling. The experimental results strongly suggest that osmotic after-effects of nerve impulses through the axonal fibers are responsible for the observed ADC decrease.

4.1 Introduction

Currently functional MRI (fMRI) studies are limited almost exclusively to gray matter, and rely upon coupling of hemodynamic response to functional activation [1]. Signal modulations on the order of 1 – 5% are typical. The limited capacity for physiologic modulation of blood flow and the inherently lower fractional blood volume probably account for the difficulty in monitoring white-matter functional activation with standard BOLD (Blood Oxygen Level Dependent) fMRI techniques [2, 3]. Thus, at present, white-matter MRI is largely restricted to probing the structural integrity of fiber tracts using diffusion tensor imaging or variants thereof [4].

Diffusion weighting has been investigated as a potential alternative to BOLD for monitoring neuronal activity in gray matter of the human visual cortex [5]. An ~1 - 2% increase in diffusion weighted MRI signal intensity was reported ($b = 1.8$ ms/μm^2), suggested to arise from activity-dependent cell swelling. In a subsequent report, a similar diffusion-weighted MRI signal intensity increase was elicited via hypercapnia-induced brain blood flow enhancement without neuronal activation [6]. Thus, the specificity of diffusion fMRI signal change to neuronal activity may be confounded by a sizeable vascular contribution.

In *ex vivo* rat optic nerve preparations, repeated electrical stimulation produces frequency- and duration-dependent shrinkage of the extracellular space (ECS), with higher frequencies and longer stimulus trains resulting in a more pronounced ECS reduction [7]. A consensus has emerged that the observed ECS shrinkage results from an osmotic shift of water into glial cells as part of a mechanism for maintaining extracellular ionic balance and neuronal electrophysiologic competence [8-11].

To determine the feasibility of detecting diffusion weighted MRI signal changes in white matter responding to functional stimulation, as well as the specificity of this signal change to axonal activation, optic nerves from room-air-breathing and hypercapnic mice were examined with and without the application of visual stimulus.

4.2 Materials and Methods

4.2.1 Animal

All experimental procedures were in compliance with the protocol approved by the Washington University Animal Studies Committee. Female C57BL/6 mice, aged 10 – 12 weeks, obtained from Jackson Laboratory (Bar Harbor, ME) were used in the experiments.

4.2.2 Visual Acuity

Prior to MRI experiments, visual acuity of each mouse was measured with a Virtual Optokinetic System (CerebralMechanics, Inc.) as previously reported [12], to ensure normal vision.

4.2.3 Animal Monitoring

Respiratory rate and rectal temperature of anesthetized mice were monitored during experiments using an MR-compatible animal monitoring system (Small Animal Instruments, Inc., Stony Brook, NY) to ensure physiologic stability. A body-core temperature of 37ºC was maintained via a circulating warm water pad placed underneath the animal and thermostated warm air blown into the magnet bore.

4.2.4 Anesthesia

The anesthesia regimen employed has been shown to maintain fMRI-observable neuronal response in mice [13]. Anesthesia was induced with 2.5% isofluorane in O_2, and reduced to 1.5% for placement of the animal in the imaging cradle. After positioning of the animal in a head holder and achieving a stable respiratory rate, a subcutaneous 0.3 mg/kg bolus of medetomidine was administered. Beginning three minutes after the bolus injection, isofluorane levels were reduced by ~ 0.2% per minute until the inhaled gas consisted of 100% O_2. At 10 minutes after the bolus injection, continuous subcutaneous infusion of medetomidine was initiated at a rate of 0.6 mg/kg/hr, and the nose cone for inhalant anesthetics was removed, leaving the animal breathing room air for the duration of the MR experiment. In experiments investigating the effect of hypercapnia (air vs. 5% CO_2/95% O_2), the animal, head holder, and other equipment was placed in a closed plastic tube that allowed control of breathing gas composition.

4.2.5 Magnetic Resonance Imaging

MRI experiments were performed on a 4.7-T Agilent DirectDrive^{TM} Small-Animal MRI system (Agilent Technologies, Santa Clara, CA), equipped with Magnex/Agilent HD imaging gradients (Magnex/Agilent, Oxford, UK). The gradient hardware, interfaced with a set of IEC 300 A gradient power amplifiers (International Electric Company, Helsinki, Finland), is capable of pulsed gradient strengths up to 58 G/cm with a gradient rise time ≤ 295 μs. An actively-decoupled volume (transmit)/surface (receive) coil pair was used for MR excitation and signal reception [14]. A diffusion-weighted, multi-echo spin-echo imaging sequence [15] was employed for scout images and also for the final targeted diffusion-weighted images (Fig. 4 – 1).

To minimize partial volume effects in optic nerve diffusion measurements, the image plan was adjusted to ensure that, as nearly as possible, the optic nerve fibers were orthogonal to the image slice plane (Figs. 4 – 2b and 4 – 2c). Image acquisition parameters included a slice thickness of 1.3 mm and a 20×20 mm^2 (256×256) field-of-view. A sequence repetition time of 1.5 s was employed, thus the total acquisition time for a pair of diffusion-weighted images probing a single diffusion direction was 12.8 minutes. To increase accumulated signal-to-noise ratio for each phase-encoding step, a train of three echoes were co-added to form the final MR images. The first echo time (which included a pair of diffusion-weighting gradient lobes centered about the 180° refocusing pulse) was 37.1 ms, with a spacing of 23.6 ms between the first and all subsequent echoes without diffusion gradients.

Some evidence for attenuated changes in ADC with repeated applications of visual stimulus after the initial "on" block was seen (data not shown). This could possibly result from accumulation of inactive forms of retinal rhodopsin during the rather lengthy 12.8-minute stimulus block [16]. To avoid potentially confounding results, $ADC_{\perp}$ and $ADC_{\parallel}$ were measured in separate cohorts of animals.

For each experimental condition (e.g., baseline, visual "stimulus on", post- "stimulus off", etc.) a pair of diffusion-weighted images with different diffusion weightings was acquired (Fig. 4 – 2c). For the cohort in which $ADC_{\perp}$ was evaluated, b values of 0.10 ms/μm^2 and 1.40 ms/μm^2 were used (δ = 5 ms, Δ = 18 ms, G_{diff} = 6 G/cm or 22.6 G/cm for a pair of trapezoidal diffusion-weighting gradients). Because of the much less restricted diffusion along the axis of the optic nerve (Fig. 4 – 3), measurements in the $ADC_{||}$ cohort were made based on a pair of diffusion-weighted images having b values of 0.10 ms/μm^2 and 0.70 ms/μm^2 (δ and Δ were the same as for

$ADC_{\perp}$ measurements, but G_{diff} = 6 G/cm or 15.5 G/cm). It is worth pointing out that, in the diffusion MR literature, b values reported in units of s/mm^2 are not uncommon, with ADC being reported in mm^2/s units in that case. To convert to those units, our numerical values for b should be multiplied by 1,000 and our ADC numbers divided by 1,000.

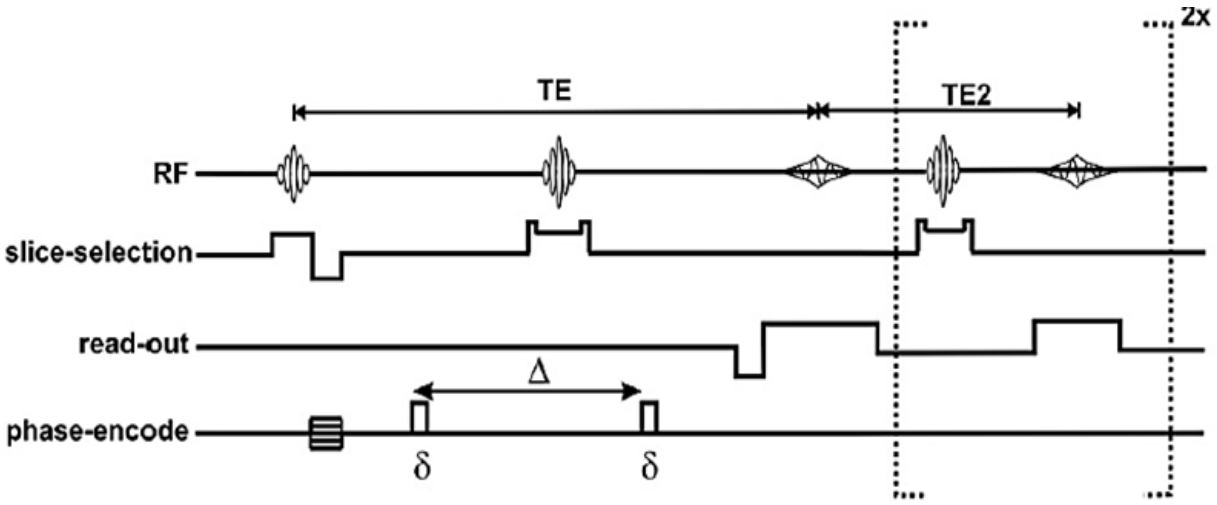

Figure 4 – 1 Pulse sequence diagram for the diffusion-weighted multi-spin-echo sequence. Timing parameters include: δ = 5 ms, Δ = 18 ms, TE = 37.1 ms TE2 = 23.6 ms.

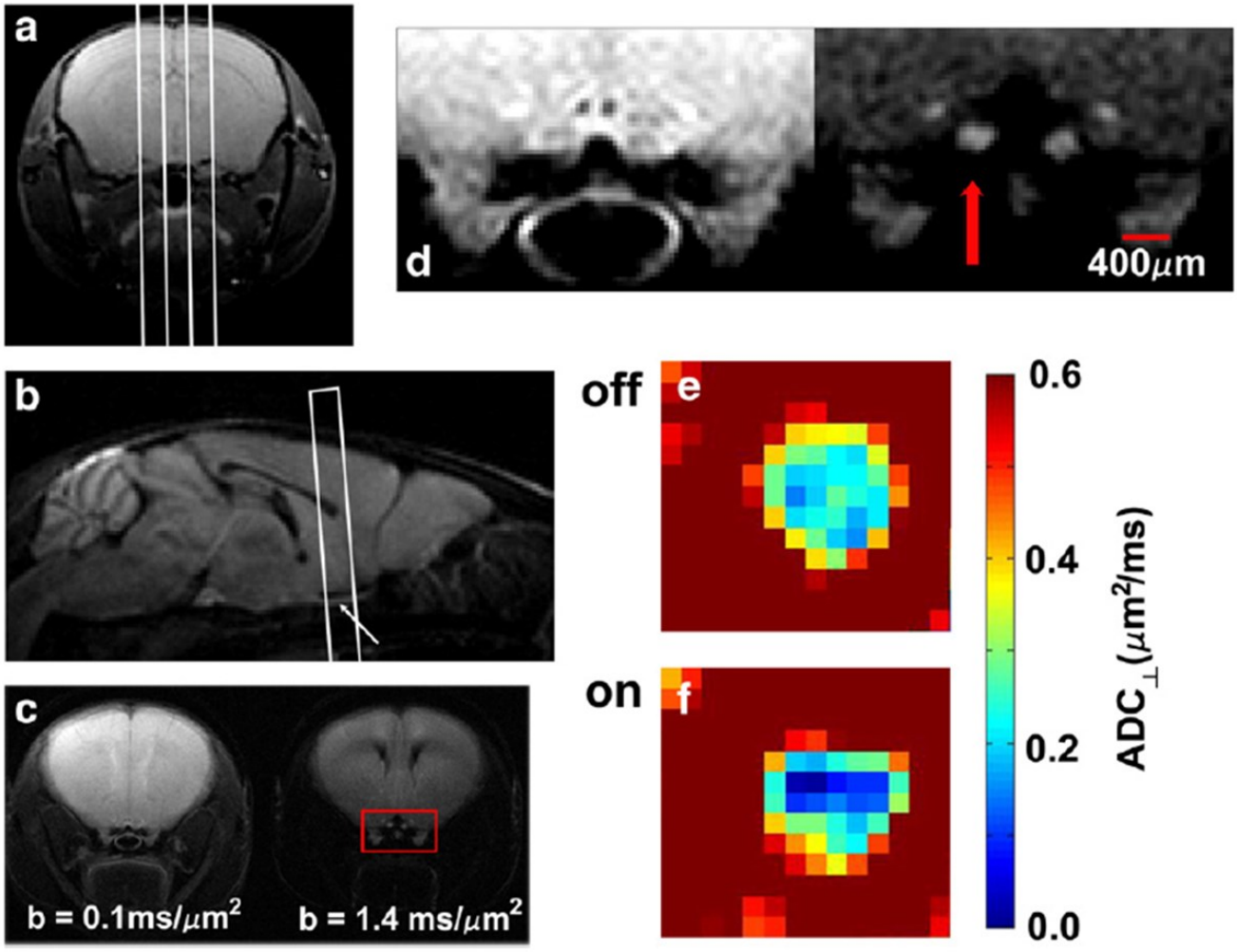

Figure 4 – 2 Typical scout planning images **(a,b)**, final targeted images for diffusion measurements **(c,d)**, and $ADC_{\perp}$ maps of an optic nerve without **(e)** and with visual stimulation **(f)**. **(a)** A multi-slice set of axial images of the mouse brain is acquired with a non-diffusion-weighted multi-echo spin-echo image (only a single slice is shown here) are used to plan sagittal slices, indicated by the white lines. **(b)** The center sagittal slice, acquired with diffusion-weighting gradients applied in the slice-select direction, captures both optic nerves (arrow) and is used to target the slice for measurements of $ADC_{\perp}$ and $ADC_{\parallel}$. **(c)** A pair of diffusion-weighted images with diffusion-sensitizing gradients applied in the phase-encode direction (left-to-right in the images). The optic nerve fibers are perpendicular to the slice plane in this final targeted slice. **(d)** Magnified view of the area within the red box of panel **c**. Both optic nerves are visible with the stimulated optic nerve indicated by the red arrow. Color maps of $ADC_{\perp}$ in an experimental optic nerve without **(e)** or with **(f)** visual stimulation.

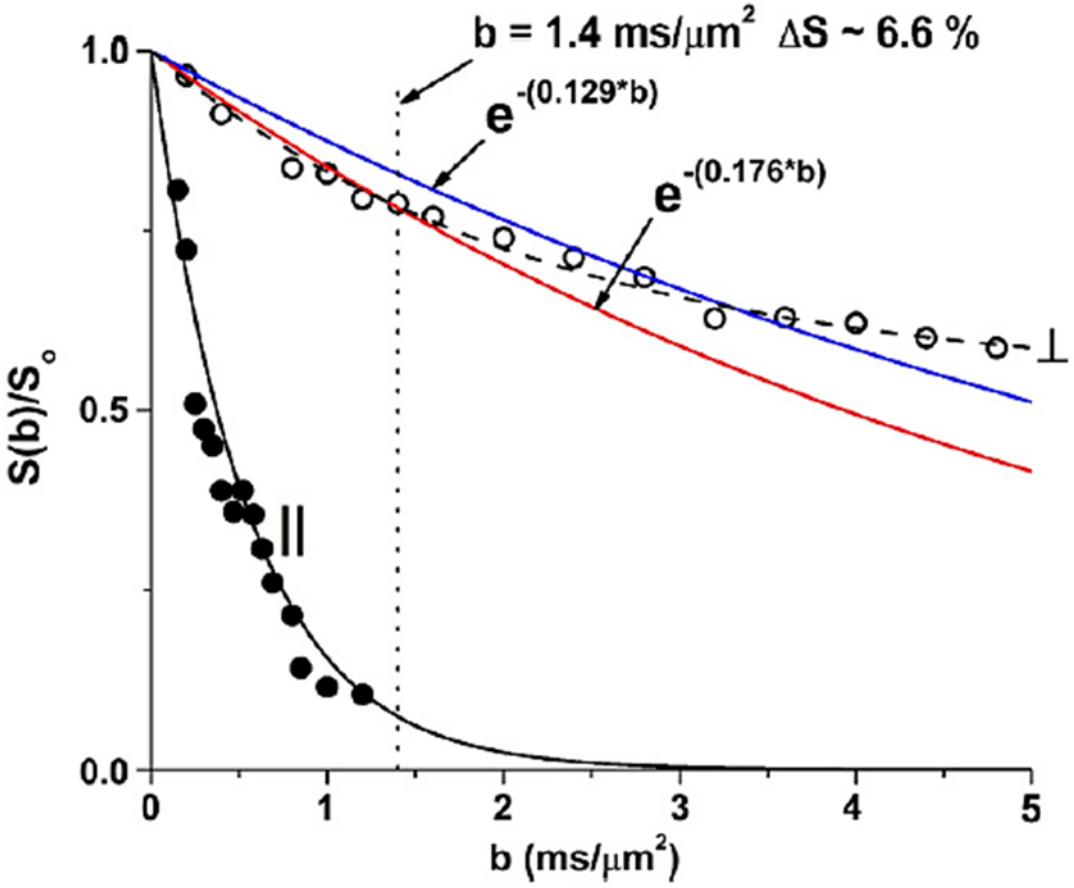

Figure 4 – 3 Diffusion attenuation curves for mouse optic nerve with diffusion weighting perpendicular and parallel to the nerve fibers (without visual stimulation), acquired with (δ = 5 ms, Δ = 18 ms). Parallel diffusivity is essentially mono-exponential. It is readily apparent that diffusion perpendicular to the fibers is highly restricted and non-monoexponential. The blue and red curves are constructed with $ADC_{\perp}$ = 0.11 μm^2/ms (blue curve, representative of activated optic nerve) and $ADC_{\perp}$ = 0.16 μm^2/ms (red curve, representative of unstimulated optic nerve). The estimated changes in $ADC_{\perp}$ from the mono-exponential data modeling indicate an approximately 5.7% signal increase at b = 1.4 ms/μm^2 with visual stimulation.

4.2.6 Visual Stimulation

Visual stimulation was achieved by repetitive flashing of a high-intensity, white LED (Cree, Model C503C-WAS) fixed at a position 5 cm in front of the animal's nose and aimed at one of the animal's eyes. Light was blocked out of the contralateral eye with two layers of black electrical tape. A step-function signal of 1.4 Hz frequency [17], 200 ms on/514 ms off, with amplitude of 4 V/0 V (on/off) was provided by a Grass Instruments S9 stimulator (Grass Technologies, West Warwick, RI). With a 100 Ω series current-limiting resistor, the forward voltage across the LED is 3.2V. The circuit draws 8 mA of DC current in the "on" state, corresponding to a luminous intensity of ~ 14 candela. DC current was carried from the stimulator (outside the magnet) through the LED (inside the RF-shielded bore of the magnet) by a pair of coaxial BNC cables. Additionally, a pair of 3-segment LC filters was placed on each BNC line where it fed into the magnet bore to eliminate delivery of unwanted RF interference into the magnet. The outer conductor of each BNC line was grounded to the magnet's RF shield at the feedthrough into the magnet. In MRI measurements with "stimulus on", the flashing light stimulus was applied for the entire 12.8-minute duration of the imaging acquisition.

While white matter tends to be less well-vascularized than gray matter structures, the vascularization of the mouse optic nerve is not negligible, with retinal venous drainage routed within close proximity to the ROI investigated [18]. In order to determine the effect of possible dilation of optic nerve vasculature and associated changes in blood oxygenation level on the observed $ADC_{\perp}$ decrease, "baseline" and "stimulus on" measurements were also made in anesthetized mice breathing a mixture of 5% CO_2/95% O_2 (n = 5). In cases where the breathing-gas composition was changed, a period of 5 minutes was allowed prior to the commencement of MR measurements.

4.2.7 Data Processing and Image Segmentation

All MR images were zero-filled to 512 × 512 data matrices. To ensure the absence of any possible hardware-related systematic variation in image signal, the ADC was determined in a 20 × 20 region-of-interest drawn within the basal forebrain (a brain region not expected to be activated with visual stimulation, but located within a reasonable proximity to the optic nerves) and the contralateral/control non-stimulated optic nerve from each pair of diffusion-weighted images. The regions of interest (the optic nerves) were manually outlined on an image with b = 1.40 ms/μm^2 diffusion-weighting perpendicular to the optic nerve fiber direction, which provides fairly clear definition of the optic nerves (Figs. 4 – 2c and 4 – 2d). Voxels on the outer periphery of the optic nerve were excluded from the ROI. Optic nerve ROIs consisted of ~ 20 voxels or ~ 30,000 μm^2 [range: 16 – 26 after zero-filling (24,000 – 40,000 μm^2), corresponding to 4 – 6 voxels before zero-filling), for which individual apparent diffusion coefficients were calculated. These individual voxelwise values were pooled together for subsequent statistical analyses.

The signal intensity, S(b), in the range of b values employed for $ADC_{\parallel}$ and $ADC_{\perp}$ estimation is essentially a monoexponential decay, although the signal-decay behavior, it should be noted, is more complex than this over a wider range of b values (Fig. 4 – 3). As is commonly done in measurements at only two b values, the following equation (Eq. (4.1)) was employed to estimate both $ADC_{\parallel}$ and $ADC_{\perp}$:

$$\ln\left[\frac{S(b')}{S(b)}\right] = -(b' - b)\cdot \mathrm{ADC}. \qquad (4.1)$$

The contrast in parallel-diffusion-weighted images does not readily reveal the definition of the optic nerve. For measurements of $ADC_{\parallel}$, each pair of diffusion-weighted images was preceded and followed by a single diffusion-weighted image with diffusion gradients applied perpendicular to the nerve fibers and b = 1.40 ms/μm^2. The definition of the ROI was then prescribed referencing the images acquired with perpendicular diffusion weighting.

4.2.8 Statistical Tests

One-way ANOVA with Tukey test post-hoc means comparison was performed to assess differences between group data (e.g., ipsilateral optic nerve: "baseline" vs. "stimulus on" vs. "stimulus off", contralateral optic nerve: "baseline" vs. "stimulus on", etc.).

4.3 Results

The imaging protocol employed provides good quality images of the mouse optic nerve. Signal-to-noise ratio varied across the study animals in the range from 22.3 to 30.3 with low diffusion weighting ($b = 0.1$ ms/μm^2) and 17.2 to 25.1 for higher diffusion weightings ($b = 1.4$ ms/μm^2).

In the cohort of animals for which $ADC_{\perp}$ was measured (n = 5 mice), a sizeable and statistically significant 22% decrease ($p = 0.0019$, Baseline vs. Stimulus On) from 0.172 ± 0.004 μm^2/ms to 0.134 ± 0.003 μm^2/ms (mean ± sem, see Fig. 4 – 4 and Table 4 – 1) was observed. In individual animals, the range of $ADC_{\perp}$ decrease with stimulation was between 10% and 34%. The change was completely reversible with cessation of visual stimulation. In the contralateral control optic nerve, no systematic variation in $ADC_{\perp}$ was detectable with application of stimulus to the ipsilateral eye (Fig. 4 – 4). Additionally, the ADC measurements from within the reference basal forebrain region were quite stable with variations no more than 3% both intra- and inter-subject. From the inset in Figure 4, it can be appreciated that the inter-subject variation in $ADC_{\perp}$ is then largely a result of partial volume effects as the mouse optic nerve is surrounded by CSF which, by comparison, has a relatively high diffusivity.

A small, but still statistically significant increase (3%) in optic nerve $ADC_{\parallel}$ ($p = 3.0 \times 10^{-5}$) was observed with visual stimulation (Fig. 4 – 5 and Table 4 – 1, n = 6 mice). Similar to the $ADC_{\perp}$ measurements, the reduction in $ADC_{\parallel}$ in the presence of visual stimulus was reversible and no changes were detectable in the contralateral optic nerve with visual stimulation. A decreased $ADC_{\parallel}$ was observed in all ipsilateral optic nerves with visual stimulation, with the percent change varying between 7.3% and 13.6% across the members of this cohort. Again,

ADC in the basal forebrain region was very stable across and within animals studied in this group.

Using the $ADC_{\parallel}$ and $ADC_{\perp}$ results in Table 1 and assuming cylindrical geometry, the fractional anisotropy for mouse optic nerve can be estimated [19]. For the resting state mouse optic nerve FA = 0.90. With the applied flashing-light stimulus FA increases to 0.93. Via a similar analysis, an orientationally-averaged diffusivity, $\langle D \rangle$, of 0.71 $\mu m^2/ms$ is estimated for the resting-state optic nerve, which decreases by ~ 14 % to 0.61 $\mu m^2/ms$ during the application of visual stimulus.

Hypercapnia, by itself, produced no measureable changes in the optic nerve $ADC_{\perp}$ (Fig. 4 – 6 and Table 4 – 2, n = 5 mice). An activation-induced reversible 25% decrease in optic nerve $ADC_{\perp}$ ($p = 0.024$) was observed in hypercapnic mice, essentially the same extent as seen in room-air-breathing animals. This strongly suggests that the observed decrease in optic nerve ADC with visual stimulation does not arise from a vascular effect [6] and is produced entirely as a result of repeated axonal firing. The effect of hypercapnia and hypercapnia + stimulation on $ADC_{\parallel}$ was not investigated.

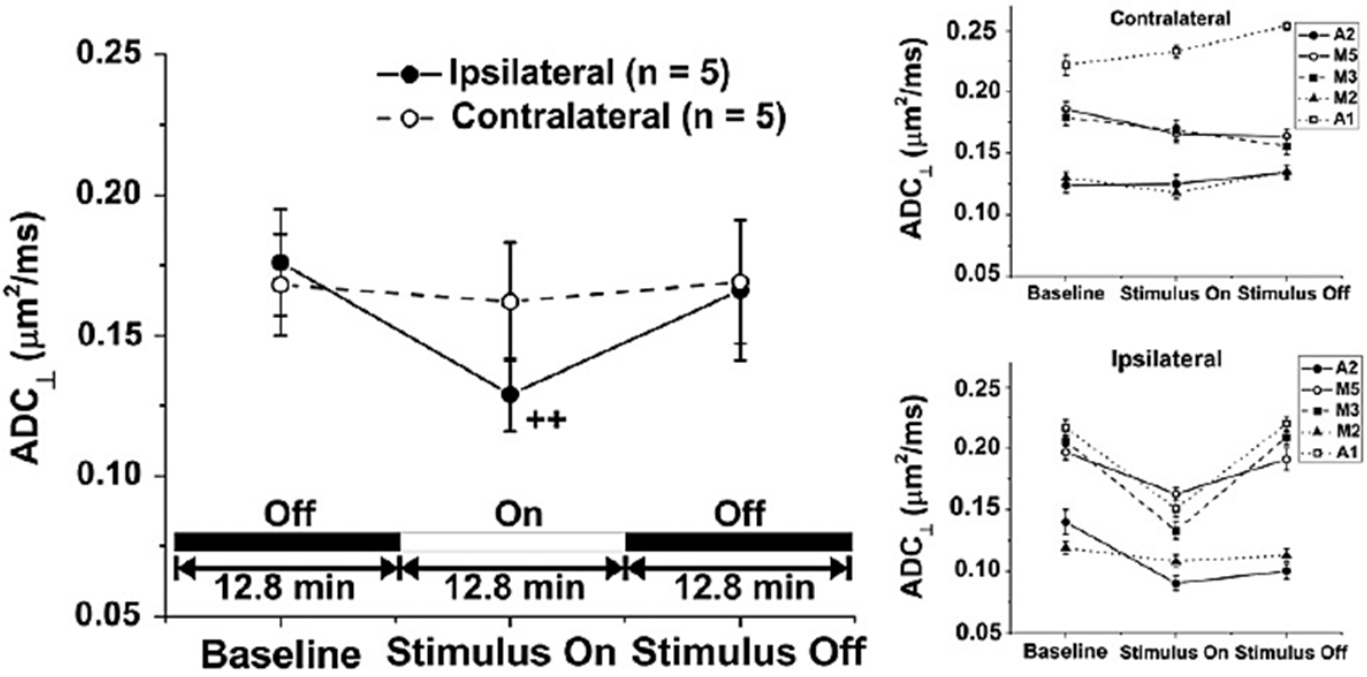

Figure 4 – 4 Application of visual stimulus produces a significant drop in $ADC_{\perp}$ for the optic nerve of the stimulated eye [Baseline: 0.153 ± 0.007 $\mu m^2/ms$ (mean ± sem), Stimulus On: 0.110 ± 0.006 $\mu m^2/ms$, ++: $p = 0.0019$], but no change for the contralateral, unstimulated eye. $ADC_{\perp}$ in the ipsilateral optic nerves returns to baseline values once again with removal of the stimulus. Quantities shown are the mean ± sem for image voxels within the optic nerve ROI in a group of five experimental mice breathing room air. The insets depicts the measurements for the experimental/ipsilateral and control/contralateral optic nerves in individual animals.

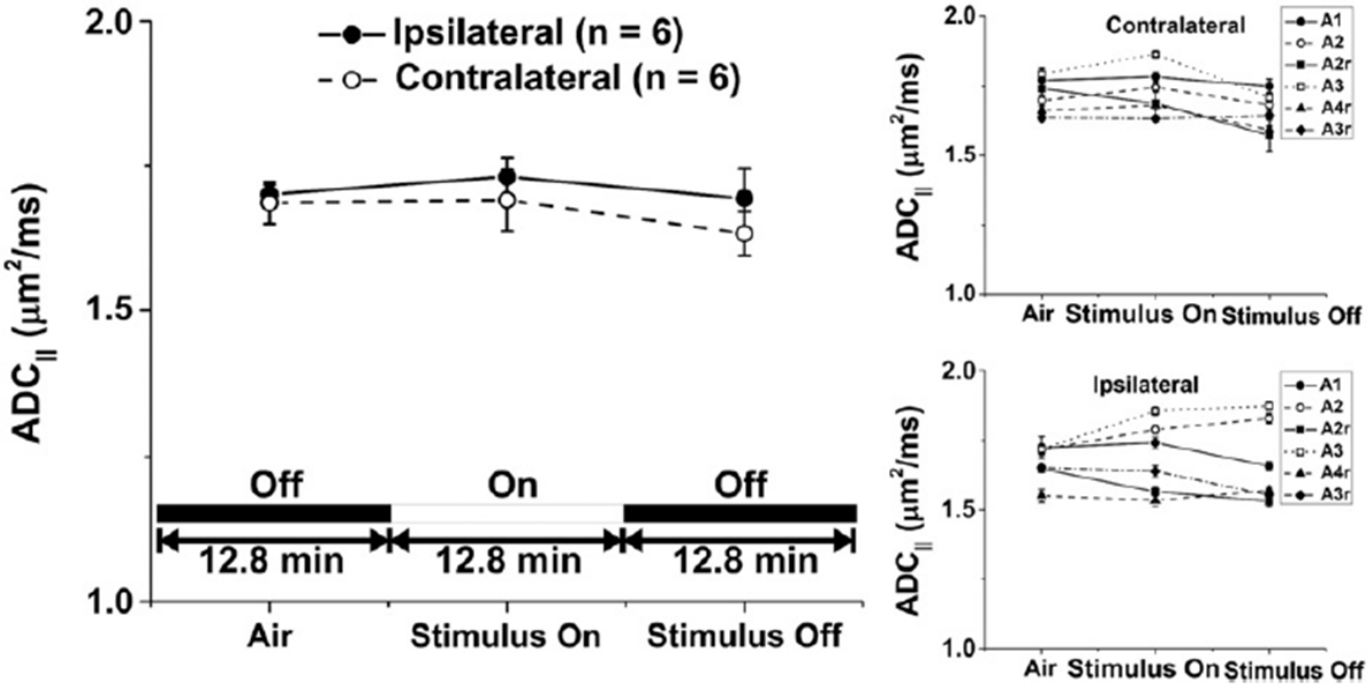

Figure 4 – 5 Stimulus and $ADC_{||}$ in optic nerve of mice breathing room air. Quantities plotted are (mean ± sem). Stimulation produces no statistically-significant changes in $ADC_{||}$

Table 4 – 1

Measured $ADC_{\perp}$ (mean ± sem, n = 5) and $ADC_{\parallel}$ (mean ± sem, n = 6) for *In Vivo* Mouse Optic Nerve in Room-Air-Breathing Mice.

Condition	Ipsilateral $ADC_{\perp}$ ($\mu m^2/ms$)	Contralateral $ADC_{\perp}$ ($\mu m^2/ms$)	Ipsilateral $ADC_{\parallel}$ ($\mu m^2/ms$)	Contralateral $ADC_{\parallel}$ ($\mu m^2/ms$)
Baseline	0.176 ± 0.019	0.168 ± 0.018[c]	1.70 ± 0.02	1.69 ± 0.04
Stimulus On	0.129 ± 0.013[a]	0.162 ± 0.021[d]	1.73 ± 0.03[f]	1.69 ± 0.05
Stimulus Off	0.166 ± 0.025[b]	0.169 ± 0.022[e]	1.69 ± 0.03[g]	1.63 ± 0.04

a: p = 0.0008 vs. Ipsilateral "Baseline" group

b: p = 0.005 vs. Ipsilateral "Stimulus On" group

c: p = 0.004 vs. Ipsilateral "Stimulus On" group

d: p = 0.01 vs. Ipsilateral "Stimulus On" group

e: p = 0.003 vs. Ipsilateral "Stimulus On" group

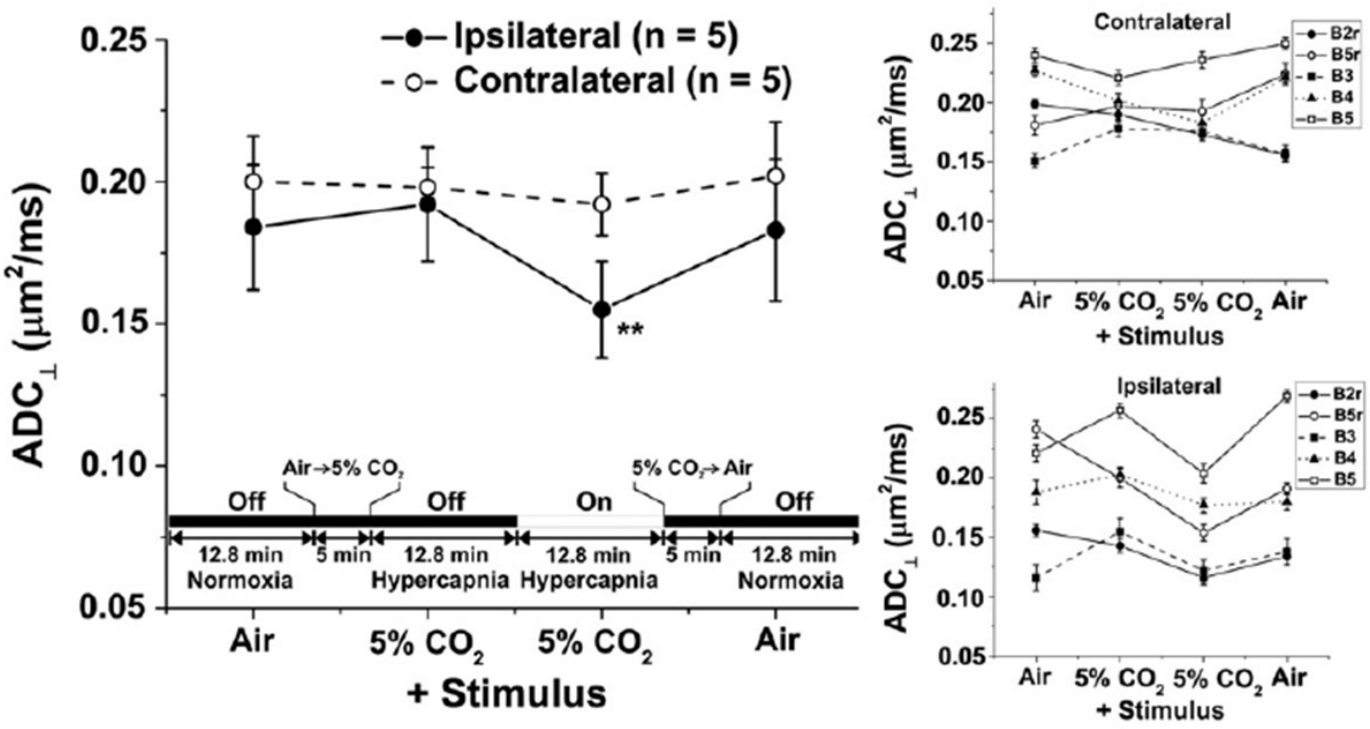

Figure 4 – 6 The effects of hypercapnia on measured $ADC_{\perp}$ (mean ± sem) with and without stimulation were investigated in a set of mice in order to quantify vascular contributions to the observed phenomenon. The effects of stimulation on $ADC_{\perp}$ (a 19% decrease) were similar to changes seen in animals breathing room air.

Table 4 – 2

Measured $ADC_{\perp}$ (mean ± sem) for *In Vivo* Mouse Optic Nerve in Mice Breathing Air or 5% CO_2/95% O_2 (n = 5).

Condition	Ipsilateral $ADC_{\perp}$ ($\mu m^2/ms$)	Contralateral $ADC_{\perp}$ ($\mu m^2/ms$)
Air, Baseline	0.184 ± 0.022	0.200 ± 0.016[d]
5% CO_2, Baseline	0.192 ± 0.020	0.198 ± 0.007[e]
5% CO_2 + Stimulus	0.155 ± 0.017[a,b]	0.192 ± 0.011[f]
Air, Stimulus Off	0.183 ± 0.025[c]	0.202 ± 0.019[g]

a: p = 0.03 vs. Ipsilateral "Air, Baseline" group

b: p = 0.008 vs. Ipsilateral "5% CO_2, Baseline" group

c: p = 0.04 vs. Ipsilateral "5% CO_2 + Stimulus" group

d: p = 0.002 vs. Ipsilateral "5% CO_2 + Stimulus" group

e: p = 0.002 vs. Ipsilateral "5% CO_2 + Stimulus" group

f: p = 0.007 vs. Ipsilateral "5% CO_2 + Stimulus" group

g: p = 0.001 vs. Ipsilateral "5% CO_2 + Stimulus" group

4.4 Discussion

Our results show that *in vivo* diffusion MRI is capable of detecting the $ADC_{\perp}$ decrease (~28%) accompanying mouse optic nerve activation in medetomidine-anesthetized mice. The activation-associated $ADC_{\perp}$ decrease is independent of blood flow effects since hypercapnia alone does not produce observable changes, and a similar activation-induced decrement in $ADC_{\perp}$ was seen in hypercapnic and air-breathing mice. The extent of *in vivo* $ADC_{\perp}$ change is comparable to that reported (31 ± 8% decrease) for depolarization and osmotic swelling of *ex vivo* rat optic nerve at 21ºC [20] supporting the notion that decreased ECS (Sen and Basser, 2005) may be responsible for the detected ADC change.

Decreased ADC is a hallmark of repeated, synchronous neuronal discharge in CNS. For example, 11 – 35% decreases in ADC were observed in 10 patients with complex partial status epilepticus [21]. Application of trains of electrical shocks, administered via carbon electrodes placed on the surface the rat brain, have been shown to result in an 8% decrease in gray-matter water ADC [22]. Spreading depression also produces a transient ADC drop [23, 24]. While all of these conditions produce membrane depolarization and subsequent cellular swelling [24], it is likely the cellular swelling aspect that is directly responsible for the observed changes in tissue water diffusion. For instance, membrane depolarization without cell swelling was not sufficient to produce changes in ADC in *ex vivo* rat optic nerve [20].

In the current study, repetitive axonal firing within the optic nerve is expected to result from the flashing light stimulus. The frequency of 1.4 Hz for the repetitive light flashing was chosen since it is in the region of maximal response in the electroretinogram and visual evoked

potential (voltage amplitude vs. flashing-stimulus frequency), as reported previously for measurements in C57BL/6 mice [17].

In the visual system, light intensity information is encoded by the excitation frequency of retinal ganglion cells [25] with faithful transmission of the photoreceptor action potentials to the brain via the optic nerve. It is likely that during the 200ms-long pulses of bright light (repeated at 1.4 Hz temporal frequency), the mouse optic nerves are repetitively transmitting action potentials at frequencies of many tens of Hz [26, 27]. *Ex vivo* rat optic nerves have been shown to undergo an ECS shrinkage that is more pronounced at higher rates of repeated electrical stimulation [7]. While it was not investigated here, we would expect that the ADC response in optic nerve should be graded in proportion to intensity of the applied stimulus. Earlier attempts to measure changes in $ADC_{\parallel}$ and $ADC_{\perp}$ in electrically-stimulated white matter of the *ex vivo* frog spinal cord were unsuccessful [28], possibly due to the low-frequency (2.7 Hz average) of the applied electrical stimulus.

Taken together, our results for $ADC_{\perp}$ and $ADC_{\parallel}$ predict an enhanced relative anisotropy for activated white-matter fibers. Provided that stimulus paradigms can be devised for activating specific white-matter pathways [3], it may be possible to monitor brain white-matter activation. A recent report was aimed at detecting white-matter diffusion anisotropy changes in humans with visual and tactile stimuli [29]. The conclusion reached in that study was that a large number of measurements would be required for reliable detection of diffusion MRI signal changes. This lack of sensitivity may reflect more on the need for higher spatial resolution (to avoid partial volume effects) than a lack of robust physiological response.

In the current study, we have used two diffusion-weighted measurements to estimate the ADC of optic nerve with and without visual stimulation, assuming diffusion-attenuated signal decays as a single exponential. As can readily be seen from Figure 3, this is approximately correct over the range of b values employed for estimation of $ADC_{\perp}$ and $ADC_{\parallel}$. Measurement with diffusion-weighting perpendicular to the optic nerve and b = 1.40 ms/μm^2 result in a relative signal intensity change of ~ 5.7% with vs. without stimulation.

Hypercapnia, a potent vasodilator and modulator of CNS blood flow (Rostrup et al., 2000), by itself did not elicit signal changes in the mouse optic nerve. A modulation in tissue ADC is one conceivable consequence of vasodilation (increased delivery of oxygenated blood) with the same level of tissue oxygen consumption. The vascular network, especially the venous network, contains some amount of relatively paramagnetic deoxyhemoglobin. The confinement of this paramagnetic material to the venous network produces unintended tissue-internal magnetic field gradients (in addition to the intentionally-applied diffusion-weighting gradients). Reducing the tissue-internal field gradients, by reducing vascular deoxyhemoglobin content, can produce an increased tissue ADC [30, 31]. No such effects were observable in hypercapnic mice and essentially the same relative decrease in $ADC_{\perp}$ was seen with stimulation in hypercapnic and room-air-breathing animals.

We believe that ECS shrinkage in the optic nerve with visual stimulation is the cause of the observed ADC decrease. Interestingly, for both the rat optic nerve [7] and rat spinal cord gray matter [10], the extent of activity-dependent ECS shrinkage (from repeated electrical stimulation) is correlated with age of the animal. Both sets of authors noted that a key developmental feature in the maturation of these tissues is gliogenesis. Glial cells are often implicated as the dominant contributors to activity-induced ECS shrinkage in neural tissue [32, 9,

8]. As recently reviewed by Rash [11] the pan glial syncytium (involving gap-junction-interconnected astrocytes, epindymocytes and oligodendrocytes--including direct involvement of myelin-bounded cytoplasmic spaces), is believed to provide a dynamic mechanism for potassium siphoning. This means of moving K^+ and osmotically accompanying water away from the axonal exterior is believed to allow for re-establishment of axonal membrane polarization required for the repeated propagation of action potentials.

It should be noted, that in addition to glial swelling, there is evidence for activity-dependent swelling of neuronal processes. Long-lasting swelling of dendritic spines has been reported following a 30-second period of *in vivo* electrical stimulation in mouse brain [33]. Also, transient axonal swelling, coincident with passage of the compound action potential has been observed in the non-myelinated garfish olfactory nerve *ex vivo* [34]. Thus neuronal cells may make some additional contribution to activity-dependent shrinkage of the extracellular space in white matter. Regardless of the precise cellular origins, ECS shrinkage would be expected to result in an overall reduction in tissue water diffusivity. Indeed, in mathematical modeling of diffusion in white matter, the extracellular volume fraction is shown to be a dominant factor in determining the overall tissue diffusion characteristics [35].

Regardless of any role that myelin itself might play in ECS shrinkage, which we believe to be at the root of the stimulus-induced ADC changes in the optic nerve, intact myelin is a requirement for normal white-matter functionality [36]. This suggests that functional diffusion MRI measurements in white matter tracts could find utility as a specific marker of white-matter lesions in demyelinating diseases (e.g., multiple sclerosis) with possible utility in directly monitoring disease progression or treatment response.

Acknowledgements

The authors thank Professors Joseph J.H. Ackerman and Marcus Raichle for valuable discussions. This work was supported in part by the Mallinckrodt Institute of Radiology; NIH R01NS047592, P01NS059560 and 5R01EB00208; and NMSS RG 4549A4/1

4.5 References

1. Logothetis, N.K., *What we can do and what we cannot do with fMRI.* Nature, 2008. **453**: p. 869-878.

2. Rostrup, E., et al., *Regional Differences in the CBF and BOLD Responses to Hypercapnia: A Combined PET and fMRI Study.* NeuroImage, 2000. **11**: p. 87-97.

3. Gawryluk, J.R., et al., *Optimizing the detection of white matter fMRI using asymmetric spin echo spiral.* NeuroImage, 2009. **45**: p. 83-88.

4. Jones, D.K., ed. *Diffusion MRI: Theory, Methods, and Applications.* 1st ed. 2010, Oxford University Press USA.

5. Le Bihan, D., et al., *Direct and fast detection of neuronal activation in the human brain with diffusion MRI.* Proc. Natl. Acad. Sci., USA, 2006. **103**(21): p. 8263-8268.

6. Miller, K.L., et al., *Evidence for a vascular contribution to diffusion fMRI at high b value.* Proc. Natl. Acad. Sci., USA, 2007. **104**(52): p. 20967-20972.

7. Ransom, B.R., C.L. Yamate, and B.W. Connors, *Activity-dependent shrinkage of extracellular space in rat optic nerve: a developmental study.* J. Neurosci., 1985. **5**: p. 532-535.

8. Schwartzkroin, P.A., S.C. Baraban, and D.W. Hochman, *Osmolarity, ionic flux, and changes in brain excitability.* Epilepsy Res., 1998. **32**: p. 275-285.

9. Ransom, B.R. and H. Sontheimer, *The neurophysiology of glial cells.* J. Clin. Neurophys., 1992. **9**(2): p. 224-251.

10. Sykova, E. and A. Chvatal, *Extracellular ionic and volume changes: the role in glia-neuron interactions.* J. Chem. Neuroanat., 1993. **6**: p. 247-260.

11. Rash, J.E., *Molecular disruptions of the panglial syncytium block potassium siphoning and axonal saltatory conduction: pertinence to neuromyelitis optica and other demyelinating diseases of the central nervous system.* Neuroscience, 2010. **168**: p. 982-1008.

12. Prusky, G.T., et al., *Rapid Quantification of Adult and Developing Mouse Spatial Vision Using a Virtual Optomotor System.* Invest. Ophthal. Vis. Sci., 2004. **45**(12): p. 4611-4616.

13. Adamczak, J.M., et al., *High field BOLD response to forepaw stimulation in the mouse.* Neuroimage, 2010. **51**: p. 704-712.

14. Garbow, J.R., C. McIntosh, and M.S. Conradi, *Actively decoupled transmit-receive coil-pair for mouse brain MRI.* Conc. Magn. Reson. Pt B: Magn. Reson. Eng., 2008. **33B**(4): p. 252-259.

15. Tu, T.W., et al., *Using absorption-mode images to improve in vivo DTI quality.* Proc. Intl. Soc. Magn. Reson. Med. , 2010. **18**: p. 4001.

16. Lee, K., et al., *Relationships among Visual Cycle Retinoids, Rhodopsin Phosphorylation, and Phototransduction in Mouse Eyes During Light and Dark Adaptation.* Biochemistry, 2010. **49**: p. 2454-2463.

17. Ridder III, W.H. and S. Nusinowitz, *The visual evoked potential in the mouse—Origins and response characteristics.* Vision Res., 2006. **46**(6-7): p. 902-913.

18. May, C.A. and E. Lutjen-Drecoll, *Morphology of the murine optic nerve.* Invest. Ophthal. Vis. Sci., 2002. **43**(7): p. 2206-2212.

19. Basser, P.J., *Inferring microstructural features and the physiological state of tissues from diffusion-weighted images.* NMR in Biomed., 1995. **8**(7-8): p. 333-344.

20. Anderson, A.W., et al., *Effects of osmotically driven cell volume changes on diffusion-weighted imaging of the rat optic nerve.* Magn. Reson. Med., 1996. **35**: p. 162-167.

21. Szabo, K., et al., *Diffusion-weighted and perfusion MRI demonstrates parenchymal changes in complex partial status epilepticus.* Brain, 2005. **128**: p. 1369-1376.

22. Zhong, J., et al., *Reversible, reproducible reduction of brain water apparent diffusion coefficient by cortical electroshocks.* Magn. Reson. Med., 1997. **37**: p. 1-6.

23. Latour, L.L., et al., *Spreading waves of decreased diffusion coefficient after cortical stimulation in the rat brain.* Magn. Reson. Med., 1994. **32**: p. 189-198.

24. Sotak, C.H., *New NMR measurements in epilepsy: diffusion-weighted magnetic resonance imaging of spreading depression.* Adv. Neurol., 1999. **79**: p. 925-929.

25. Hartline, H.K., *Intensity and duration in the excitation of single photoreceptor units.* J. Cell. Comp. Physiol., 1934. **5**: p. 229-247.

26. Rothe, T., et al., *Repetitive firing deficits and reduced sodium current density in retinal ganglion cells developing in the absence of BDNF.* J. Neurobiol., 1999. **40**: p. 407-419.

27. Nakamura, T.J., S. Ebihara, and K. Shinohara, *Reduced light response of neuronal firing activity in the suprachiasmatic nucleus and optic nerve of cryptochrome-deficient mice.* PLoS One, 2011. **6**: p. e28726.

28. Gulani, V., G.A. Iwamoto, and P.C. Lauterbur, *Apparent Water Diffusion Measurements in Electrically Stimulated Neural Tissue.* Magn. Reson. Med., 1999. **41**: p. 241-246.

29. Mandl, R.C.W., et al., *Functional diffusion tensor imaging: measuring task-related anisotropy changes in the human brain along white matter tracts.* PLoS One, 2008. **3**(11): p. e3631.

30. Does, M.D., J. Zhong, and J.C. Gore, *In Vivo measurement of ADC change due to intravascular susceptibility variation.* Magn. Reson. Med., 1999. **41**: p. 236-240.

31. Zhong, J., R.P. Kennan, and J.C. Gore, *Effects of susceptibility variations on NMR measurements of diffusion.* J. Magn. Reson., 1991. **95**: p. 267-280.

32. Walz, W., *Role of glial cells in the regulation of the brain ion microenvironment.* Prog. Neurobiol., 1989. **33**: p. 309-333.

33. Fifkova, E. and A. van Harreveld, *Long-lasting morphological changes in dendritic spines of dentate granular cells following stimulation of the entorhinal area.* J. Neurocytol., 1977. **6**: p. 211-230.

34. Tasaki, I. and P.M. Byrne, *Rapid structural changes in nerve fibers evoked by electric current pulses.* Biochem. Biophys. Res. Commun., 1992. **188**(2): p. 559-564.

35. Sen, P.N. and P.J. Basser, *A model for diffusion in white matter in the brain.* Biophys. J., 2005. **89**: p. 2927-2938.

36. Waxman, S.G., et al., eds. *Myelin Biology and Disorders*. Vol. 1. 2004, Elsevier Academic Press.

Chapter 5

Diffusion fMRI detects white-matter dysfunction in mice with acute optic neuritis

This chapter represents the latest version of a manuscript that is targeted for submission to NeuroImage.

(Tsen-Hsuan Lin, William M. Spees, Kathryn Trinkaus, Chia-Wen Chiang, Anne H. Cross, and Sheng-Kwei Song)

Abstract

Optic neuritis is a frequent first sign of multiple sclerosis (MS). Conventional magnetic resonance (MR) techniques provide a means to assess multiple MS-related pathologies, including axonal injury, demyelination, and inflammation. However, a method to directly and non-invasively probe white-matter function could further elucidate the interplay of pathology and dysfunction. Previously, we demonstrated a significant 27% activation-associated decrease in the apparent diffusion coefficient of water perpendicular to the axonal fibers ($ADC_{\perp}$) in normal C57BL/6 mouse optic nerve with visual stimulation using diffusion fMRI. Here we extend this approach to explore the relationship between visual acuity, pathology, and diffusion fMRI in the experimental autoimmune encephalomyelitis (EAE) mouse model of optic neuritis. Visual stimulation produced a significant 25% decreased in $ADC_{\perp}$ in EAE sham optic nerves, while only a 7% $ADC_{\perp}$ decrease was seen in acute-stage EAE mice. The reduced $ADC_{\perp}$ response was

consistent with impaired visual function in EAE eyes. Immunohistochemistry (IHC) data confirmed pathologies of EAE optic nerves including axonal injury, demyelination, and inflammation. These pathologies contributed impaired visual function and presumably produce the resulting reduced activation-associated $ADC_{\perp}$ response. Diffusion fMRI holds promise for directly gauging *in vivo* white-matter dysfunction.

5.1 INTRODUCTION

Multiple sclerosis (MS) is an inflammatory and neurodegenerative disease that mainly affects the central nerve system (CNS), such as brain, optic nerve, and spinal cord [1-3]. Optic neuritis is an inflammatory disorder of optic nerve and a frequent first sign of MS, which produces blurred vision and/or pain in the affected eye due to inflammation and demyelination at foci within optic nerve. The ten- and fifteen-year risk of developing clinically MS following a single episode of optic neuritis was 38% and 50%, respectively [4, 5]. Hence, investigating and treatment of optic neuritis might be crucial to reduce later development of MS and long-term disability due to the significant relationship between MS and optic neuritis [6]. Therefore, investigating functional deficits of optic neuritis may prevent or improve MS. Experimental autoimmune encephalomyelitis (EAE), which is induced by inoculation with myelin oligodendrocyte glycoprotein (MOG) peptide, is an animal model of human MS. Many pathological features in EAE models parallel those characteristic of MS, including demyelinating autoantibody response, axonal injury and loss, infiltration of encephalitogenic T cells and macrophages, activation of microglia, microphages and astrocytes [7-10].

Non-invasive MR measurement has been widely used to investigate or diagnose pathologies in EAE animal models and MS patients [11, 10, 12, 13, 2]. For instance, the apparent diffusion coefficient (ADC), axial and radial diffusivity, mean diffusivity (MD), and fractional anisotropy (FA) derived from diffusion-weighted images (DWI) or diffusion-tensor images (DTI) can be used to identify axonal injury, demyelination, inflammation, and axonal loss [14, 7, 15-17]. T1- and T2- weighted hypointensities result from higher cellularity and T2-weighted hyperintensities reflect vasogenic edema, demylination, and axonal loss. Also, T1-weighted contrast-enhanced images using Gd-DTPA or Mn^{2+} are indicative of compromised blood-brain

barrier (BBB) or inflammation in EAE models and MS, which results in vasogenic edema [18-22]. More accurate and novel approaches have recently been introduced to distinguish coexisting pathologies, including neuroinflammation, axonal injury or pathologieas in gray matter using diffusion basis spectrum image (DBSI) or diffusion kurtosis image (DKI) [23-26].

In addition, functional deficits are highly associated with or prior to aforementioned morphologies. MRI, also indeed, holds potential to reveal functional integrity. For instance, blood oxygen level dependent (BOLD) fMRI has been applied to study brain plasticity and cortical activation in MS patients [27-30] to reflect motor or visual functional deficits. Since conventional BOLD fMRI relies on local modulation of tissue blood volume and blood flow, secondary to neuronal activation and metabolic demand, it is an approach which is largely limited to cortical and gray-matter regions [31, 32] and mainly reflects post-synapse potential in cortical region [33, 34]. In addition to post-synapse potential, action potential, the visual signal propagation in CNS, should be considered as well to understand and assess functional deficits because optic neuritis is prominently affected in optic nerve tracts.

Recently, diffusion fMRI has been introduced and suggested as an alternative approach to identify neuronal and axonal functional integrity directly [35-40] Especially for white matter tracts, diffusion fMRI offers a promising means to assess axonal function, since our previous report showed a significant 27% $ADC_{\perp}$ decrease was observed during visual stimulation in healthy mouse optic nerves. Activation-associated $ADC_{\perp}$ decreases in optic nerves were independent of any vascular contribution [36].

White-matter tracts are prominently affected in MS, leading to various level of neurological disability. It is estimated that ~ 66% of MS patients will experience an episode of

optic neuritis at some point during the course of the disease (National MS Society, www.nationalmssociety.org). A direct and non-invasive assessment of axonal function in optic nerves would be crucial in understanding the MS pathophysiology and evaluating therapeutic outcomes. In this study, diffusion fMRI was performed to investigate *in vivo* axon-function deficits in EAE optic nerves.

5.2 Materials and Methods

All experimental procedures involving animals were approved by Washington University's Animal Studies Committee and conformed to the NIH Policy on Responsibility for Care and Use of Animals.

5.2.1 Experimental autoimmune encephalomyelitis (EAE) mouse model

Fourteen 7-week-old, female C57BL/6 mice were obtained from Jackson Laboratory (Bar Harbor, ME). Before immunization, mice were housed with 12-hour dark/light cycle for a week. Mice were randomly separated into two groups: seven in the EAE group and seven in the sham group. The mice in the EAE group were immunized with 50 μg MOG_{35-55} peptide emulsified (1:1) in incomplete Freund's adjuvant (IFA) and Mycobacterium tuberculosis. Pertussis toxin (300 ng; PTX, List Laboratories, Campbell, CA) was injected intravenously on the day of MOG_{35-55} immunization and two days later. The mice in the control group underwent the same procedure with only IFA without MOG_{35-55} immunization.

5.2.2 Visual Acuity (VA)

Mouse visual acuity was assessed using the Virtual Optometry System (Optomotry, Cerebral Mechanics, Inc., Canada). Briefly, the virtual rotating columns were projected on the LCD monitors with different spatial frequencies in cycles/degree (c/d). The mouse head movement in response to the virtual column rotations was noted. The spatial frequency was changed starting from 0.1 c/d with step size of 0.05 c/d until the mouse stopped responding. The VA was defined as the highest spatial frequency the mouse was able to respond to the virtual rotating columns. Prior to assignment of mice to EAE or experimental groups, all animals were checked to ensure that their visual acuity was within the accepted normal range, 0.37 ± 0.02 cycles/degree (mean ± S.D.), which was similar to our previous report, 0.38 ± 0.003 c/d [23]. After immunization, VA was assessed daily in all mice. For animals in the EAE group, VA $\leq$ 0.25 c/d (typically 8 – 13 days post-immunization) was defined as the onset of acute optic neuritis [23]. For EAE animals, diffusion fMRI measurements were performed on the first day at which their visual acuity was observed to be below 0.25 c/d. The mice in sham group did not develop visual impairment, but underwent the diffusion fMRI procedure within the same time range (8 – 13 days post-immunization)

5.2.3 Animal anesthesia and set-up

For initial setup mice were anesthetized with 1.5% isofluorane in O_2. Anesthetized mice were placed in a custom-made stereotactic head holder. The animal's experimental eye remained open and the contralateral eye was covered with parafilm and two layers of black electrical tape. After careful setup the mouse and head holder were placed in the imaging cradle. Respiratory rate and body temperature were monitored during experiments using an MR-compatible animal-monitoring system (SA Instrument, Inc., Stony Brook, NY). The body temperature was maintained at 37 ± 0.5 ºC via a regulated circulating warm water pad underneath the mouse body

and regulated warm air blown into the magnet bore. When mouse respiration was stable, a subcutaneous 0.3 mg/kg bolus of medetomidine was administered followed immediately by a continuous infusion of medetomidine at a rate of 0.6 mg/kg·hr through an in-dwelling subcutaneous catheter. Isoflurane in the breathing-gas mixture was gradually discontinued according to previously-described protocols until the animals were breathing room air [41].

5.2.4 Diffusion-weighted Image (DWI) protocol

MRI experiments were performed on a 4.7-T Agilent DirectDrive™ small-animal MRI system (Agilent Technologies, Santa Clara, CA) equipped with a Magnex/Agilent HD imaging gradient coil (Magnex/Agilent, Oxford, UK) capable of pulsed-gradient strengths of up to 58 G/cm and a gradient rise time ≤ 295 μs. An actively-decoupled 1.7-cm receive coil [42] was placed on the top of the mouse head for MR signal reception. Then, the animal holder assembly, including the receive coil was placed inside an 8-cm actively-decoupled volume transmit coil.

DWI measurements were carried out as previously described [36]. In brief, a multi-echo spin-echo diffusion-weighted imaging sequence [43] was employed with following parameters: TR = 1.5 s, TE = 37.1 ms, inter-echo delay = 23.6 ms, FOV = 20 × 20 mm^2, matrix size = 256 × 256 (zero-filled to 512 × 512), slice thickness = 1.3 mm. To get the final target image plane and minimize partial volume effects, three middle-sagittal DWI images (diffusion gradient applied in the slice-select direction) were acquired based on image planning derived from axial T2-weighted images. The middle slice of the three sagittal DWI images clearly showed the orientation of the pair of optic nerves, and the final image plane was adjusted carefully based upon this middle sagittal DWI. The final targeted image slice plane was orthogonal to the optic nerves to minimize partial volume effects. Two diffusion-sensitizing factors (b values), 0.1 and

1.4 ms/μm^2 (with δ = 5 ms and Δ = 18 ms), were applied to generate two DWIs (Fig. 5 – 1A and 5 – 1B). A train of three echoes were co-added to form the final MR images to increase accumulated signal-to-noise ratio.

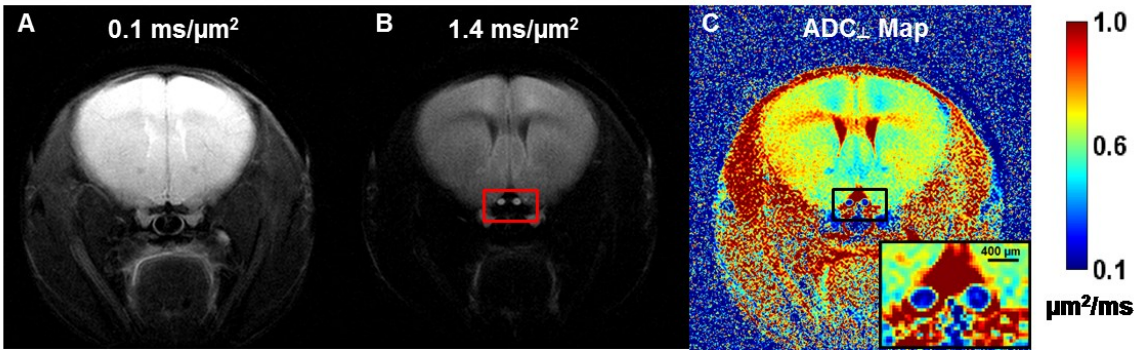

Figure 5 – 1 Two diffusion-weighted images (DWI) with diffusion-sensitizing gradients applied in the phase-encoding direction (left-to-right) with b values of 0.1 ms/μm^2 (A) and 1.4 (B) ms/μm^2 were used to generate the resulting $ADC_{\perp}$ map (C). The red box in panel B highlights the location of optic nerves (bright) and surrounding cerebrospinal, which is highly suppressed.$ADC_{\perp}$ values in the optic nerves are considerably lower than that in other brain tissues. The regular (nearly circular) shape of the optic nerves suggests good orthogonality between the nerve axes and the slice plane, which minimizes partial volume effects.

5.2.5 Visual stimulation

Visual stimulation was delivered by a flashing white LED (Cree, Model C503C-WAS) placed 5 cm in front of mouse nose. A step-function signal of 1.4 Hz frequency with 200 ms on/514 ms off and 4 V/0 V (on/off) was provided during stimulation. The detail of equipment set-up was the same as that reported previously [36].

5.2.6 Diffusion fMRI strategy

For each mouse, three pairs of diffusion-weighted images were acquired. The first pair of images without visual stimulation was taken as a baseline. Then, the stimulus-on DWI dataset was acquired during application of flashing-light stimulation. Finally, the LED light was turned off for the post-stimulus DWI acquisition.

5.2.7 DWI Data analysis

For measurements of diffusion perpendicular to the axonal fibers, signal decay with b-value between 0.1 and 1.4 ms/μm^2 is monexponential [36]. $ADC_{\perp}$ maps were generated from the pair of DWIs according to equation of Skejskal and Tanner [44] with code developed in-house and written in MATLAB (Mathworks, Natick, MA). Optic nerve ROIs were drawn based on operator-independent criteria as described previously [36].

5.2.8 Immunohistochemistry (IHC) staining in optic nerves

Following MR experiments, mice were perfused with 1 % phosphate-buffer saline (PBS) followed by 4 % paraformaldehyde in 1 % PBS. The brain was excised and post-fixed in fixative for 24 hours then transferred to 1 % PBS for storage at 4˚C until histological analysis. Mouse optic nerves were embedded in 2 % agar blocks [45]. Then, the agar block was embedded in

paraffin wax and 5-µm thick transverse slices were sectioned for IHC staining. Sections were deparaffinized, rehydrated, and then blocked using 1 % bovine serum albumin (BSA, Sigma Inc., MO, US) and 5 % normal goat-serum solution for 20 minutes at room temperature to prevent non-specific binding and to increase antibody permeability. Slides were incubated overnight at 4˚C with monoclonal anti-phosphorylated neurofilament antibody (SMI-31; 1:1000, Covance, U.S.) to stain non-injured axons or rabbit anti-myelin basic protein (MBP) antibody (1:1000, Sigma Inc., MO, U.S.) to stain myelin sheaths [46-48]. After rinsing, goat anti-mouse IgG or goat anti-rabbit IgG conjugated Alexa 488 (1:800) were applied to visualize immunoreactivity of phosphorylated neurofilament and MBP. Finally, slides were covered using Vectashield Mounting Medium with 4',6-diamidino-2-phenylindole (DAPI, Vector Laboratory, Inc., Burlingame, CA) to stain cell nuclei as well [48, 24]. Histological slides were examined with a Nikon Eclipse 80i fluorescence microscope equipped with 60× water objective, and images were captured with a black-and-white CCD camera with MetaMorph software (Universal Imageing Corporation, Sunnyvale, CA) from the center of optic nerve. The 60× IHC staining images (0.018 mm^2) covered ~40% area of whole optic nerves (0.045 ± 0.013 mm^2, mean ± S.D.). Histological counts are reported for 7 EAE and 6 sham optic nerves in this study.

5.2.9 Histological data analysis

The whole field of SMI-31, MBP, and DAPI staining images at 60× magnification were captured with the same fluorescence light intensity and exposure time. All captured images were converted to 8- bit gray scale and analyzed using threshold, analyze particles and gray level watershed segmentation functions in ImageJ (http://bigwww.epfl.ch/sage/soft/watershed/).

Positive DAPI staining represented cell nuclei, and larger spots were shown in staining images. DAPI-stained regions showed obvious contrast to the background, thus the quantified number was directly calculated after applying the signal threshold.

5.2.10 Statistical analysis

The p-values of $ADC_{\perp}$ change between first off (baseline) and stimulus on came from a cluster linear repeated measures model, which took into account that there were three time points for each eye and two eyes per mouse. The p-values of visual function (VA), SMI-31, MBP, and DAPI were from nonparametric test for difference between sham and EAE groups and adjusted using Wilcoxon Two-Sample Test. The correlation coefficients for VA with each of SMI-31, MBP, DAPI, and decreased $ADC_{\perp}$ were analyzed by Spearman's rank correlation coefficient.

5.3 Results

5.3.1 Impairment of visual function and reduced activation-associated ADC⊥ response in EAE optic nerves

Visual acuity (VA) of EAE and sham animals was assessed daily. Our previous report mentioned that normal VA of C57BL/6 mouse was 0.38 ± 0.03 c/d (mean ± S.D., n=30). The operational definition of onset acute optic neuritis was VA ≤ 0.25 c/d [23]. Before immunization, normal VA was confirmed for each eye (n = 28, VA = 0.37 ± 0.02 c/d) to exclude mice with poor vision due to uncontrollable factors. For the EAE mice in this study, the first time point at which VA ≤ 0.25 c/d was observed, the operational definition of onset acute optic neuritis in this animal model,was between day 8 – 13 post-immunization. Affected mice developed unilateral

visual impairment. Group-averaged visual acuities of the EAE, sham and blocked eyes (n= 7, 7, and 14, respectively) were 0.15 ± 0.08, 0.36 ± 0.02, and 0.36 ± 0.03 c/d (mean ± S.D., Fig. 5 – 2A). VA of EAE eyes showed a significant 58% ($p < 0.005$, EAE vs. sham) decrease at the acute-stage time point when diffusion fMRI was performed.

$ADC_{\perp}$ maps were generated from the diffusion-weighted image data (Fig. 1). The group-averaged baseline optic-nerve $ADC_{\perp}$ of affected acute-stage EAE optic neuritis eyes was higher than in sham eyes (Fig. 5 – 2B and 5 – 2C, Table 5 – 1) Compared to their own baseline $ADC_{\perp}$ measurements, EAE and sham eyes showed a slight 7% ($p = 0.45$) and significant 25% ($p < 0.005$) $ADC_{\perp}$ decrease during visual stimulus, respectively. No $ADC_{\perp}$ changes were observed between baseline and visual stimulus in the contralateral blocked eyes of EAE ($p = 0.91$) and sham ($p = 0.97$) mice (Fig. 5 – 2B and 5 – 2C, Table 5 – 1) during applied visual stimulation. These results imply that the activation-associated $ADC_{\perp}$ decreases in EAE and sham optic nerves are elicited by axonal activation. The EAE eyes exhibited impaired visual acuity and correspondingly reduced $ADC_{\perp}$ response with visual stimulation.

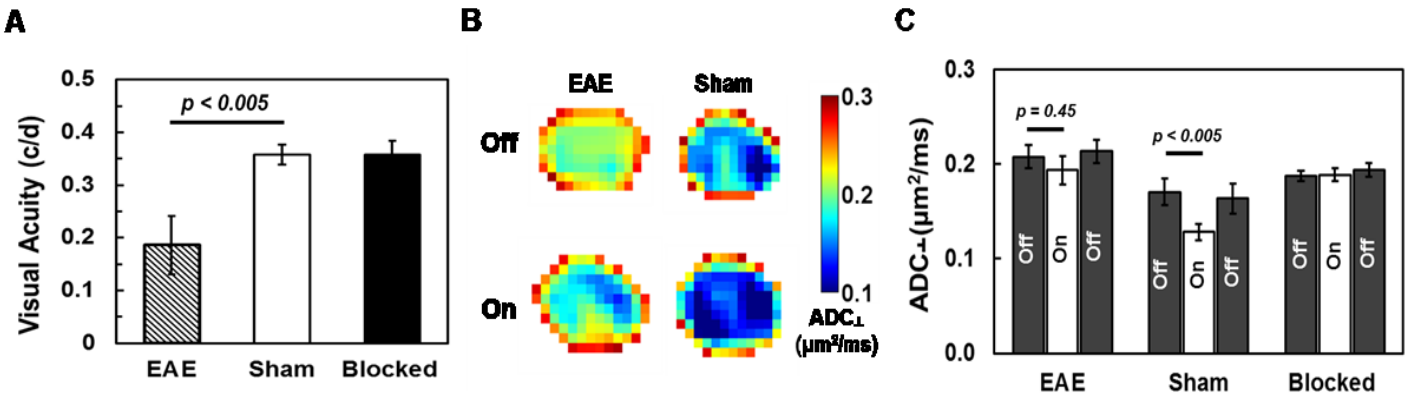

Figure 5 – 2 In this mouse model of EAE optic neuritis, visual deficits typically developed in only one eye. **(A)** Group-averaged visual acuity was significantly decreased by 58% ($p < 0.005$, vs. sham, mean ± S.D.) in affected EAE eyes (n=7) compared with the normal vision of sham eyes (n=7). Error bars indicate standard deviation. Also shown in A is the visual acuity of contralateral blocked (n=14) eyes, which were used as a diffusion fMRI internal control for each animal. **(B)** Group $ADC_{\perp}$ maps were generated by averaging stacked $ADC_{\perp}$ maps from EAE (n=7) and sham (n=7) optic nerves, respectively (B). The baseline $ADC_{\perp}$ of EAE optic nerves (panel B and C) was higher than sham group due to demyelinated vasogenic edema in acute stage (cf. Figure 3). Activation-associated $ADC_{\perp}$ decrease was observed in both EAE and sham optic nerves (B and C). **(C)** When compared to its own baseline, $ADC_{\perp}$ significantly decreased in sham optic nerves (25%, $p < 0.005$, B, C, and Table 1) with visual stimulation. In contrast, only a slight $ADC_{\perp}$ decrease was observed in EAE optic nerves (7%, $p = 0.45$, B, C and, Table 1). The optic nerves of blocked eyes showed no $ADC_{\perp}$ change with visual stimulation (C and Table 1), suggesting that the decreased $ADC_{\perp}$ in stimulated EAE and sham optic nerves was caused by axonal activity.

Table 5 – 1
Group averaged $ADC_{\perp}$ of baseline, stimulus on, and stimulus off of EAE (n=7), sham (n=7), blocked EAE and sham (n=14) eyes

	Baseline	Stimulus on	Stimulus off
EAE	0.200 ± 0.012	0.186 ± 0.015	0.207 ± 0.012
Sham	0.171 ± 0.014	0.128 ± 0.008	0.164 ± 0.016
Blocked	0.188 ± 0.006	0.189 ± 0.007	0.196 ± 0.007

$ADC_{\perp}$ ($\mu m^2/ms$): mean ± standard error of the mean
Blocked: contralateral EAE and sham eyes

5.3.2 Axonal impairment was assessed by immunohistochemistry (IHC) staining

Previously, immunohistochemical (IHC) staining of phosphorylated neurofilament (SMI-31, intact axon), myelin basic protein (MBP, myelin sheath), and 4',6- diamidino-2-phenylindole (DAPI, cell nuclei) have been shown to reflect white-matter integrity [46, 7, 24]. Representative zoom-in 60× images (56% of 60× image) from EAE (n=7) optic nerves demonstrated obviously axonal beading, low density of intact axons, less/thin myelin area, and higher cell nuclei density (Fig.5 – 3A, 5 – 3D, and 5 – 3G) than sham optic nerves (n = 6, one optic nerve specimen was damaged during tissue processing). Group-averaged counts of SMI-31, MBP, and DAPI (Fig. 5 – 3C, 5 – 3F, 5 – 3I and Table 5 – 2) in EAE optic neuritis onset showed a significant 22% [$p < 0.005$, 5.3 (± 0.6) × 10^5] decrease in density of intact axons and 17% [$p < 0.005$, 36.2 (± 2.5)] myelin sheath area decrease compared with sham group [6.8 (± 0.5) × 10^5 and 43.6 (± 2.), respectively] . Furthermore, the density of cell nuclei in EAE optic neuritis onset was increased by 38% [$p < 0.05$, 5.8 (± 1.2) × 10^3] compared with sham group [4.2 (± 0.5) × 10^3]. Based on IHC histological results, EAE optic nerves exhibited clear signs of axonal injury, demyelination, and inflammation.

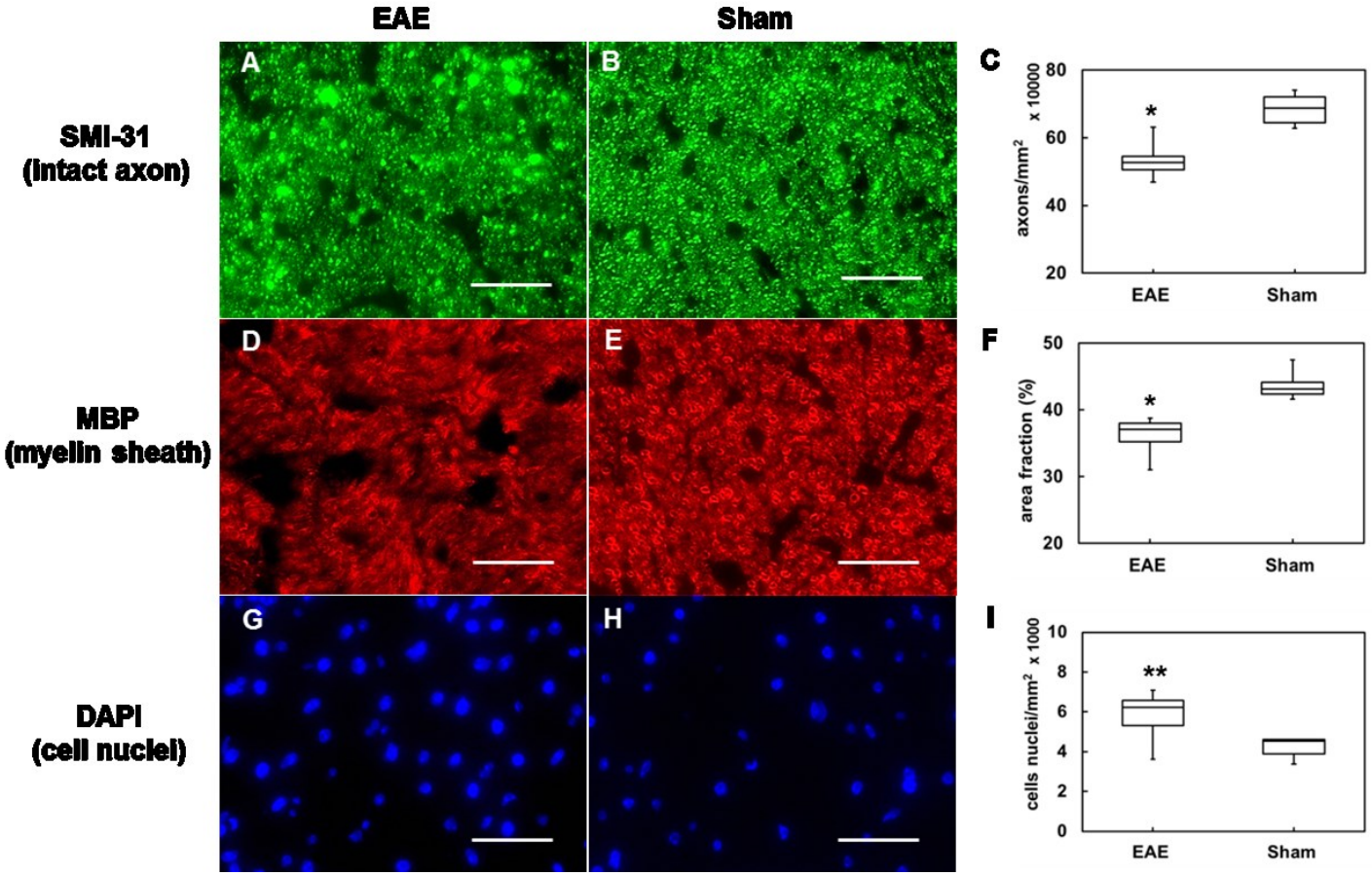

Figure 5 – 3 Representative 60× immunohistochemistry staining images of phosphorylated neurofilament (SMI-31, intact axon), myelin basic protein (MBP, myelin sheath), and 4', 6-dianidino-2-phenylindole (DAPI, nuclei) from EAE (A, D, and G,) and sham (B, E, and H) optic nerves. EAE optic nerves demonstrated obvious axonal beading, lower axonaldensity (A), reduced myelin area (D), and more cell nuclei (G). Group average IHC counts of EAE (n=7) and sham (n=6) optic nerves (Table 2) reveal significant SMI-31 (C) and MBP (F) decrease and significant DAPI (I) increase in the EAE group. IHC results suggest that axonal impairment, demyelination, and inflammatory infiltration all contribute to visual deficits in acute optic neuritis in this EAE mouse model.

Scale Bar: 25 μm

* indicates $p < 0.005$

** indicates $p < 0.05$

Table 5 – 2
Quantitative immunohistochemistry results of EAE (n=7) and sham (n=6) optic nerves

	SMI31 (#/mm^2)	MBP (area %)	DAPI (#/mm^2)
EAE (n=7)	532897 ± 58103	36.15 ± 2.50	5819 ± 1160
Sham (n=6)	684574 ± 46864	43.60 ± 2.11	4225 ± 545

Counts: mean ± standard deviation

5.3.3 Pathological trend and activation-associated $ADC_{\perp}$ reduction

Visual function (measured by VA) highly correlated with intact axon density (Fig. 5 – 4A, $r = 0.77$, $p = 0.0012$), myelin sheath area (Fig. 5 – 4B, $r = 0.92$, $p < 0.0001$), and cell nucleus density (Fig. 5 – 4C, $r = -0.73$, $p = 0.0029$) assessed by positive SMI-31, MBP, and DAPI stains. Our data suggested that impairment of optic nerve function resulting from axonal injury, demyelination, and inflammation contributed to decreased VA at the acute stage. The reduction of activation-associated $ADC_{\perp}$ decrease was consistent and correlated well with impaired visual function (Fig. 5 – 4D, $r = 0.76$, $p = 0.0015$) and suggested that diffusion fMRI provides a means to non-invasively assess axonal-activation and axonal dysfunction resulting from pathological changes in onset optic neuritis in this EAE mouse model.

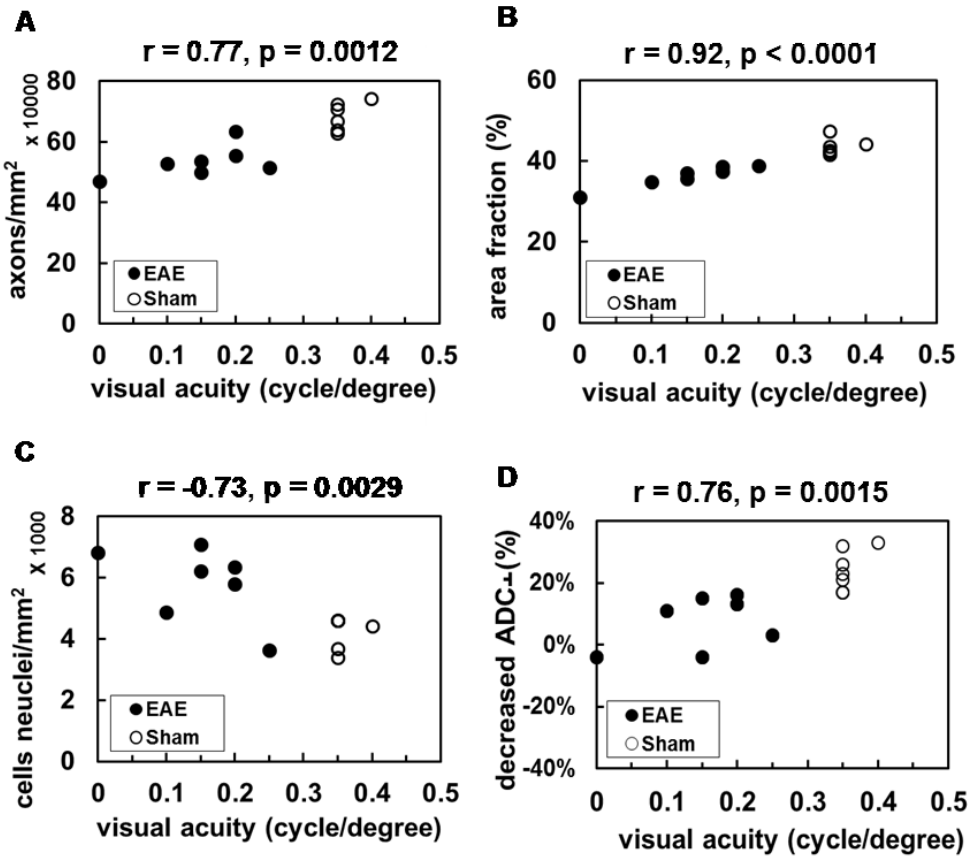

Figure 5 – 4 Pathological changes accompanying decreased visual acuity included reduced SMI-31 counts (A, intact axon) and MBP (B, myelin area) and increased DAPI counts (C, cell nuclei). The reduced activation-associated $ADC_{\perp}$ change (decrease in $ADC_{\perp}$ with stimulation expressed as a percentage of baseline $ADC_{\perp}$) accompanied lower visual acuity (D). This data suggests that axonal impairment and dysfunction can be assessed by diffusion fMRI.

5.4 Discussion

This is the first study applying diffusion fMRI to assess functional deficits of a white-matter tract *in vivo*. The results presented here demonstrate a slightly attenuated, 7%, neuronal-activation-associated $ADC_{\perp}$ decrease in EAE mice with onset optic neuritis compared to a significant, 25%, decrease in sham mice. The results for EAE sham mice are comparable to our previously-reported ~27% $ADC_{\perp}$ decrease in normal mouse optic nerves [36]. The attenuated activation-associated $ADC_{\perp}$ response in the current study is consistent with impaired visual function resulting from optic-nerve pathologies including axonal injury, demyelination, and inflammation.

Visual signal conduction through the optic nerve depends on repeated cycles of membrane depolarization/action potential/repolarization, which are accompanied by ion gradient changes [49].Unlike BOLD fMRI is largely limited to gray matter for post-synaptic potential [33, 34], diffusion fMRI reveals the effect of action potential propagation in white matter. Diffusion MRI would be expected to be sensitive extracellular space (ECS) shrinkage caused by transient ionic gradient changes, osmotic shifts of water across cell membranes, or glial cell swelling associated with changes in size and shape during axonal activation [50-56, 39, 57, 58]. In our previous study, the observed activation-associated 27% $ADC_{\perp}$ decrease was shown to be independent of a vascular-coupling contribution [36]. Diffusion fMRI has the potential to directly probe functional integrity in CNS axons without confounding blood-flow effects.

In this study, we measured VA by optokinetic response (OKR) for EAE and sham eyes to reflect visual function, since VA with different spatial frequency in C57BL/6 mice reflected the retinal efferent pathway to subcortical visual structures [59, 60]. Because psychophysical

measurement, i.e. OKR, is taken 70% correct level compared to electrophysiological measurement, i.e. VEP [61], VA by OKR measurement, therefore, reflects appropriately electrical signal propagation in mouse visual system. The VA of EAE eyes in this sample was significantly lower than in sham eyes (a 58% decrease, $p < 0.005$, Fig. 5 – 2A). The histological results showed that the EAE mice in this sample developed inflammation, demyelination, and axonal injury (Fig. 5 – 3C, 5 – 3F, and 5 – 3I), suggesting the pathologies of optic neuritis in EAE mice affected their visual function.

According to VEP measurement in mouse visual system, the optimal visual stimulation condition was determined [61] and applied to this study. During diffusion measurement with visual stimulation, decreased $ADC_{\perp}$ and unchanged $ADC_{\perp}$ were observed in unblocked and blocked eyes of sham mice, respectively (Fig. 5 – 2B and 5 – 2C) suggesting the $ADC_{\perp}$ directly revealed electrical/action potential in optic nerve. For the unblocked eyes, the $ADC_{\perp}$ change in EAE optic nerves was less than sham mice and revealed that the dysfunction of axonal activity. The results corresponded to lower VA and pathologies. The baseline of $ADC_{\perp}$ in EAE optic nerves may result from acutely demyelination or vasogenic edema since radial diffusivity or ADC increase reflected those two pathologies have been reported in EAE mice or MS patients [14, 7, 23, 19, 62, 63].

In CNS, compound action potential (CAP) propagation causes ion gradient change and needs large amount of ATP to maintain ion homeostasis and neurotransmission including about 60-80% and 10-20% ATP consumption, respectively [64]. Mitochondria are the major source of axonal ATP required to maintain CAP propagation by means of saltatory conduction [65]. At acute stage of MS patients and EAE animal models, lymphocytes cross BBB and attack myelin

in CNS [3]. Lymphocyte-induced inflammation activates microglial cells and macrophages and then induced more nitric oxide (NO), which also blocks saltatory conduction propagation and reduces mitochondrial function in CNS of MS patients and EAE animals [66-68]. Demyelination, which also leads to impaired saltatory conduction [69, 70], has been shown to result in, redistribution of and/or increases in voltage-gated Na^+ channel density in the membrane of demyelinated axons in order to maintain nerve conduction, and it leads to increased energy demands due to altered channel expression and demyelination [71, 70, 72]. Therefore, inhibition of mitochondrial due to NO production and increase of energy demand due to Na^+-channel redistribution might result in ion dyshomeostasis and energetic imbalance. Declining energetic status results in reduced Na^+/K^+ ATPase pump activity and, hence, increases intracellular Na^+ concentration. In such situations, Ca^{2+} influx via action of the Na^+/Ca^{2+} exchanger has been postulated to produce mitochondrial dysfunction, axonal damage, and ultimately necrosis [73, 74, 66, 71, 75]. Other mechanism such as the excessive glutamate production by inflammatory cells leads to glutamate-induced Ca^{2+} overload and inhibition of mitochondria, and it finally results in excitotoxicity of axons [76, 75, 77, 71]. Therefore, we speculate that the inflammation, demyelination, ion-dyshomeoastasis, and energetic imbalance in CNS of MS patients or EAE animals affect functional integrity and could be an early event.

Our histological results demonstrated that EAE optic nerves in this sample developed axonal injury, demyelination, and inflammation (Fig. 5 – 3); the pathologies were consistent with impaired visual function as well (Fig. 5 – 4A ~ 5 – 4C). The results were in agreement with aforementioned impaired visual signal propagation in MS patients or EAE animals. The change of decreased activation-associated $ADC_\perp$ response was consistent with impaired visual acuity (Fig. 5 – 4D). Therefore, this non-invasive in vivo functional measurement may offer a new

approach to directly reflect the axonal activity. Contributions from retinal dysfunction at the early time point measured herein are unlikely as previously retinal ganglion cell (RGC) pathological changes have been shown to occur later in the progression of optic neuritis [78, 79]. This is also consistent with our own RGC histological data (Chiang et al., unpublished).

Optic neuritis is frequently the first sign of MS in patients [4]. Inflammation and demyelination of the affected optic nerves produces impaired visual function (blurred vision or occasionally total blindness). In EAE animal models of MS, several groups demonstrated visual dysfunction accompanying optic neuritis via behavioral or visual evoke potential (VEP) measurements [80, 81, 8, 82]. These measurements rely upon functionality of the entire visual pathway including retina, optic nerve, visual cortex, and/or conscious response of the brain. Thus they may lack specificity in terms of demonstrating the location and contribution of specific lesion sites. Because $ADC_{\perp}$ of diffusion fMRI is a direct measurement of white-matter function, hence, we speculate that activation-associated $ADC_{\perp}$ decrease, which likely result from ECS shrinkage during axonal activation, in EAE optic nerves is less than sham mice during visual stimulation. Decreased $ADC_{\perp}$ change was observed in EAE optic nerves since they bear dysregulation of ion gradients and ion dyshomeostasis owing to mitochondrial failure and demyelination. That is, the EAE optic nerves with prolonged or impeded CAP propagation lose the abilities to modulate transient ion gradient change and osmotic shift of water across cell membranes.

To conclude, the attenuated activation-associated $ADC_{\perp}$ response at the onset of optic neuritis in this animal model likely reflects *in vivo* functional deficits at the optic-nerve axonal level. The impaired EAE optic nerves demonstrated an attenuated response compared to sham optic nerves

during application of the same stimulation protocol. The functional pathologies in EAE optic nerves using diffusion fMRI provide a unique perspective on the consequences of inflammatory demyelinating pathologies. *In vivo* diffusion fMRI is a promising tool for investigations of pathological mechanisms, therapeutic targets, and/or longitudinal assessment in white-matter tracts.

Acknowledgements

The authors thank Mr. Bob Mikesell for excellent technical assistance. This study was supported in part by the grants from National Institute of Health R01-NS047592 (S.-K.S.), P01-NS059560 (A.H.C.), and National Multiple Sclerosis Society (NMSS) RG 4549A4/1 (S.-K.S.).

5.5 Reference

1. Trapp, B.D. and K.A. Nave, *Multiple sclerosis: an immune or neurodegenerative disorder?* Annu Rev Neurosci, 2008. **31**: p. 247-69.

2. Filippi, M., et al., *Association between pathological and MRI findings in multiple sclerosis.* Lancet Neurol, 2012. **11**(4): p. 349-60.

3. Compston, A. and A. Coles, *Multiple sclerosis.* Lancet, 2008. **372**(9648): p. 1502-17.

4. Beck, R.W., et al., *High- and low-risk profiles for the development of multiple sclerosis within 10 years after optic neuritis: experience of the optic neuritis treatment trial.* Arch Ophthalmol, 2003. **121**(7): p. 944-9.

5. *Multiple sclerosis risk after optic neuritis: final optic neuritis treatment trial follow-up.* Arch Neurol, 2008. **65**(6): p. 727-32.

6. Arnold, A.C., *Evolving management of optic neuritis and multiple sclerosis.* Am J Ophthalmol, 2005. **139**(6): p. 1101-8.

7. Sun, S.W., et al., *Selective vulnerability of cerebral white matter in a murine model of multiple sclerosis detected using diffusion tensor imaging.* Neurobiol Dis, 2007. **28**(1): p. 30-8.

8. Diem, R., et al., *Autoimmune optic neuritis in the common marmoset monkey: comparison of visual evoked potentials with MRI and histopathology.* Invest Ophthalmol Vis Sci, 2008. **49**(8): p. 3707-14.

9. Gold, R., C. Linington, and H. Lassmann, *Understanding pathogenesis and therapy of multiple sclerosis via animal models: 70 years of merits and culprits in experimental autoimmune encephalomyelitis research.* Brain, 2006. **129**(Pt 8): p. 1953-71.

10. Emerson, M.R., et al., *Enhancing the ability of experimental autoimmune encephalomyelitis to serve as a more rigorous model of multiple sclerosis through refinement of the experimental design.* Comp Med, 2009. **59**(2): p. 112-28.

11. Ge, Y., *Multiple sclerosis: the role of MR imaging.* AJNR Am J Neuroradiol, 2006. **27**(6): p. 1165-76.

12. Inglese, M. and M. Bester, *Diffusion imaging in multiple sclerosis: research and clinical implications.* NMR Biomed, 2010. **23**(7): p. 865-72.

13. Filippi, M., *MRI-clinical correlations in the primary progressive course of MS: new insights into the disease pathophysiology from the application of magnetization transfer, diffusion tensor, and functional MRI.* J Neurol Sci, 2003. **206**(2): p. 157-64.

14. Song, S.K., et al., *Demyelination increases radial diffusivity in corpus callosum of mouse brain.* Neuroimage, 2005. **26**(1): p. 132-40.

15. Naismith, R.T., et al., *Radial diffusivity in remote optic neuritis discriminates visual outcomes.* Neurology, 2010. **74**(21): p. 1702-10.

16. Roosendaal, S.D., et al., *Regional DTI differences in multiple sclerosis patients.* Neuroimage, 2009. **44**(4): p. 1397-403.

17. Wu, Q., et al., *MR diffusion changes correlate with ultra-structurally defined axonal degeneration in murine optic nerve.* Neuroimage, 2007. **37**(4): p. 1138-47.

18. Broom, K.A., et al., *MRI reveals that early changes in cerebral blood volume precede blood-brain barrier breakdown and overt pathology in MS-like lesions in rat brain.* J Cereb Blood Flow Metab, 2005. **25**(2): p. 204-16.

19. Boretius, S., et al., *MRI of optic neuritis in a rat model.* Neuroimage, 2008. **41**(2): p. 323-34.

20. Filippi, M., et al., *Comparison of triple dose versus standard dose gadolinium-DTPA for detection of MRI enhancing lesions in patients with primary progressive multiple sclerosis.* J Neurol Neurosurg Psychiatry, 1995. **59**(5): p. 540-4.

21. Nessler, S., et al., *Early MRI changes in a mouse model of multiple sclerosis are predictive of severe inflammatory tissue damage.* Brain, 2007. **130**(Pt 8): p. 2186-98.

22. Bruck, W., et al., *Inflammatory central nervous system demyelination: correlation of magnetic resonance imaging findings with lesion pathology.* Ann Neurol, 1997. **42**(5): p. 783-93.

23. Chiang, C.W., et al., *Acute visual function impairment in EAE is primarily caused by optic nerve inflammation as assessed by DBSI.* Proc. Intl. Soc. Mag. Reson. Med. 20, 3058, 2012.

24. Wang, Y., et al., *Quantification of increased cellularity during inflammatory demyelination.* Brain, 2011. **134**(Pt 12): p. 3590-601.

25. Tu, T.W., et al., *Diffusion Basis Spectrum Imaging detects evolving axonal injury, demyelination, and inflammation in the course of EAE.* Proc. Intl. Soc. Mag. Reson. Med. 20, 3598, 2012.

26. Raz, E., et al., *A Better Characterization of Spinal Cord Damage in Multiple Sclerosis: A Diffusional Kurtosis Imaging Study.* AJNR Am J Neuroradiol, 2013.

27. Rocca, M.A., M. Absinta, and M. Filippi, *The role of advanced magnetic resonance imaging techniques in primary progressive MS.* J Neurol, 2012. **259**(4): p. 611-21.

28. Rocca, M.A., et al., *Large-scale neuronal network dysfunction in relapsing-remitting multiple sclerosis.* Neurology, 2012. **79**(14): p. 1449-57.

29. Gallo, A., et al., *Visual resting-state network in relapsing-remitting MS with and without previous optic neuritis.* Neurology, 2012. **79**(14): p. 1458-65.

30. Staffen, W., et al., *Cognitive function and fMRI in patients with multiple sclerosis: evidence for compensatory cortical activation during an attention task.* Brain, 2002. **125**(Pt 6): p. 1275-82.

31. Heeger, D.J. and D. Ress, *What does fMRI tell us about neuronal activity?* Nat Rev Neurosci, 2002. **3**(2): p. 142-51.

32. Logothetis, N.K., *What we can do and what we cannot do with fMRI.* Nature, 2008. **453**(7197): p. 869-878.

33. Logothetis, N.K., et al., *Neurophysiological investigation of the basis of the fMRI signal.* Nature, 2001. **412**(6843): p. 150-7.

34. Gawryluk, J.R., et al., *Optimizing the detection of white matter fMRI using asymmetric spin echo spiral.* Neuroimage, 2009. **45**(1): p. 83-8.

35. Le Bihan, D., et al., *Direct and fast detection of neuronal activation in the human brain with diffusion MRI.* Proc Natl Acad Sci U S A, 2006. **103**(21): p. 8263-8.

36. Spees, W.M., T.H. Lin, and S.K. Song, *White-matter diffusion fMRI of mouse optic nerve.* Neuroimage, 2013. **65**: p. 209-15.

37. Tsurugizawa, T., et al., *Diffusion fMRI can detect neural activation when the BOLD fMRI response is abolished by nitroprussiate.* Proc. Intl. Soc. Mag. Reson. Med. 21, 0416, 2013.

38. Darquie, A., et al., *Transient decrease in water diffusion observed in human occipital cortex during visual stimulation.* Proc Natl Acad Sci U S A, 2001. **98**(16): p. 9391-5.

39. Flint, J., et al., *Diffusion weighted magnetic resonance imaging of neuronal activity in the hippocampal slice model.* Neuroimage, 2009. **46**(2): p. 411-8.

40. Le Bihan, D., *Diffusion, confusion and functional MRI.* Neuroimage, 2012. **62**(2): p. 1131-6.

41. Adamczak, J.M., et al., *High field BOLD response to forepaw stimulation in the mouse.* Neuroimage, 2010. **51**(2): p. 704-12.

42. Garbow, J.R., C. McIntosh, and M.S. Conradi, *Actively decoupled transmit–receive coil-pair for mouse brain MRI.* Concepts in Magnetic Resonance Part B: Magnetic Resonance Engineering, 2008. **33B**(4): p. 252-259.

43. Tu, T.W., et al., *Using absorption-mode images to improve in vivo DTI quality.* Proc. Intl. Soc. Mag. Reson. Med. 18, 4001, 2010.

44. Stejskal, E.O. and J.E. Tanner, *Spin Diffusion Measurements: Spin Echoes in the Presence of a Time-Dependent Field Gradient.* The Journal of Chemical Physics, 1965. **42**(1): p. 288-292.

45. Blewitt, E.S., T. Pogmore, and I.C. Talbot, *Double embedding in agar/paraffin wax as an aid to orientation of mucosal biopsies.* J Clin Pathol, 1982. **35**(3): p. 365.

46. Song, S.K., et al., *Diffusion tensor imaging detects and differentiates axon and myelin degeneration in mouse optic nerve after retinal ischemia.* Neuroimage, 2003. **20**(3): p. 1714-22.

47. Sun, S.W., et al., *Evolving Wallerian degeneration after transient retinal ischemia in mice characterized by diffusion tensor imaging.* Neuroimage, 2008. **40**(1): p. 1-10.

48. Budde, M.D., et al., *Axial diffusivity is the primary correlate of axonal injury in the experimental autoimmune encephalomyelitis spinal cord: a quantitative pixelwise analysis.* J Neurosci, 2009. **29**(9): p. 2805-13.

49. Nicholls, J.G., S.W. Kuffler, and M.A. Robert, *From neuron to brain*. 4th ed. Vol. 2001. 2001, Sunderland, Mass.: Sinauer Associates. 1-23.

50. Holthoff, K. and O.W. Witte, *Intrinsic optical signals in rat neocortical slices measured with near-infrared dark-field microscopy reveal changes in extracellular space.* J Neurosci, 1996. **16**(8): p. 2740-9.

51. Ransom, B.R. and R.K. Orkand, *Glial-neuronal interactions in non-synaptic areas of the brain: studies in the optic nerve.* Trends Neurosci, 1996. **19**(8): p. 352-8.

52. Bay, V. and A.M. Butt, *Relationship between glial potassium regulation and axon excitability: a role for glial Kir4.1 channels.* Glia, 2012. **60**(4): p. 651-60.

53. Kole, M.H., et al., *Action potential generation requires a high sodium channel density in the axon initial segment.* Nat Neurosci, 2008. **11**(2): p. 178-86.

54. Waxman, S.G., *Conduction in myelinated, unmyelinated, and demyelinated fibers.* Arch Neurol, 1977. **34**(10): p. 585-9.

55. Schwartzkroin, P.A., S.C. Baraban, and D.W. Hochman, *Osmolarity, ionic flux, and changes in brain excitability.* Epilepsy Res, 1998. **32**(1-2): p. 275-85.

56. Ransom, B.R., C.L. Yamate, and B.W. Connors, *Activity-dependent shrinkage of extracellular space in rat optic nerve: a developmental study.* J Neurosci, 1985. **5**(2): p. 532-5.

57. Le Bihan, D. and H. Johansen-Berg, *Diffusion MRI at 25: exploring brain tissue structure and function.* Neuroimage, 2012. **61**(2): p. 324-41.

58. Le Bihan, D., *The 'wet mind': water and functional neuroimaging.* Phys Med Biol, 2007. **52**(7): p. R57-90.

59. Douglas, R.M., et al., *Independent visual threshold measurements in the two eyes of freely moving rats and mice using a virtual-reality optokinetic system.* Vis Neurosci, 2005. **22**(5): p. 677-84.

60. Prusky, G.T., et al., *Rapid quantification of adult and developing mouse spatial vision using a virtual optomotor system.* Invest Ophthalmol Vis Sci, 2004. **45**(12): p. 4611-6.

61. Ridder, W.H., 3rd and S. Nusinowitz, *The visual evoked potential in the mouse--origins and response characteristics.* Vision Res, 2006. **46**(6-7): p. 902-13.

62. Castriota-Scanderbeg, A., et al., *Diffusion of water in large demyelinating lesions: a follow-up study.* Neuroradiology, 2002. **44**(9): p. 764-7.

63. Hickman, S.J., et al., *A serial MRI study following optic nerve mean area in acute optic neuritis.* Brain, 2004. **127**(Pt 11): p. 2498-505.

64. Kann, O. and R. Kovacs, *Mitochondria and neuronal activity.* Am J Physiol Cell Physiol, 2007. **292**(2): p. C641-57.

65. Ohno, N., et al., *Myelination and axonal electrical activity modulate the distribution and motility of mitochondria at CNS nodes of Ranvier.* J Neurosci, 2011. **31**(20): p. 7249-58.

66. Smith, K.J. and H. Lassmann, *The role of nitric oxide in multiple sclerosis.* Lancet Neurol, 2002. **1**(4): p. 232-41.

67. Redford, E.J., R. Kapoor, and K.J. Smith, *Nitric oxide donors reversibly block axonal conduction: demyelinated axons are especially susceptible.* Brain, 1997. **120 (Pt 12)**: p. 2149-57.

68. Smith, K.J., et al., *Electrically active axons degenerate when exposed to nitric oxide.* Ann Neurol, 2001. **49**(4): p. 470-6.

69. Frohman, T.C., et al., *Uhthoff's phenomena in MS-clinical features and pathophysiology.* Nat Rev Neurol, 2013.

70. Waxman, S.G., *Axonal conduction and injury in multiple sclerosis: the role of sodium channels.* Nat Rev Neurosci, 2006. **7**(12): p. 932-41.

71. Stys, P.K., *General mechanisms of axonal damage and its prevention.* J Neurol Sci, 2005. **233**(1-2): p. 3-13.

72. Moll, C., et al., *Increase of sodium channels in demyelinated lesions of multiple sclerosis.* Brain Res, 1991. **556**(2): p. 311-6.

73. Andrews, H.E., et al., *Mitochondrial dysfunction plays a key role in progressive axonal loss in Multiple Sclerosis.* Med Hypotheses, 2005. **64**(4): p. 669-77.

74. Mao, P. and P.H. Reddy, *Is multiple sclerosis a mitochondrial disease?* Biochim Biophys Acta, 2010. **1802**(1): p. 66-79.

75. Su, K.G., et al., *Axonal degeneration in multiple sclerosis: the mitochondrial hypothesis.* Curr Neurol Neurosci Rep, 2009. **9**(5): p. 411-7.

76. Mark, L.P., et al., *Pictorial review of glutamate excitotoxicity: fundamental concepts for neuroimaging.* AJNR Am J Neuroradiol, 2001. **22**(10): p. 1813-24.

77. Pitt, D., P. Werner, and C.S. Raine, *Glutamate excitotoxicity in a model of multiple sclerosis.* Nat Med, 2000. **6**(1): p. 67-70.

78. Shindler, K.S., et al., *Inflammatory demyelination induces axonal injury and retinal ganglion cell apoptosis in experimental optic neuritis.* Exp Eye Res, 2008. **87**(3): p. 208-13.

79. Quinn, T.A., M. Dutt, and K.S. Shindler, *Optic neuritis and retinal ganglion cell loss in a chronic murine model of multiple sclerosis.* Front Neurol, 2011. **2**: p. 50.

80. Meyer, R., et al., *Acute neuronal apoptosis in a rat model of multiple sclerosis.* J Neurosci, 2001. **21**(16): p. 6214-20.

81. Matsunaga, Y., et al., *Visual functional and histopathological correlation in experimental autoimmune optic neuritis.* Invest Ophthalmol Vis Sci, 2012. **53**(11): p. 6964-71.

82. Diem, R., et al., *Combined therapy with methylprednisolone and erythropoietin in a model of multiple sclerosis.* Brain, 2005. **128**(Pt 2): p. 375-85.

Chapter 6

Conclusion

Optic neuritis is frequently the first sign of multiple sclerosis (MS). The pathologies result from lymphocytes crossing blood-brain barrier (BBB) and then attacking myelin in central nervous system (CNS) and, finally, lead to inflammation, demyelination, and axonal injury [1]. Better understanding of the mechanism and relationship of optic neuritis and MS will lead to more efficient treatment strategies. Recently, MRI has been widely used as a non-invasive approach to detect and diagnose the morphological changes of MS over several decades to track or diagnose the disease process [2-5]. Functional deficits might be an early pathological event that precedes the morphological changes. However, currently the most commonly used functional test is BOLD (blood oxygen level dependent) fMRI, which mostly focuses on cortical regions, but is limited in the analysis of white-matter function [6]. Magnetic resonance imaging (MRI) can reflect different physical properties in tissues, such as T1, T2, and water diffusivity. We further took advantage of these properties to dynamically investigate *in vivo* functional activity in EAE mice, the mouse model of MS, which also develops optic neuritis.

6.1 Axonal transport using manganese-enhanced MRI (MEMRI)

Axonal transport, the transport of proteins and organelles within the axons, is crucial to maintaining normal neuronal function. There are multiple reports in the literature that axonal transport dysfunction or disruption is an early event of neurodegenerative disease, such as Alzheimer's disease [7]. However, few studies focus on the integrity of axonal transport in MS patients or experimental autoimmune encephalomyelitis (EAE) animal models. Therefore,

investigating axonal transport in the EAE mice might provide pathological information about MS before morphological changes. Manganese-enhanced MRI (MEMRI) is a promising tool to tract dynamic Mn^{2+} transport within visual system which will allow us to investigate axonal transport *in vivo*. Since Mn^{2+} is paramagnetic, MEMRI provides obvious contrast on T1-weighted (T1W) image and as a Ca^{2+} analogue it can enter neurons via voltage-gated Ca^{2+} channels and be transported down the axon[8, 9]. However, the cellular toxicity of Mn^{2+} has long been recognized as overexposure causes Parkinsonism [10]. Hence, it is important to determine the Mn^{2+} dosage which maximizes MR detectability and minimizes toxicity. Therefore, before we apply MEMRI to EAE mice, the optimized dosage for mouse visual system is needed.

In Chapter 2, we compared topical loading with intravitreal injection of $MnCl_2$ for MEMRI of mouse optic nerve to determine the optimal concentration and volume of $MnCl_2$ dose. Visual functional was assessed longitudinally. *In vivo* MEMRI and diffusion tensor imaging (DTI) of optic nerves as well as the T2-weighted (T2W) MRI of mouse retina were used to assess the integrity of visual system tissue after $MnCl_2$ loading. After MRI studies, postmortem histology was performed to validate *in vivo* MRI findings. The results revealed that the previously suggested safe dose for intravitreal injection of $MnCl_2$ caused transient retinal swelling and visual acuity impairment with full recovery within one day in mice. In contrast, the literature reported dose for topical $MnCl_2$ loading caused adverse degeneration of photoreceptors and significantly impaired visual acuity in mice. We not only examined the toxicity of $MnCl_2$ loading, but also demonstrated the utility of *in vivo* MRI contrast as a surrogate marker of visual system tissue integrity.

In Chapter 3, we compared the axonal transport rate in EAE and sham mouse optic nerves using MEMRI with an intravitreal injection of 0.25 μL of 0.2 M $MnCl_2$: the optimal

dosage that was determined in Chapter 2. In order to understand the mechanism of functional deficits at the acute stage, we defined and determined the onset of optic neuritis by mouse visual acuity using the Virtual Optometry System (Optomotry, Cerebral Mechanics, Inc., Canada). MEMRI was performed in EAE eyes as soon as visual acuity dropped (~ 11.3 ± 1.9 days post-immunization). The mice in the sham group did not develop visual impairment but underwent the same MEMRI procedure at the similar time range. During the MEMRI procedure, mice were directly put in the scanner after intravitreal injection. A series of 3D-T1W images was acquired every 0.55 hour from 0.55 – 5.5 hours post-injection. The quantitative data showed that comparing to sham optic nerve, the accumulation rate in EAE mice with moderate and severe optic neuritis was significantly decreased by 19% and 38%, respectively. Similarly, the transport rate in EAE mice with moderate and severe optic neuritis was significantly decreased when compared to sham optic nerve by 43% and 65%, respectively. Postmortem histology confirmed the EAE mice with optic neuritis in this sample developed inflammation, demyelination, and axonal injury pathologies. The degree of axonal transport deficits correlated well with impaired visual function as well as histological pathologies. In conclusion, MEMRI holds potential to track *in vivo* dynamical axonal transport.

6.2 Axonal Activity using diffusion fMRI

Another functional component of neuronal function in the visual system is the electric transmission of the visual signal via depolarization of different ion channels in optic nerve through brain [11]. Myelin plays a role to speed up and conserve signal delivery, so-called saltatory conduction. Since MS is a demyelinative disease, the signal propagation should be blocked or delayed. Currently, fMRI mainly depends on BOLD signal change to identify neuron activity in gray matter indirectly through vascular changes. Several reports have explored

functional deficits in gray matter of MS, such as motor and visual cortex [12-15]. However, electrical signal propagation also largely relies on white matter, but there have been limited studies focusing on it in MS. Since visual conduction leads to repeated cycles of membrane depolarization, action potential, and repolarization, these successive effects are highly associated with transient ionic gradient changes, osmotic shift of water across cell membranes, and size- and shape-related glial cell swelling [16-25]. Finally, those effects might results in the extracellular space (ECS) shrinkage. Displacement of water molecules in tissue can be detected by diffusion MRI. Le Bihan et al. reported that during visual stimulation, increased signal intensity (2%) was observed in diffusion weighted images [26]. That is, apparent diffusion coefficient (ADC) was decreased and could be a direct means to reveal neuronal activity. However, Miller et al. later reported that the vascular effects also led to ADC decrease without visual stimulation [27]. Unlike gray matter, diffusion MRI might be a potential means to reveal neuronal activity in white matter due to limited blood flow and blood volume. Hence, ADC might be sensitive to stimulation-associated ECS shrinkage, which limits the displacement of water molecules.

In Chapter 4, we gave mice visual stimulation and measured $ADC_{\perp}$ and $ADC_{\parallel}$ using standard diffusion measurement. A 27% stimulus-associated $ADC_{\perp}$ decrease, which is the ADC perpendicular to optic nerve/axonal fibers, was observed. No change $ADC_{\parallel}$, which is the ADC parallel to optic nerve/axonal fibers, was shown. The stimulus-associated $ADC_{\perp}$ decrease was repeatable. To confirm that the $ADC_{\perp}$ decrease was independent of vascular contribution, we performed the same experimental procedure in hypercapnia mice. The results showed that during visual stimulation, a significant 20% $ADC_{\perp}$ decrease was observed suggesting there were no

vascular effects. Therefore, diffusion measurement in white matter could directly reveal axonal activity.

In Chapter 5, we further applied the diffusion measurement with visual stimulation in EAE mice with optic neuritis to assess functional integrity in optic nerves. After immunization, daily visual acuity was confirmed by Virtual Optometry System (Optomotry, Cerebral Mechanics, Inc., Canada). Diffusion fMRI was performed in EAE eyes as soon as visual acuity dropped (~ 10.6 ± 1.7 days post-immunization). The mice in the sham group did not develop visual impairment but underwent the same diffusion fMRI procedure at the similar time range. The results showed that visual stimulation produced a significant 25% stimulus-associated $ADC_{\perp}$ decrease in sham mice, which is comparable of our previous report in normal mice (~27%). Only a statistically insignificant 7% stimulus-associated $ADC_{\perp}$ decreased was seen in acute-stage EAE mice. The reduced $ADC_{\perp}$ response was consistent with impaired visual function (lower visual acuity) and histological pathologies including axonal inflammation, demyelination, and axonal injury. The results also implied that diffusion fMRI holds promise for directly gauging *in vivo* white-matter dysfunction.

6.3 Conclusion

To conclude, axonal transport disruption and axon-activity dysfunction, at optic neuritis onset in EAE mice were confirmed by MEMRI and diffusion fMRI, respectively. These functional deficits were highly correlated with impaired visual function and morphological changes. Therefore, non-invasive MRI not only provides a way to reflect morphological changes but also holds potential to assess functional integrity in white matter.

6.4 Reference

1. Compston, A. and A. Coles, *Multiple sclerosis.* Lancet, 2008. **372**(9648): p. 1502-17.

2. Ge, Y., *Multiple sclerosis: the role of MR imaging.* AJNR Am J Neuroradiol, 2006. **27**(6): p. 1165-76.

3. Filippi, M., *MRI-clinical correlations in the primary progressive course of MS: new insights into the disease pathophysiology from the application of magnetization transfer, diffusion tensor, and functional MRI.* J Neurol Sci, 2003. **206**(2): p. 157-64.

4. Emerson, M.R., et al., *Enhancing the ability of experimental autoimmune encephalomyelitis to serve as a more rigorous model of multiple sclerosis through refinement of the experimental design.* Comp Med, 2009. **59**(2): p. 112-28.

5. Inglese, M. and M. Bester, *Diffusion imaging in multiple sclerosis: research and clinical implications.* NMR Biomed, 2010. **23**(7): p. 865-72.

6. Rostrup, E., et al., *Regional differences in the CBF and BOLD responses to hypercapnia: a combined PET and fMRI study.* Neuroimage, 2000. **11**(2): p. 87-97.

7. De Vos, K.J., et al., *Role of axonal transport in neurodegenerative diseases.* Annu Rev Neurosci, 2008. **31**: p. 151-73.

8. Silva, A.C., et al., *Manganese-enhanced magnetic resonance imaging (MEMRI): methodological and practical considerations.* NMR Biomed, 2004. **17**(8): p. 532-43.

9. Koretsky, A.P. and A.C. Silva, *Manganese-enhanced magnetic resonance imaging (MEMRI).* NMR Biomed, 2004. **17**(8): p. 527-31.

10. Olanow, C.W., *Manganese-induced parkinsonism and Parkinson's disease.* Ann N Y Acad Sci, 2004. **1012**: p. 209-23.

11. Nicholls, J.G., *From neuron to brain*. 4th ed2001, Sunderland, Mass.: Sinauer Associates.

12. Rocca, M.A., M. Absinta, and M. Filippi, *The role of advanced magnetic resonance imaging techniques in primary progressive MS.* J Neurol, 2012. **259**(4): p. 611-21.

13. Rocca, M.A., et al., *Large-scale neuronal network dysfunction in relapsing-remitting multiple sclerosis.* Neurology, 2012. **79**(14): p. 1449-57.

14. Gallo, A., et al., *Visual resting-state network in relapsing-remitting MS with and without previous optic neuritis.* Neurology, 2012. **79**(14): p. 1458-65.

15. Staffen, W., et al., *Cognitive function and fMRI in patients with multiple sclerosis: evidence for compensatory cortical activation during an attention task.* Brain, 2002. **125**(Pt 6): p. 1275-82.

16. Holthoff, K. and O.W. Witte, *Intrinsic optical signals in rat neocortical slices measured with near-infrared dark-field microscopy reveal changes in extracellular space.* J Neurosci, 1996. **16**(8): p. 2740-9.

17. Ransom, B.R. and R.K. Orkand, *Glial-neuronal interactions in non-synaptic areas of the brain: studies in the optic nerve.* Trends Neurosci, 1996. **19**(8): p. 352-8.

18. Bay, V. and A.M. Butt, *Relationship between glial potassium regulation and axon excitability: a role for glial Kir4.1 channels.* Glia, 2012. **60**(4): p. 651-60.

19. Kole, M.H., et al., *Action potential generation requires a high sodium channel density in the axon initial segment.* Nat Neurosci, 2008. **11**(2): p. 178-86.

20. Waxman, S.G., *Conduction in myelinated, unmyelinated, and demyelinated fibers.* Arch Neurol, 1977. **34**(10): p. 585-9.

21. Schwartzkroin, P.A., S.C. Baraban, and D.W. Hochman, *Osmolarity, ionic flux, and changes in brain excitability.* Epilepsy Res, 1998. **32**(1-2): p. 275-85.

22. Ransom, B.R., C.L. Yamate, and B.W. Connors, *Activity-dependent shrinkage of extracellular space in rat optic nerve: a developmental study.* J Neurosci, 1985. **5**(2): p. 532-5.

23. Flint, J., et al., *Diffusion weighted magnetic resonance imaging of neuronal activity in the hippocampal slice model.* Neuroimage, 2009. **46**(2): p. 411-8.

24. Le Bihan, D. and H. Johansen-Berg, *Diffusion MRI at 25: exploring brain tissue structure and function.* Neuroimage, 2012. **61**(2): p. 324-41.

25. Le Bihan, D., *The 'wet mind': water and functional neuroimaging.* Phys Med Biol, 2007. **52**(7): p. R57-90.

26. Le Bihan, D., et al., *Direct and fast detection of neuronal activation in the human brain with diffusion MRI.* Proc Natl Acad Sci U S A, 2006. **103**(21): p. 8263-8.

27. Miller, K.L., et al., *Evidence for a vascular contribution to diffusion FMRI at high b value.* Proc Natl Acad Sci U S A, 2007. **104**(52): p. 20967-72.

Appendix

Reprints from the annual Proceedings of

the International Society of Magnetic Resonance in Medicine

Toxicity of Mn^{2+} in MEMRI with topical loading

Tsen-Hsuan Lin[1], and Sheng-Kwei Song[2]
[1]Physics, WUSTL, St Louis, MO, United States, [2]Radiology, Washington University in St Louis, St Louis, MO, United States

Introduction

Manganese enhanced MRI (MEMRI) has been widely applied to investigate axonal transport in the rodent visual pathway. Intraocular injection is an established approach for $MnCl_2$ loading. Bearer et al. [1] have reported the impaired visual evoke potential (VEP) at the lowest intraocular dose allowing detectable MEMRI effect. In a recent report, the noninvasive topical $MnCl_2$ loading [2] was demonstrated without the need of invasive intraocular injection of $MnCl_2$. However, the effect of topical $MnCl_2$ loading on visual function was not evaluated. In this study, the toxicity of $MnCl_2$ was evaluated by visual acuity (VA) measurement [3,4] as well as optic nerve and retina MRI.

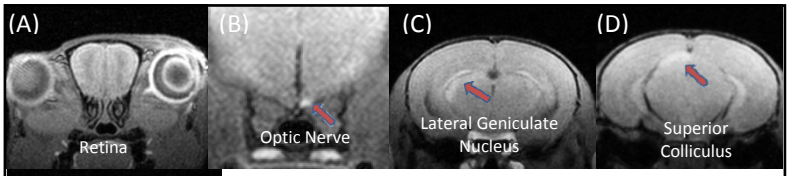

Fig. 1 Four representative axial images from 3D T1W data set one day after 0.75 M $MnCl_2$ loading. Visual pathway was enhanced from (A) right retina, (B) right optic nerve, (C) left lateral geniculate nucleus, and (D) left superor colliculus ; (E) oblique T1W image that included retina and optic nerve showed Mn^{2+} enhanced signal at right side.

Material and Method

Four groups of female C57BL/6 mice at 8 weeks of age were examined: control (n=4), 0.5 (n=4), 0.75 (n=6), and 1 M (n=5) of $MnCl_2$ loading. Mice were anesthetized using 1.5% isoflurane/oxygen for topical loading of 20µl of $MnCl_2$ on the right eye. An additional 20µl of $MnCl_2$ was applied every 20 min to compensate the volume loss due to evaporization. The body temperature was maintained at 37 ºC during loading with an electric heating pad. After an hour, a lint free tissue was used to remove the solution. Twenty-four hours after loading, mice were anesthetized and imaged on a 4.7 T animal scanner using a 3D gradient echo sequence with the following parameters: TR 15ms TE 2.63ms, flip angle 20, number of averages 16, FOV 15 × 15 mm^2, and matrix size 128 × 128 × 64 (zero-filled to 256 × 256 × 64). Region of interest (ROI) included retina, optic nerve (ON), and superior colliculus (SC). Visual acuity (VA) was assessed daily from 1 to 7 days. Optic nerve were imaged on 4.7 T animal scanners with multiple-echo spin-ehco diffusion weighted sequence at days 1 and 7 with the following parameters: TR 1.5s, TE 34 ms, inter-ehco delay 19 ms, FOV 22.5 × 22.5 mm^2 , matrix size 192 × 192 (zero-filled to 384×384), thickness 0.5 mm. Retina images were performed on an11.74 T scanner with a standard spin echo sequence with the following parameters: TR 2s, TE 34ms FOV 12 × 12 mm^2 matrix size 256 × 256 (zero-filled to 512 × 512).

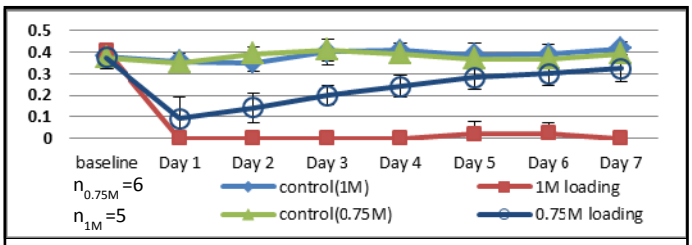

Fig. 2 Visual acuity (VA) time course after 0.75 and 1 M $MnCl_2$ loading on right eyes. VA irreversibly decreased from normal (0.4) to complete blind (0) after 1 M loading. VA decreased to 0.1 (not completely bind) and recovered at day 5 after 0.75 M loading.

Results & Discussion

At one day after 0.75 and 1 M $MnCl_2$ loading on right eyes, significant T1W enhancement was seen in the right retina, right optic nerve, left lateral geniculate nucleus and left superior colliculus (Fig. 1). Only slight enhancement of retina was seen in mice loaded with 0.5M $MnCl_2$. Significant visual function impairment was seen in both 0.75 and 1 M $MnCl_2$ loaded eyes (Fig. 2). Upon 1 M $MnCl_2$ loading, irreversible VA decreased from normal (VA = 0.4) to complete blindness (VA = 0) from 1 day after loading. In 0.75 M $MnCl_2$ loaded eyes, VA decreased to 0.1 (not completely blind) at 1 day after and recovered to approximately the normal range at 5 days after loading (Fig. 2). There was no detected axonal or myelin injury in optic nerve loaded with 1M $MnCl_2$ at 1 and 7 days after loading (Fig. 3). However, a significant reduction in retinal thickness (~27% compared to the control) was seen in eyes loaded with 1M $MnCl_2$ (Fig. 3).

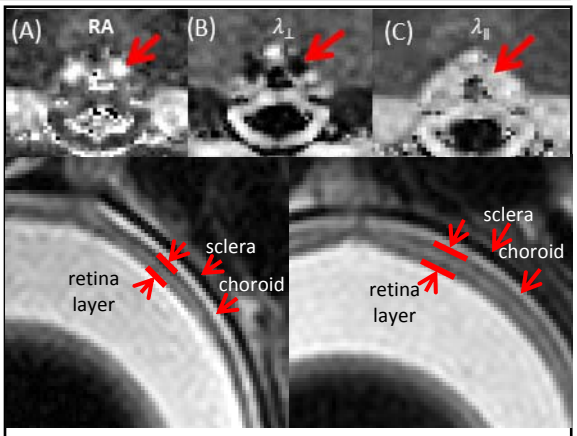

Fig. 3 DTI parameters of optic nerve, indicated by the arrow, in (A) RA, (B) radial, and (C) axial diffusivity maps after 1 M $MnCl_2$ loading at the right eye were not affected. T2W images showed that the right retina (D) after 1 M $MnCl_2$ loading was thinner than the control retina (E). Thickness decreased by 27 % after $MnCl_2$ loading.

Conclusion

Our data suggested that although topical loading of 1 M $MnCl_2$ did not injure optic nerve, as indicated by normal DTI parameters, the damaged retina was likely responsible for the irreversible loss of vision. The reduced retinal thickness may reflect the loss of retinal cells. The success in optic nerve enhancement after loading may suggest the retinal ganglion cells were not lost and still capable of uptake Mn^{2+}. Alternately, the retinal ganglion cell was damaged after uptake of Mn^{2+} and transporting to its axon. This is the first time retinal integrity was assessed after $MnCl_2$ loading.

Reference

[1] Bearer *et al*., Neuroimage, 2007, 37(suppl 1) S37-S46; [2] Sun *et al*., IOVS, 2011, 52: 3914-3920. [3] Prusky *et al.*, IOVS, 2004, Vol: 45 No.12; [4] Douglas *et al.*, Visual Neuroscience, 2005, 22, 677-684

Diffusion fMRI detects white-matter dysfunction in mice with acute optic neuritis

Tsen-Hsuan Lin[1], William M. Spees[2,3], Robert Mikesell[4], Anne H. Cross[3,4], and Sheng-Kwei Song[2,3]

[1]Physics, Washington University, St. Louis, MO, United States, [2]Radiology, Washington University School of Medicine, St. Louis, MO, United States, [3]The Hope Center for Neurological Disorders, Washington University School of Medicine, St. Louis, MO, United States, [4]Neurology, Washington University School of Medicine, St. Louis, MO, United States

Introduction

Conventional fMRI, based on blood-oxygen level dependent (BOLD) signal change, to identify neuronal activation is largely limited to assess gray matter activation. We have developed a diffusion fMRI method to detect white matter functional activation in normal, healthy mouse optic nerves and observed a 27% decrease in the water apparent diffusion coefficient perpendicular to the axonal fibers ($ADC_\perp$) upon flashing light stimulation. Meanwhile, we excluded the vascular contributions to the $ADC_\perp$ change via measurements in hypercapnic mice [1]. In the current study, we extend this method to non-invasively assess the response of experimental autoimmune encephalomyelitis (EAE) mouse optic nerves to visual stimulation with ongoing optic neuritis. Our findings suggest that acute axonal pathologies present at the onset of optic neuritis led to decreased axonal activation in EAE mice. Thus, diffusion fMRI holds the potential to provide a non-invasive assessment of functional integrity of CNS axons.

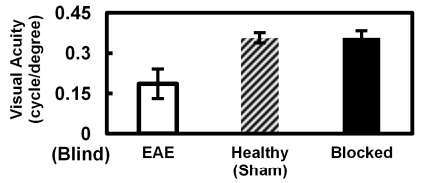

Figure 1 Averaged visual acuity of EAE (n=7), sham (n=7), and contralateral blocked (n=14) eyes (measured before MR experiments) showed the poor vision of EAE eyes and normal vision of sham and blocked eyes. Note: EAE mice in this sample of animals developed unilateral visual impairment.

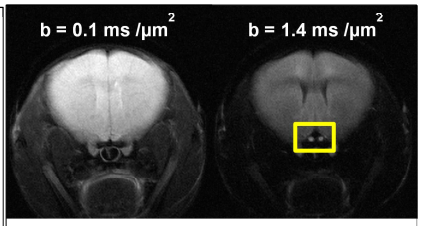

Figure 2 Two diffusion-weighted images (DWIs) with 0.1 and 1.4 ms/μm² b-values were calculated to generate apparent diffusion coefficient ($ADC_\perp$) map. Yellow box indicates the location of optic nerves

Materials and Methods

Animal Model: EAE was induced in seven female ten-week-old C57BL/6 mice with MOG_{35-55} peptide in complete Freund's adjuvant emulsion. The other seven age-matched control mice (sham group) underwent the same procedure without MOG_{35-55} immunization. For EAE mice, daily visual acuity (VA) was measured and MR was performed when VA ≤ 0.25 cycle/degree (Fig. 1). Typically, this occurs by 9-13 days post-immunization. Daily VA measurements assured normal visual function in control mice [2]. *Diffusion-weighted image (DWI) protocol:* Experiments were performed on a 4.7-T Agilent small-animal MR scanner with a multiple-echo spin-echo imaging sequence [3] with the following parameters: TR = 1.5 s, TE = 37.1 ms, inter-echo delay = 23.6 ms, FOV = 20 × 20 mm², matrix size = 256 × 256 (zero-filled to 512 × 512), and thickness = 1.3 mm. The image slice was planned carefully to be orthogonal to the optic nerves, thus minimizing partial volume effects. A pair of one-direction (perpendicular to optic nerve) DWI was acquired with b-value = 0.1 and 1.4 ms/μm², δ = 5 ms, and Δ = 18 ms. Acquisition time was 12.8 minute for each pair of DWI images [1]. *Visual stimulation:* A white LED light was placed 5 cm in front of mouse nose for stimulation of the experimental eye. The other eye was covered with parafilm and blocked using black electrical tape. *Diffusion fMRI strategy:* We acquired one baseline DWI dataset without stimulation. Then, the stimulus-on DWI dataset was acquired during application of flashing light stimulation. Finally, the LED was turned off for last DWI acquisition [1]. *Data analysis:* $ADC_\perp$ maps were generated from two DWIs (Fig. 2). ROI was selected using the same determination as our previous study [1]. *Histology:* mice were perfusion fixed immediately after the *in vivo* MRI for immunohistochemical staining.

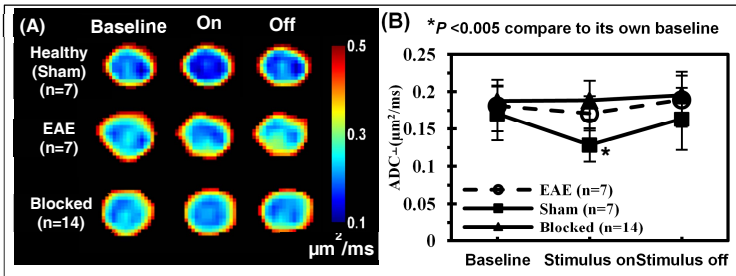

Figure 3 Averaged $ADC_\perp$ maps of sham, EAE, and contralateral blocked eyes at baseline, with and without stimulation (A). Comparing to its own baseline map, sham group showed obvious $ADC_\perp$ decrease. Statistical $ADC_\perp$ average plot (B) was in agreement with the pattern of averaged $ADC_\perp$ maps (A). A significant 25% $ADC_\perp$ decrease was observed in sham group. EAE group only showed a slightly 5% decrease. Regarding blocked eyes, there was no difference between the scans of baseline and stimulation.

Results

Color-coded group-averaged $ADC_\perp$ maps for the different experimental groups are shown in Figure 3A. Group-averaged $ADC_\perp$ at baseline, with and without visual stimulus for EAE, healthy, and blocked optic nerves are depicted in Figure 3B. In healthy optic nerves, application of visual stimulus led to a significant $ADC_\perp$ decrease (~25%) while in EAE optic nerves only a slight $ADC_\perp$ decrease (~5%) was observed. ADC changes were reversible with cessation of stimulus. Blocked eyes showed no difference between baseline and stimulation scans. From Figure 3A it can also be appreciated that optic nerves in EAE mice are slightly swollen. Representative SMI31 (intact axons), MBP (myelin sheaths), and SMI32 (injured axons) staining images of optic nerves were showed that EAE optic nerve developed axonal beading, distorted myelin sheaths, and injured axons (Fig. 4).

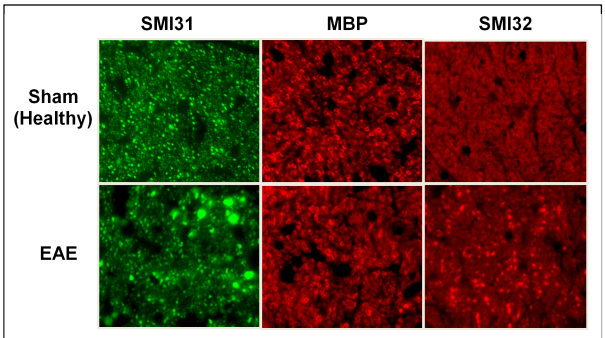

Figure 4 Representative 60× SMI31 (intact axon), MBP (myelin sheath), and SMI32 (injured axon) staining images from control and EAE mouse. EAE mouse optic nerve showed obviously axon beading (SMI31), distorted myelin sheath (MBP), and positive SMI32 staining.

Conclusion

Our results demonstrate that diffusion fMRI can non-invasively differentiate between patterns of *in vivo* axonal activation in healthy and diseased optic nerve. Histology of retinal samples is ongoing, however, since measurements are made early in the EAE time course, it is likely that the pathology is localized to the optic nerve-- prior to any retinal ganglion cell loss [4]. More broadly, with other stimulus paradigms, this technique may enable global detection of white-matter dysfunction throughout the CNS.

Reference

[1] Spees et al., Neuroimage (in press); [2] Chiang et al., Proc. Intl. Soc. Magn. Reson. Med. 20 (2012), 3058; [3] Tu et al., Proc. Intl. Soc. Magn. Reson. Med. 18 (2010), 4001; [4] Shindler et al., Exp. Eye Res. 87: 208-213.

Axonal transport rate decreased at the onset of optic neuritis in EAE mice

Tsen-Hsuan Lin[1], Joong Hee Kim[2], Carlos Perez-Torres[2], Chia-Wen Chiang[2], Kathryn Trinkaus[3], Anne H. Cross[4,5], and Sheng-Kwei Song[2,5]

[1]Physics, Washington University, St. Louis, MO, United States, [2]Radiology, Washington University School of Medicine, St. Louis, MO, United States, [3]Biostatistics, Washington University School of Medicine, St. Louis, MO, United States, [4]Neurology, Washington University School of Medicine, St. Louis, MO, United States, [5]The Hope Center for Neurological Disorders, Washington University School of Medicine, St. Louis, MO, United States

Introduction

Multiple sclerosis (MS) is an inflammatory demyelinating disorder of central nervous system (CNS). Frequently, optic neuritis (ON) is an early symptom of MS[1]. Axonal transport deficits are an early event of many neurodegenerative diseases[2]. However, few reports have assessed axonal transport rate in MS or in experimental autoimmune encephalomyelitis (EAE). EAE induced in C57BL/6 mice is a widely used animal model of MS and exhibits many MS-like pathologies, including ON. Mn^{2+}, a Ca^{2+} analog, is paramagnetic to shorten T1 relaxation time and crosses cell membrane trough voltage-dependent Ca^{2+} channels. Hence, *in vivo* manganese-enhanced MRI (MEMRI) provides a way to investigate real-time axonal transport in rodent visual pathway. In this study, we measured visual acuity (VA) by optokinetic response (OKR) to define onset of ON in EAE mice[3]. Then, $MnCl_2$ was injected in the vitreous of sham and EAE mouse eyes, followed by series of time-lapse T1-weighted (T1W) images to compare axonal transport rate. The results suggested that axonal transport impairment was present and correlated with impaired visual functional and pathologies. The results of this study showed that axonal transport deficit is an early event of functional deficit of optic nerve in EAE mice. *In vivo* MEMRI is ideal to investigate axonal transport.

Materials and Methods

Animal Model: EAE was induced in 10 female eight-week-old C57BL/6 mice with MOG_{35-55} peptide in incomplete Freund's adjuvant emulsion. The other six age-matched control mice (sham group) underwent the same procedure without MOG_{35-55} immunization. Daily visual acuity (VA) was measured and MEMRI was performed at VA ≤ 0.25 cycle/degree (c/d). According to severity of ON, mice were separated into three groups, sham (VA = 0.35/0.4 c/d), moderate (VA = 0.2/0.25 c/d), and severe (VA = 0 c/d) ON. ***Intravitreal injection:*** A dose of 50 nmol $MnCl_2$ (0.25μL of 0.2 M) was delivered to vitreous space at a rate of 3μL/min with 34-gaugue needle[4]. ***MEMRI:*** A pair of 8-cm diameter volume and 1.7-cm diameter surface active-decoupled coils was used. Experiments were performed on a 4.7-T Agilent small-animal MR scanner with a standard 3D gradient echo sequence with the following parameters: TR = 15 ms, TE = 2.63 ms, flip angle = 20°, FOV = 15 × 15 × 22 mm^3, matrix size = 128 × 128 × 64 (zero-filled to 256 × 256 × 128), acquisition time = 32.8 minutes, number of signal average = 16, and ten successive sets of 3D-T1W images were captured at ~0.55 – 5.5 hours post-injection. ***B1-inhomogeneity correction:*** 3D-T1W image of a 2% agar gel phantom was placed underneath surface coil using the same acquisition MEMRI parameters with 64 averages. The raw 3D-T1W image of mouse brain was divided by the 3D-T1W image of phantom voxel by voxel using ImageJ to correct B1-inhomogeneity. ***Data analysis:*** The corrected 3D-T1W image set was adjusted and rotated to oblique plane that covered retina and optic nerves before chiasm (Fig. 1). **Accumulation rate calculation:** ROIs (region of interest) were drawn on Mn^{2+}-loading optic nerves and reference area for all oblique corrected T1W images (Fig. 2A). The slope of normalized intensity, calculated by ratio of Mn^{2+}-loading ROI and reference area, was accumulation rate (Fig. 2C and 2E). **Transport rate calculation:** ROI lines were drawn on Mn^{2+}-loading and contralateral optic nerves for all oblique corrected T1W images (Fig. 2B). Arrival of Mn^{2+} was determined by intensity of voxel ≥ threshold (mean + 2SD of contralateral ROI line). The slope of normalized displacement (number of voxels with Mn^{2+} arrival), normalized by the whole optic-nerve ROI line, was transport rate. After converting with image resolution, transport rate was converted to millimeter per hour (Fig. 2 D and F). ***Histology:*** mice were perfusion fixed immediately after the *in vivo* MEMRI for immunohistochemical staining of the optic nerve.

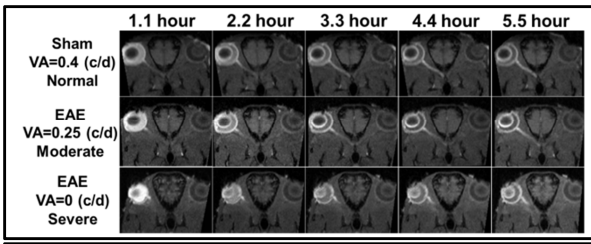

Figure 1 A serial time-lapse oblique corrected T1W images from representative mice from sham, moderate-ON, and severe-ON optic nerves were presented to demonstrate the different degree of Mn^{2+}-enhancement from 1.1 – 5.5 hours post-injection.

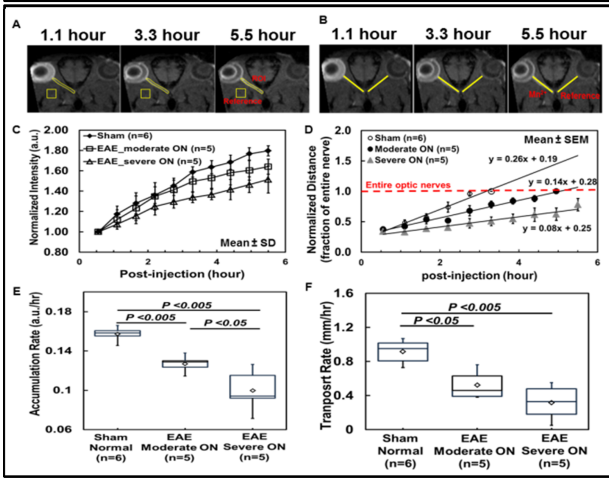

Figure 2 For accumulation rate, ROIs were drawn on Mn^{2+}-loading optic nerve and reference muscle for each time point (A). The slope of each normal intensity tend was accumulation rate (C). With VA decreased, lower accumulation rate was shown (E). For transport rate, ROI lines were drawn on Mn^{2+}-loading and contralateral optic nerves (B). The slope of each normalized displacement trend was transport rate in percentage optic nerve/hour (D). After converting with image resolution, transport rate was acquired in millimeter/hour (F). When VA decreased, lower transport rate was observed

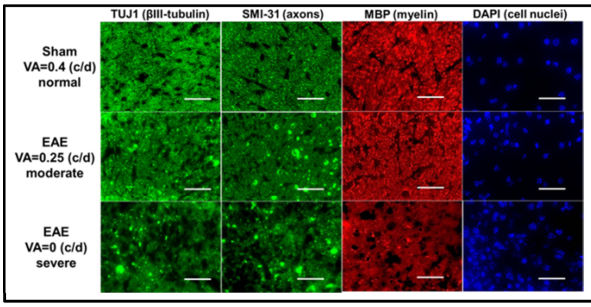

Figure 3 Representative 60x TUJ1 (βIII-tubulin), SMI31 (intact axon), MBP (myelin sheath), and DAPI (cell nuclei) staining from sham, moderate-ON, and severe-ON optic nerves. EAE optic nerves showed the sign of axonal transport deficits (less microtubule-associated βII-tubulin), axonal injury (less axon), demyelination (less myelin area), and inflammation (more cells). Scale bar: 25μm

Results

Compared to sham optic nerves, Mn^{2+} accumulation rate was significantly decreased by 19% ($p < 0.005$, moderate EAe) and 38% ($p < 0.005$, severe EAE) (Fig. 2E). The accumulation rate was 23% ($p < 0.05$) slower in the EAE mice with severe ON than that with the moderate ON (Fig. 2E). Compared to sham optic nerves, Mn^{2+} transport rate was significant decreased by 43% ($p < 0.05$, moderate EAE) and 65% ($p < 0.005$, severe EAE). Representative TUJ1(microtubule-associated βIII-tubulin, staining the base structure for kinesin motor protein movement)[5], SMI31 (intact axon), MBP (myelin sheath), and DAPI (cell nuclei) stains showed that EAE optic nerves developed axonal transport deficits, axonal injury, demyelination, and inflammation.

Conclusion

Our results demonstrate that MEMRI can provide an *in vivo* real-time quantification of axonal transport in EAE mice at ON onset. In addition to morphological changes, functional deficits, such as axonal transport disruption, also occurred at this stage. Preventing the worsening or curing the early axonal transport deficit may be a potential treatment target to halt the degeneration of axons in MS. Our results showed the first quantitative assessment of axonal transport in EAE mice suggesting that MRMRI is suitable for pre-clinical drug tests.

Reference

[1] Arnold ; Am J Ophthalmol 2005;139 : 1101-1108; [2] Millecamps and Julien ; Nat Rev Neurosci 2013 ; 14 :161-176 [3] Chiang et al., Proc. Intl. Soc. Magn. Reson. Med. 20 (2012), 3085; [4] Chan et al., Investigativ Ophthalmology & Visual Science 2012; 53 :2777-2785; [5] Niwa et al., The EMBO Journal 2013; 32: 1352-1364.

Acknowledgements

Supported in part by NIH R01-NS047592, P01-NS059560, NMSS RG 4549A4/1, and DOD W81XWH-12-1-0457

Washington University in St. Louis

GRADUATE SCHOOL OF ARTS & SCIENCES

EXAMINATION APPROVAL FORM

Date September 11, 2013

To the Graduate School:

We, the undersigned, report that as a committee we have examined the dissertation entitled

Assessing Functional Deficits at Optic Neuritis Onset in EAE Mice Using Manganese-Enhanced MRI (MEMRI) and Diffusion fMRI

and have given it our approval for acceptance in partial fulfillment of the requirements for the degree of Doctor of Philosophy. We certify that the dissertation conforms to the requirements described in "Statement by Graduate Council on Minimal Requirements for Ph.D. Dissertations" as published in the Washington University Doctoral Dissertation Guide. We also certify that we have examined Ms. Tsen-Hsuan Lin upon the work done in Physics and find that (his, her) attainments are such that (he, she) may properly be admitted to the degree of Doctor of Philosophy.

Signed Mark S Conradi, Chair
Professor Mark S. Conradi

for Jason Woodsby WUSC
Professor Jason Woods

James S. Schilling
Professor James S. Schilling

Ralf Wessel
Professor Ralf Wessel

Professor Sheng-Kwei Song

Dr. William M. Spees

Chair of Department or Program

I dissent from the foregoing report.

_____ _____

This form should be signed and forwarded to the Graduate School of Arts and Sciences, Cupples II Suite 204 or Campus Box 1187.

Recorded by the Graduate School *(initial/date)*: _____

Dissertation Submission Approved *(initial/date)*: _____